

Dissertation
submitted to the
Combined Faculties for the Natural Sciences and for Mathematics
of the Ruperto-Carola University of Heidelberg, Germany
for the degree of
Doctor of Natural Sciences

Put forward by
Yifei Wang
born in Tianjin, P.R. China
Oral Examination: February 4, 2014

**Charmed Meson Reconstruction in the
 $D^{*+} \rightarrow D^0(K^-\pi^+)\pi^+$ Decay Channel
in p-p Collisions at $\sqrt{s} = 7$ TeV with the
ALICE Experiment**

Referees:

**Prof. Dr. Norbert Herrmann
Dr. Kai Schweda**

Rekonstruktion von Mesonen mit Charm im Zerfallskanal $D^{*+} \rightarrow D^0(K^-\pi^+)\pi^+$ in p-p Kollisionen bei $\sqrt{s} = 7$ TeV mit ALICE

Im Rahmen dieser Arbeit wurde die prompte Produktion des $D^{*+}(2010)$ Mesons und seines Antiteilchens bei Midrapidität im Zerfallskanal $D^{*+} \rightarrow D^0(K^-\pi^+)\pi^+$ in p-p collisions bei $\sqrt{s} = 7$ TeV im ALICE Experiment gemessen. Der differentielle Wirkungsquerschnitt wird in zehn Intervallen des Transversalimpulses im Bereich $1 < p_T < 24$ GeV/c vorgestellt. Der gemessene differentielle Wirkungsquerschnitt von prompter $D^{*+}(2010)$ Meson-Produktion wird durch modernste Rechnungen in perturbativer QCD im Rahmen von FONLL und GM-FVNS innerhalb der relativ großen Unsicherheiten im Experiment und in den Rechnungen beschrieben. Hadronisierung von Charm nach D Mesonen mit einem leichten Quark (d) erlaubt eine Beschreibung innerhalb des statistischen Modells. Der gesamte Charm Produktionsquerschnitt wurde unter zusätzlicher Verwendung der ALICE Messungen zur prompten Produktion von D^0 and D^+ Mesonen bestimmt. Es wird angemessene Übereinstimmung mit Ergebnissen anderer LHC Experimente, ATLAS und LHCb, gefunden.

Charmed Meson Reconstruction in the $D^{*+} \rightarrow D^0(K^-\pi^+)\pi^+$ Decay Channel in p-p Collisions at $\sqrt{s} = 7$ TeV with ALICE

Within this thesis, the prompt production of the $D^{*+}(2010)$ meson and its anti-particle has been measured in the $D^{*+} \rightarrow D^0(K^-\pi^+)\pi^+$ decay channel at mid-rapidity from p-p collisions at $\sqrt{s} = 7$ TeV with the ALICE apparatus. The production differential cross section is presented in ten intervals in the transverse momentum range $1 < p_T < 24$ GeV/c. The measured differential cross section of prompt $D^{*+}(2010)$ meson production is described by state-of-the-art perturbative QCD calculations within the framework of FONLL and GM-FVNS within rather large uncertainties in both experiment and calculations. Hadronization of charm into light flavor (d) D mesons allows for a description within the statistical model. The total charm production cross section was extracted by additionally taking into account the ALICE measurements on the prompt production of D^0 and D^+ mesons. Fair agreement with results from other LHC experiments ATLAS and LHCb is found.

Contents

1	Introduction	1
2	Charm Production in Hadron Collisions	5
2.1	Charm Production in p-p Collisions	5
2.2	Perturbative QCD in Heavy Quark Production	12
2.3	pQCD Calculation Models	18
2.3.1	Resummation	19
2.3.2	MNR	20
2.3.3	FONLL	20
2.3.4	GM-VFNS	25
3	The LHC and ALICE	29
3.1	The Large Hadron Collider	29
3.1.1	LHC Setup	29
3.1.2	LHC Experiments	31
3.1.3	LHC in Operation	32
3.2	The ALICE Detector System at the LHC	33
3.2.1	Inner Tracking System	36
3.2.2	Time Projection Chamber	38
3.2.3	Time of Flight Detector	41
3.2.4	VZERO Detector	43
3.3	Data Collection	43
3.3.1	Minimum Bias Trigger	43
3.3.2	LHC Luminosity	44
3.4	Offline Analysis	44
3.4.1	Monte Carlo Simulations	45
3.4.2	Reconstruction	46
4	D^{*+} Reconstruction	49
4.1	D^{*+} Decay Channel	49
4.1.1	$D^0 \rightarrow K^- \pi^+$ Decay Channel	49

4.1.2	$D^{*+} \rightarrow D^0 + \pi_s^+$ Decay Channel	51
4.1.3	The Soft Pion π_s^+	52
4.2	Reconstruction Scheme	54
4.2.1	Invariant Mass	54
4.2.2	Δm Distribution	55
4.2.3	Particle Combination	56
4.2.4	Vertexing Algorithm	57
4.3	Track Selection	58
4.3.1	Selection on Track Quality	58
4.3.2	Selection on Track Kinematics	59
4.3.3	List of Single Track Pre-Selection	60
4.4	Topological Selections	60
4.4.1	Topological Selections of D^0	61
4.4.2	Cuts Optimization	68
4.5	Particle Identification	70
4.5.1	PID Selections on D^0 Daughter Particles	70
4.5.2	PID Selection on the D^{*+}	73
4.6	Yield Extraction	74
4.6.1	Background Fit	74
4.6.2	Bin Counting	74
4.6.3	D^0 Sideband	75
4.6.4	Raw Yields	75
4.7	QA of the D^{*+} Reconstruction	78
4.7.1	Reconstructed D^{*+} Yield	78
4.7.2	Reconstructed D^{*+} Mass	79
4.7.3	Reconstructed D^{*+} Mass Width	81
4.7.4	The D^0 and D^{*+} Invariant Mass Spectra	81
5	Corrections	83
5.1	D^{*+} Efficiency	83
5.2	D^{*+} Corrections	84
5.3	B Feed-down Correction	89
6	Systematic Uncertainties	93
6.1	Systematics from Reconstruction	93
6.2	Systematics from Correction	96
6.3	Systematics Summary	97
7	Charm Cross Section	99
7.1	Differential Charmed Meson Cross Section	99
7.1.1	Differential D^{*+} Cross Section	100

7.1.2	Differential Cross Sections of Other D Mesons	105
7.1.3	D Mesons Ratios	109
7.2	Total Cross Sections of D Mesons	111
7.2.1	Visible Cross Sections of D Mesons	111
7.2.2	Method of Extrapolation	111
7.2.3	Total Cross Sections of D Mesons	113
7.3	P_v	116
7.4	Total Cross Section of Charm Quark Production	118
8	Summary and Outlook	121
	Bibliography	123

Contents

List of Figures

2.1	Timeline of charm production in p-p collisions, from the initial collision through to the decay of charmed hadrons.	6
2.2	Feynman diagrams of charm production in quark-antiquark process $q\bar{q} \rightarrow Q\bar{Q}$ (top) and gluon-gluon processes $gg \rightarrow Q\bar{Q}$ (bottom).	7
2.3	Parton distribution function (PDF) from MSTW (Martin-Stirling-Thorne-Watt) 2008 in Next-to-Leading Order, at two different momentum scales [27].	8
2.4	LHC parton kinematics (Q^2, x) phase space at $\sqrt{s} = 7$ TeV compared to HERA [28]. For charm production at mid rapidity, where $Q = M \approx 1.5$ GeV, the Bjorken-x of the active parton is about $\sim 3 \cdot 10^{-4}$	9
2.5	Relative abundance for hadrons with a charm quark in central rapidity $ y < 1$. The numbers are taken from PYTHIA citePYTHIA simulations in p-p collisions at 14 TeV [30].	10
2.6	Decay modes of excited charmed mesons.	11
2.7	Summary of the strong coupling constant α_S measured in different experiments, as a function of energy scale [33]. A clear signature of the energy dependence of α_S is observed, which is consistent with the feature of asymptotic freedom at large values of Q	13
2.8	Peterson's fragmentation function, with $\epsilon_c = 0.06$ and $\epsilon_b = 0.006$	17
2.9	Breakdown of the different components of the uncertainty on $d\sigma/dp_T$ for charmed and beauty hadrons at LHC [42]. The cross sections and the uncertainties are calculated with MNR model.	22
2.10	Charm cross section calculated with FONLL and standard NLO calculations in 7 TeV p-p collisions [43].	24

2.11	FONLL calculations of the differential cross sections of D mesons at Tevatron. The data show the measurement of the D meson cross sections from CDF Run II [6]. The grey bands represent the results from FONLL. The calculation for D_s^+ is absent due to the unavailable D_s^+ fragmentation function.	25
3.1	Schematic view of the accelerator complex of CERN. This figure has been taken from [45].	30
3.2	Schematic view of the Large Hadron Collider and the four major experiments ALICE, ATLAS, LHCb and CMS. This figure has been taken from [45].	32
3.3	Integrated LHC luminosity in 2010. In the later runs, ALICE was applying horizontal separation between crossing bunches at the ALICE collision point (P2), not to exceed an instantaneous luminosity of $2 \cdot 10^{29} \text{ cm}^{-2} \text{ s}^{-1}$ and a collision probability per bunch-bunch crossing of less than 5%. This figure has been taken from [45].	34
3.4	Schematic overview of the ALICE detector. This figure has been taken from [47].	35
3.5	Pseudo rapidity coverage of the ALICE detectors [48].	35
3.6	Particle identification capabilities of the ALICE detectors as a function of particle transverse momentum [48].	36
3.7	Transverse impact parameter resolution from p-p collisions. The impact parameter is the closest distance from the reconstructed collision vertex to an extrapolated particle trajectory. The plot is showing the resolution of its projection on the transverse plane, both in data and simulation.	38
3.8	TPC transverse momentum resolution measured with events from cosmic rays. This figure has been taken from [50].	40
3.9	TPC dE/dx vs momentum/charge in p-p collisions at $\sqrt{s} = 900 \text{ GeV}$	40
3.10	Relativistic particle velocity as function of momentum measured with TOF in p-p collision at $\sqrt{s} = 900 \text{ GeV}$. The dependence on particle mass is visible for the different particle species.	42
3.11	Schematic work flow of the AliRoot offline framework. This figure has been taken from [55].	45
4.1	Schematic view of the $D^{*+} \rightarrow D^0(K^-\pi^+)\pi^+$ decay [8].	50

4.2	Transverse momentum distribution of π_s^+ and D^0 mesons from $D^{*+} \rightarrow D^0 + \pi_s^+$ decays from PYTHIA simulation in p-p collisions at $\sqrt{s} = 7$ TeV.	53
4.3	Schematic view of stand-alone tracking in the ITS. Left: tracking high p_T particles; right: tracking low p_T particles [62].	54
4.4	p_T distribution of the soft pion from the D^{*+} decay. The three sets of (θ, ϕ) represent the searching window settings in the ITS stand-alone tracking. The (θ_1, ϕ_1) is the conservative setting for Pb-Pb runs, and the other two are for pp runs [62].	55
4.5	Transverse momentum distribution of tracks before selection. Magenta: all tracks from both signal and background; Blue: daughter tracks K, π from D^0 decays. The data are from a minimum bias simulation with PYTHIA.	60
4.6	Impact parameter distribution of π tracks. Gray: primary π tracks; Blue: Secondary π daughter tracks from D^0 decay; Magenta: π tracks from hyperons, e.g. Λ, Ξ , and Ω decay and from K_S^0 decay; Red: π tracks decay from \bar{p} annihilation in the beam pipe or detector material.	64
4.7	Sign of the product of the impact parameters of the two tracks from the decay of D^0 in the transverse plane. The ones with negative impact parameter products are candidates track pairs from D^0 decays	65
4.8	The product of the impact parameters of the K, π tracks from D^0 candidates. The signals are the D^0 candidates decayed from D^{*+} mesons. The background are the other D^0 candidates.	65
4.9	Distribution of the distance of closest approach of the two daughter tracks.	66
4.10	Cosine of the pointing angle between D^0 flight line and its reconstructed momentum direction. Hereby shown are the distributions of signal and background from $D^{*+} \rightarrow D^0 \pi^+$ decays.	67
4.11	The distribution of $\cos \theta^*$. Hereby shows respectively the entries of signal and background from $D^{*+} \rightarrow D^0 \pi^+$ decay. . .	68
4.12	Significance of reconstructed D^{*+} as functions of selection thresholds. The selections are applied on 6 topological variables independently. These variables are $p_T^{K, \pi}$ (a), $d_0^{K, \pi}$ (b), $d_0^K \times d_0^\pi$ (c), DCA (d), $\cos \theta_{\text{point}}$ (e), $\cos \theta^*$ (f). This was studied with 150M simulated p-p collision events with PYTHIA.	69

4.13	Top: TPC Signal of particle energy loss versus the momentum. Bottom: TOF Signal of particle velocity versus the momentum divided by the charge.	71
4.14	$\Delta m = m_{D^{*+}} - m_{D^0}$ invariant mass spectrum from p-p collisions at $\sqrt{s} = 7$ TeV without particle identification, and with a 2σ selection from the specific energy loss in the TPC, and an additional 3σ selection in the time of flight.	73
4.15	ΔM invariant mass spectrum from minimum bias p-p collisions at $\sqrt{s} = 7$ TeV, integrated over $p_T > 1$ GeV/ c and $ \eta < 0.8$	76
4.16	$\Delta m = m_{D^{*+}} - m_{D^0}$ invariant mass spectrum in 10 p_T bins from 1 GeV/ c to 24 GeV/ c for minimum bias p-p collisions at $\sqrt{s} = 7$ TeV.	77
4.16	$\Delta m = m_{D^{*+}} - m_{D^0}$ invariant mass spectrum in 10 p_T bins from 1 GeV/ c to 24 GeV/ c for minimum bias p-p collisions at $\sqrt{s} = 7$ TeV.	78
4.17	Extracted D^{*+} signal and background in $\pm 3\sigma$ region, from minimum bias p-p collisions at $\sqrt{s} = 7$ TeV. The results are shown in 10 p_T bins from 1 GeV/ c to 24 GeV/ c	79
4.18	Significances of the reconstructed D^{*+} peaks, from minimum bias p-p collisions at $\sqrt{s} = 7$ TeV. The results are shown in 10 p_T bins from 1 GeV/ c to 24 GeV/ c	80
4.19	Mean and width of $\Delta m = m_{D^{*+}} - m_{D^0}$ invariant mass peak, from minimum bias p-p collisions at $\sqrt{s} = 7$ TeV. The results are shown in 10 p_T bins from 1 GeV/ c to 24 GeV/ c . The value of Δm from PDG [7] is shown in red.	80
4.20	Invariant mass spectra of D^0 and D^{*+} from minimum bias p-p collisions at $\sqrt{s} = 7$ TeV, integrated over $p_T > 1$ GeV/ c	82
5.1	Relative D^{*+} yield as each step in the reconstruction procedure. The yield is normalized to the Generated D^{*+} yield in the limited rapidity range $ y < 0.5$	86
5.2	D^{*+} reconstruction efficiency as functions of p_T (left) and y (right). The efficiencies of prompt D^{*+} and D^{*+} from decay of b-hadrons are shown separately. The prompt D^{*+} efficiency without PID is also shown as a control of PID quality.	87

5.3	Left: the detector acceptance of D^{*+} mesons as a function of p_T . The acceptance is normalized with respect to the generated D^{*+} in the rapidity range $ y < 0.5$. Right: the rapidity distributions of the generated D^{*+} mesons in the limited rapidity range $ y < 0.5$ and the generated D^{*+} mesons in the detector acceptance.	88
5.4	The product of acceptance and efficiency of D^{*+} reconstruction as a function of p_T (left). The efficiencies of prompt D^{*+} and D^{*+} from decay of b-hadrons are shown separately. The prompt D^{*+} efficiency without PID is also shown as a control of PID quality.	89
5.5	B mesons as D meson source.[64]	90
5.6	B feed-down correction factor f_c for D^{*+} , as a function of p_T . The prompt and non-prompt D^{*+} are from FONLL calculations, and the efficiencies are from PYTHIA simulation, as shown in Fig. 5.2. The uncertainty is from the FONLL calculation.	91
6.1	Systematics of yield extraction methods. The fitting method is compared with the bin counting method.	94
6.2	Systematics of PID methods. The D^{*+} yield with PID method using TPC $\pm 2\sigma$ and TOF $\pm 3\sigma$ is compared with the yield without applying any PID selection. The ratio of the yield with PID to the yield without PID is drawn in the right plot. The expected value of the ratio is drawn in red.	95
6.3	The ratio of $\frac{c \rightarrow D^{*+}}{b, c \rightarrow D^{*+}}$ to its center value. The distribution is calculation with FONLL. The error bars represent the systematic uncertainty of B feed-down calculation.	96
7.1	D^{*+} p_T differential cross section in proton proton collisions at $\sqrt{s} = 7$ TeV. The result is compared with FONLL (in red) and GM-VFNS (in blue) calculations.	102
7.2	D^0 and D^+ p_T differential cross section in proton proton collisions at $\sqrt{s} = 7$ TeV [19]. The result is compared with FONLL (in red) and GM-VFNS (in blue) calculations.	106
7.3	D_S^+ p_T differential cross section in proton proton collisions at $\sqrt{s} = 7$ TeV. The result is compared with k_T factorization at LO [69] (in magenta) and GM-VFNS (in blue) calculations [70].	107
7.4	D^0 , D^+ and D^{*+} p_T differential cross section in proton proton collisions at $\sqrt{s} = 2.76$ TeV. The result is compared with FONLL (in red) and GM-VFNS (in blue) calculations [20]. . .	108

7.5	D^0 , D^+ and D^{*+} p_T differential cross section in proton proton collisions at $\sqrt{s} = 2.76$ TeV, compared with the scaling of the cross sections at $\sqrt{s} = 7$ TeV. The ratio of the 2.76 TeV cross section to the 7 TeV scaling is shown in the bottom [20].	109
7.6	The ratios between the D mesons as a function of p_T in pp collisions at $\sqrt{s} = 7$ TeV. The result is compared with FONLL (in red), GM-VFNS (in blue) and PYTHIA 6.4.21 with Perugia-0 tune [20].	110
7.7	The P_v values of $c\bar{d}$ D mesons in various experiment systems [6, 19, 20, 68, 73, 71]. The average of the measurement in Ref. [74] is also shown. The weighted average value is represented by the yellow band.	117
7.8	Total charm cross section as a function of colliding energy measured by various experiments in nucleon-nucleon collisions. The three data points from ALICE, ATLAS and LHCb are measured at the same energy. The horizontal displacement of the data points is drawn for reading convenience.	119

List of Tables

2.1	Table of charmed hadrons. These numbers have been taken from [7].	10
3.1	LHC schedule of operation with p-p and Pb-Pb collisions. . . .	33
3.2	Parameters of the various silicon detector types of ITS. A module represents a single sensor element [47].	37
4.1	Main D^0 decay channels. These channels are often used in D^0 reconstructions. These numbers have been taken from [7]. . . .	52
4.2	D^{*+} decay channels. These numbers have been taken from [7].	52
4.3	List of parameters used for track selection. Only tracks passing all these selection criteria are used for D^0 reconstruction. . . .	61
4.4	Optimized thresholds of the topological selections in various p_T intervals.	70
4.5	TPC and TOF PID criteria for a given track (valid for both kaon and pion).	72
4.6	The reconstructed yields of $D^{*+} + D^{*-}$ signal and background in 10 p_T intervals. The corresponding significances ($\frac{\text{signal}}{\sqrt{\text{signal}+\text{background}}}$) are shown as well.	76
5.1	Total yield, average rapidity density for $ y < 1$, for hadrons with charm and beauty from PYTHIA simulations in p-p collisions at $\sqrt{s} = 14$ TeV [30].	90
6.1	Summary of the systematic uncertainties of D^{*+} cross section in the p_T intervals in the range $1 < p_T < 24$ GeV/c.	98

7.1	p_T -differential cross sections and mean p_T of D^{*+} meson in each p_T bins. The data are measured by the ALICE experiment in p-p collisions at 7 TeV. The values correspond to the data points in Fig. 7.1. The systematic uncertainties from the normalization and the decay branching ratio are not included.	103
7.2	Summary of the visible cross sections of the D mesons measured by the ALICE experiment in p-p collisions at 7 TeV and 2.76 TeV. The visible cross sections are in the rapidity range $ y < 0.5$. The systematic uncertainties from the normalization and the decay branching ratio are not included.	112
7.3	Summary of the extrapolation factors of D mesons calculated with FONLL in p-p collisions at 7 TeV and 2.76 TeV. Both the extrapolation factors for total cross section σ_{tot}^D and rapidity differential cross section $\frac{d\sigma}{dy} _{y=0}$ are listed.	114
7.4	Summary of the total cross sections of D mesons measured by the ALICE experiment in p-p collisions at 7 TeV and 2.76 TeV.	115
7.5	Summary of the $\frac{d\sigma}{dy} _{y=0}$ of D mesons measured by the ALICE experiment in p-p collisions at 7 TeV and 2.76 TeV.	115
7.6	Total charm cross sections in proton-proton collisions at 7 TeV and 2.76 TeV measured by ALICE experiment. The total cross section is extrapolated from the D^0 , D^+ and D^{*+} cross section at mid-rapidity.	119

Chapter 1

Introduction

Quantum chromodynamics (QCD) is the theory of strong interactions. It has two remarkable features. One is asymptotic freedom [1, 2], i.e. the interaction between quarks weakens as they get closer to each other. The other is color confinement, which prohibits single color charge in vacuum.

The asymptotic freedom reveals that the strong interaction is very small at high energy scales, where the strong coupling constant $\alpha_s \ll 1$. This enables perturbative methods to be applied in QCD calculations. Perturbative QCD (pQCD) has successfully calculated the R ratio in e^+e^- annihilation. However, it is not applicable when low-energy interactions are involved in the process, e.g. the initial state in hadron collisions. The factorization theorem makes the calculation possible for wider circumstances. It states that one may treat the short-range and long-range processes, the short-lived and long-lived interactions, and the high-energy and low-energy scales separately.

The calculation of heavy-flavor (c, b) quark cross sections in hadro-production is a good application of pQCD and factorization theorem. The hard processes of heavy quark production are eligible for pQCD calculation, since their energy scales are much larger than the QCD scale Λ_{QCD} . On the other hand, the factorization theorem makes it possible to take the non-perturbative processes of particle distribution function and hadronization fragmentation function into account separately.

The charm cross section in high energy hadron collisions has been a remaining challenge in pQCD calculations. First, the charm cross section from calculations is less precise than the bottom cross section, since the energy scale is not as large. Second, the parton distribution function at low Feynman- x regime is not well understood. Third, the high collision energy introduces a second energy scale, which causes the differential cross section at high momentum to not be reproduced by a standard NLO pQCD

calculation. The third difficulty is solved by introducing a resummation of the logarithmic terms into the NLO pQCD calculation. Models (e.g. FONLL [3], GM-VFNS [4]) with resummation have successfully reproduced the high momentum cross section distribution measured by CDF [5, 6]. However, the problems associated with calculations of the low momentum differential charm cross section and the total charm cross section remain.

The Large Hadron Collider (LHC) at CERN near Geneva, Switzerland, provides proton-proton collisions at the world's highest center-of-mass energy $\sqrt{s} = 7$ TeV in the runs during 2010 and 2011 (8 TeV in the run of year 2012). Additionally, it provides lead-lead collisions at center-of-mass energies up to $\sqrt{s_{NN}} = 2.76$ TeV per nucleon-nucleon pair. At these energies, heavy quarks are produced in abundance. Compared to the previously highest energies in nucleus-nucleus collisions achieved at the Relativistic Heavy Ion Collider (RHIC) at Brookhaven National Laboratory in Upton, New York, the production of charm quarks (bottom quarks) is roughly ten times (100 times) larger at the LHC.

The dominant fraction of charm quarks emerges in open charm hadrons, e.g. D mesons, while hidden charm hadrons, e.g. J/ψ , carry roughly one percent of the total charm yield [7]. At the LHC, the ALICE experiment measures most of the heavy quark hadrons in both proton-proton and lead-lead collisions. Open charmed hadrons are identified by measuring their displaced decay vertex [8] with high spatial resolution with help of the inner tracking system (ITS) of ALICE.

In lead-lead collisions, heavy-flavor (c, b) quarks are excellent tools to study the degree of thermalization of the initially created matter [9]. The critical temperature and density are exceeded, allowing quarks and gluons to be freed from their hadronic boundary and form a deconfined phase of matter – a quark gluon plasma (QGP) [10, 11].

The large masses of heavy quarks are almost exclusively generated through their coupling to the Higgs field in the electro-weak sector, while the masses of the light quarks (u, d, s) are dominated by spontaneous breaking of chiral symmetry in QCD. This means that in a QGP, where chiral symmetry might be restored, light quarks are left with their bare current masses while heavy-flavor quarks remain heavy. Due to their large masses ($\gg \Lambda_{\text{QCD}}$), heavy quarks are dominantly created in early stage perturbative QCD processes. The overall number of heavy quarks is conserved since their heavy mass is much larger than the maximum temperature of the medium. Thus thermal production is negligible. Also, cross sections for heavy quark-antiquark annihilation are marginal [12].

Frequent interactions at the partonic stage will cause these heavy quarks to participate in collective motion [13, 14, 15] and finally kinetically

equilibrate. This led to the idea of statistical hadronization of charm quarks [16]. At high momentum, charm and bottom quarks propagating through the medium provide another tool for probing the medium, e.g. the gluon density [17]. Due to their large mass, novel effects have been predicted [18].

The work presented in this thesis is the full reconstruction of the D^{*+} (2010) via the hadronic decay channel $D^{*+} \rightarrow D^0(K^-\pi^+)\pi^+$ and charm production cross section in proton-proton collisions at $\sqrt{s} = 7$ TeV, measured with the ALICE detector in mid-rapidity. This work was performed in collaboration with the ALICE group, and has been part of three publications by the ALICE collaboration [19, 20, 21].

This thesis is organized as follows. Chapter 2 gives a brief overview of heavy quark physics in proton-proton collisions. Chapter 3 addresses the Large Hadron Collider and its four main experiments with a closer look at the ALICE detector. The data sample and the ALICE offline data processing flow in the simulation and the reconstruction are also shown. In Chapter 4, the reconstruction of D^{*+} via the hadronic decay channel $D^{*+} \rightarrow D^0(K^-\pi^+)\pi^+$ in p-p collisions is shown, with the yield extraction selection method. Chapter 5 presents the study of the correction, explaining how the efficiency is obtained. The systematic uncertainty is discussed in Chapter 6. Chapter 7 presents the differential and integrated charm production cross sections in p-p collisions, which is the result of this work. Comparison is given to other measurements from ALICE, e.g. $D^0 \rightarrow K^-\pi^+$, $D^+ \rightarrow K^-\pi^+\pi^+$ and $D_S^+ \rightarrow \phi(K^-K^+)\pi^+$. A summary and outlook is given in Chapter 8.

Chapter 2

Charm Production in Hadron Collisions

The quark model was first proposed by Murray Gell-Mann [22] and George Zweig [23] independently in 1964, to classify the numerous discovered hadrons using sub-nuclear particles known as quarks. They considered only three quarks (up, down, and strange). The fourth one was first suggested by James Bjorken and Sheldon Glashow [24] and named charm quark. The first discovered particle containing charm quarks is the J/ψ meson, which was found independently in $e^+ - e^-$ collisions at the Stanford Linear Accelerator Center (SLAC) [25] and in p-Be collisions at Brookhaven National Laboratory (BNL) [26] in 1974.

In this chapter, the charm production in proton-proton collisions is discussed first. The calculation of its cross section using perturbative QCD is described in detail. Furthermore, several pQCD calculation models are introduced. Finally, the charm production in heavy ion collisions is briefly described, where we focus on the effects of the interactions between charm quarks and the medium.

2.1 Charm Production in p-p Collisions

Timeline

The typical production of charm quarks in p-p collisions is schematically illustrated in Fig. 2.1. The starting time is defined as the point when the two projectile protons meet each other in the beam direction, coinciding with the strong interaction occurring between the colliding partons. Charm-anticharm quark pairs are produced from the kinetic energy of the partons.

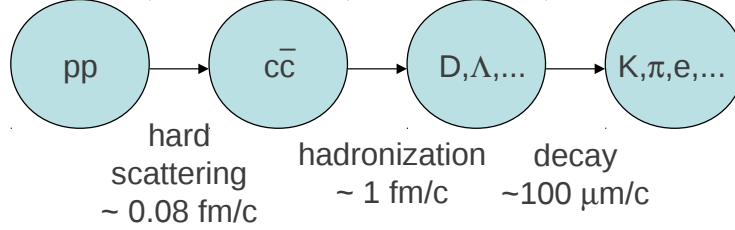


Figure 2.1: Timeline of charm production in p-p collisions, from the initial collision through to the decay of charmed hadrons.

The formation time of the quark pair is related to their Compton wave length. We can give a rough estimation that the charm quark is produced at $t \approx \hbar/2m_c c^2 \sim 0.08 \text{ fm}/c$. The produced quarks can not live individually. Due to the confinement of the color charge, the quarks are confined into hadrons. The process that the produced quarks and anti-quarks combine into hadrons is named hadronization. It occurs at a time which corresponds to the size of a hadron ($t \approx R/c \sim 1 \text{ fm}/c$). Hadronic resonances in excited states are unstable and decay via strong processes into ground state hadrons. The decays of these excited hadrons occur $\sim 1 \text{ fm}/c$ after their creation. No flavor number is changed in the strong decay, and the net charm quark remains in the hadron. After $\sim 100 \mu\text{m}/c$, the charmed hadron in the ground state decays through weak interaction. It has $\sim 95\%$ probability of decaying into a strange quark s , and $\sim 5\%$ probability of decaying into a down quark d [7]. The daughter particles of the decay are then detected in the experiments.

Hard Scattering

In proton-proton collisions, the initial interaction happens between two partons, one from each projectile proton. The interaction is a strong process, where charm quarks are produced in pairs, a charm quark and an anti-charm quark, because flavor number is conserved. The combination of the two interacting partons that produce charm-anticharm quark pair can be gluon-gluon or quark-antiquark. Some Feynman diagrams of quark-antiquark and gluon-gluon processes are drawn in Fig. 2.2.

There are infinitely many possible processes, which can not be listed one by one. In the calculations, we consider only the dominant processes. The processes are sorted by the order of strong coupling constant in the Feynman diagram. For example, pair creation and quark fusion are Leading Order

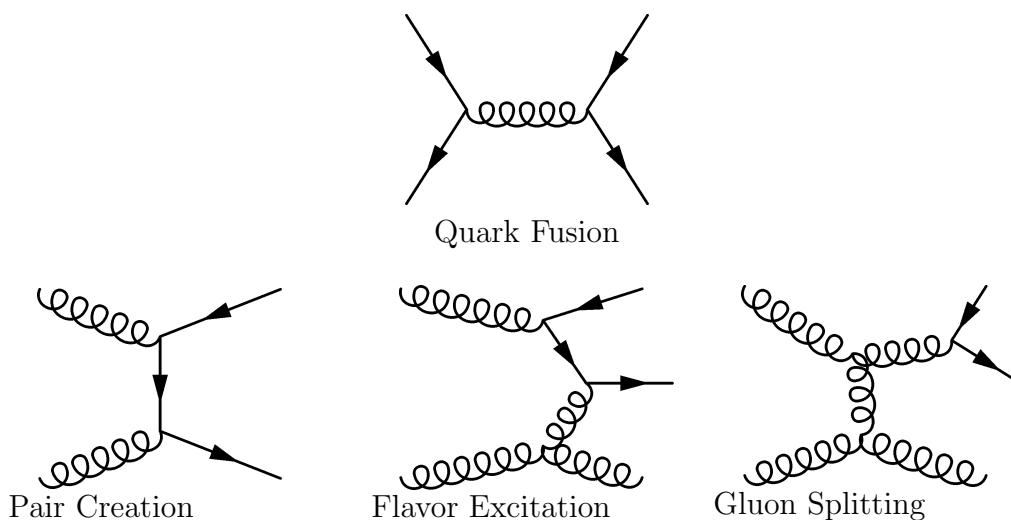


Figure 2.2: Feynman diagrams of charm production in quark-antiquark process $q\bar{q} \rightarrow Q\bar{Q}$ (top) and gluon-gluon processes $gg \rightarrow Q\bar{Q}$ (bottom).

(LO) processes. Flavor excitation and gluon splitting are Next-to-Leading Order (NLO) processes. There are higher order processes NNLO, NNNLO, etc., but their cross sections are highly suppressed, when the strong coupling constant is very small ($\alpha_S \ll 1$). These terms will be discussed again in the next section, where perturbative QCD calculations are introduced.

Within the limited acceptance of the detector, the full reconstruction of charmed hadrons is limited in a certain rapidity region. Given a certain collision energy of the proton beams, the hard processes that can be measured in a rapidity region correspond to the colliding partons in a certain phase space of momentum transfer Q^2 and momentum fraction Bjorken- x . The parton kinematics in 7 TeV p-p collisions at LHC is shown in Fig. 2.4. With increasing beam energy, the lowest x -value of the active parton decreases, when a fixed rapidity range is considered.

At LHC energies, the $c\bar{c}$ quark pair at mid rapidity is produced from the partons with typically $x \sim 10^{-4}$, where the gluon contribution dominates the parton distribution function, as displayed in Fig. 2.3. Hence, the gluon-gluon processes ($gg \rightarrow Q\bar{Q}$) are dominant in charm production at LHC at mid-rapidity, compared to quark-antiquark ($q\bar{q} \rightarrow Q\bar{Q}$) processes.

Hadronization

A color-charged particle can not exist alone freely. After the creation of a heavy quark in the initial hard process in a p-p collision, it will hadronize quickly (~ 1 fm/ c). The interaction between two quarks is described by the

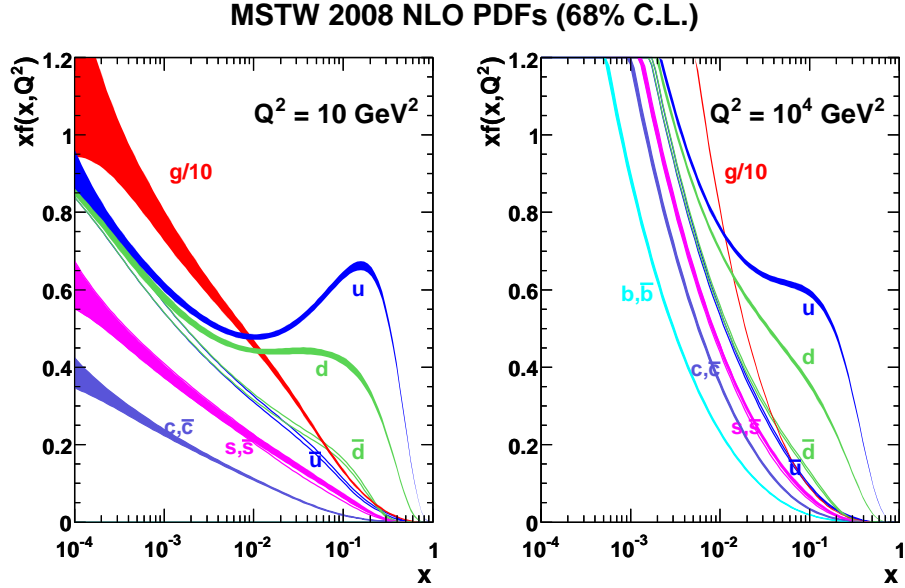


Figure 2.3: Parton distribution function (PDF) from MSTW (Martin-Stirling-Thorne-Watt) 2008 in Next-to-Leading Order, at two different momentum scales [27].

strong force, which increases with distance. The large strong force energy potential binds the two into a meson, and in some cases, binds three quarks into a baryon.

Figure 2.5 shows the relative abundance of charmed hadrons in the rapidity range $|y| < 1$. Charm quarks hadronize into D mesons, Λ_c baryons and hidden charmed mesons. These fragmentation fractions are measured from other experiments and then fitted with parametrized functions. The Review of Particle Physics [7] lists the fragmentation fractions of charm quark to D mesons as,

$$\begin{aligned}
 f(c \rightarrow D^0) &= 0.557 \pm 0.023, \\
 f(c \rightarrow D^+) &= 0.226 \pm 0.010, \\
 f(c \rightarrow D^{*+}) &= 0.238 \pm 0.007.
 \end{aligned}
 \tag{2.1}$$

Decay of Charmed Hadrons

Charmed hadrons have non-zero net charm flavor number, so they are also named open charmed hadrons. This is in contrast to hidden charmed hadrons, which have charm quarks but a zero net charm flavor number. Table 2.1 shows a list of open charmed hadrons with their intrinsic physical

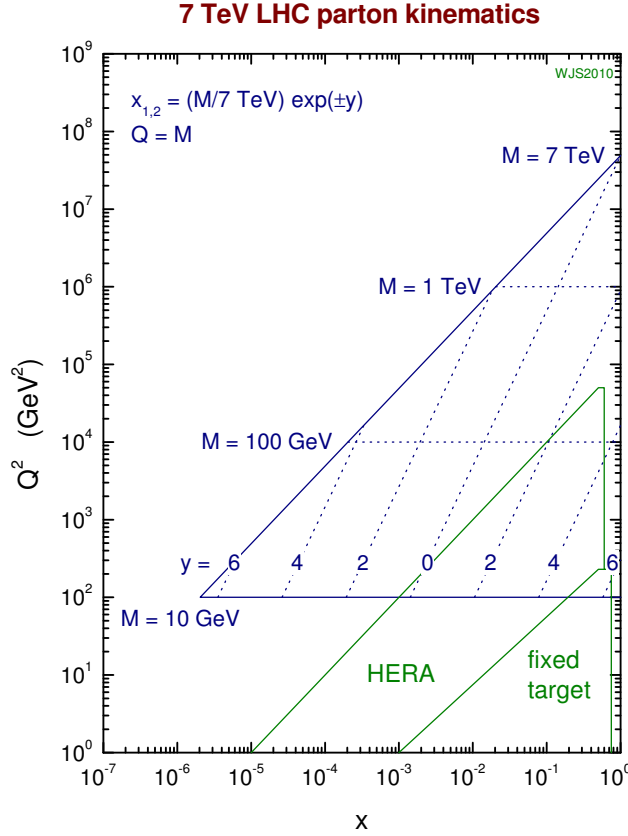


Figure 2.4: LHC parton kinematics (Q^2, x) phase space at $\sqrt{s} = 7$ TeV compared to HERA [28]. For charm production at mid rapidity, where $Q = M \approx 1.5$ GeV, the Bjorken- x of the active parton is about $\sim 3 \cdot 10^{-4}$.

characteristics. The list contains only the mesons with a charm quark. The corresponding charge conjugates containing an anti-charm quark are not given.

The D mesons consist of a charm quark and a light (u, d, s) anti-quark. The Λ_c and Σ_c baryons consist of a charm quark and two other light quarks. As shown in Table 2.1, the charmed hadrons are not stable, as their mean lifetime is rather short. The excited charmed hadrons decay via strong interaction, and their Breit-Wigner decay widths are smaller than the order of ~ 1 MeV, which corresponds to a mean lifetime of about ~ 200 fm/ c . The other charmed hadrons, which decay via weak interaction, have mean lifetimes on the order of about ~ 100 μ m/ c .

Decay of Excited-State Charmed Hadrons

The mesons in excited states, named D^* mesons, decay strongly into lower

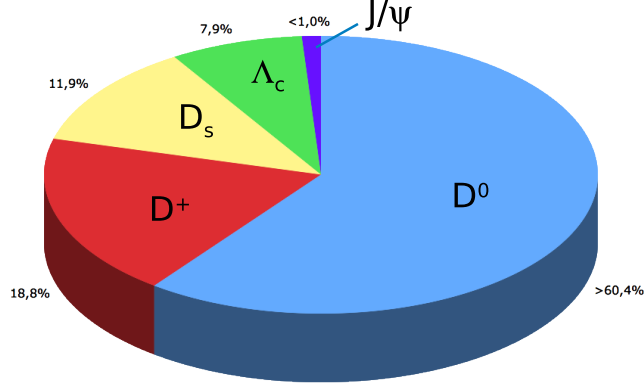


Figure 2.5: Relative abundance for hadrons with a charm quark in central rapidity $|y| < 1$. The numbers are taken from PYTHIA citePYTHIA simulations in p-p collisions at 14 TeV [30].

Charmed Hadron	Valence Quark	$I(J^P)$	Rest Mass (MeV/ c^2)	Life Time / Decay Width
D^0	$c\bar{u}$	$\frac{1}{2}(0^-)$	1864.86 ± 0.13	$c\tau = 122.9 \mu\text{m}$
D^+	$c\bar{d}$	$\frac{1}{2}(0^-)$	1869.62 ± 0.15	$c\tau = 311.8 \mu\text{m}$
D_s^+	$c\bar{s}$	$0(0^-)$	1968.49 ± 0.32	$c\tau = 149.9 \mu\text{m}$
D^{*0}	$c\bar{u}$	$\frac{1}{2}(1^-)$	2006.98 ± 0.15	$\Gamma < 2.1 \text{ MeV}$
D^{*+}	$c\bar{d}$	$\frac{1}{2}(1^-)$	2010.28 ± 0.13	$\Gamma = 96 \text{ keV}$
D_s^{*+}	$c\bar{s}$	$0(?^?)$	2112.3 ± 0.5	$\Gamma < 1.9 \text{ MeV}$
Λ_c^+	cdu	$0(\frac{1}{2}^+)$	2286.46 ± 0.14	$c\tau = 59.9 \mu\text{m}$
Σ_c^{++}	cuu	$1(\frac{1}{2}^+)$	2453.98 ± 0.16	$\Gamma = 2.26 \text{ MeV}$
Σ_c^+	cdu	$1(\frac{1}{2}^+)$	2452.9 ± 0.4	$\Gamma < 4.6 \text{ MeV}$
Σ_c^0	cdd	$1(\frac{1}{2}^+)$	2453.74 ± 0.16	$\Gamma = 2.16 \text{ MeV}$

Table 2.1: Table of charmed hadrons. These numbers have been taken from [7].

(or ground) states, where the charm flavor still exists in the final state after the decay. The decay scheme of the charmed mesons from J_1 ($D^{*0}, D^{*\pm}$) to J_0 (D^0, D^\pm) state is shown in Fig. 2.6. The orbital quantum number L of these D mesons is equal to 0, so the angular quantum number is equal the spin $J = S$. The D^{*0} mesons decay to D^0 mesons, and the $D^{*\pm}$ mesons decay to D^0 or D^\pm mesons. The width of the D^{*0} meson is $< 2.1 \text{ MeV}$, and that of the $D^{*\pm}$ meson is 96 keV . We can easily deduce their mean lifetimes

$\tau \sim 10^{-21}$ s ~ 1 pm/c from the mass width-life time relation $\tau = \frac{\hbar}{\Gamma}$. Thus they decay almost immediately after their creation in the collision, and the distance they travelled away from the collision vertex is not noticeable with current experimental methods.

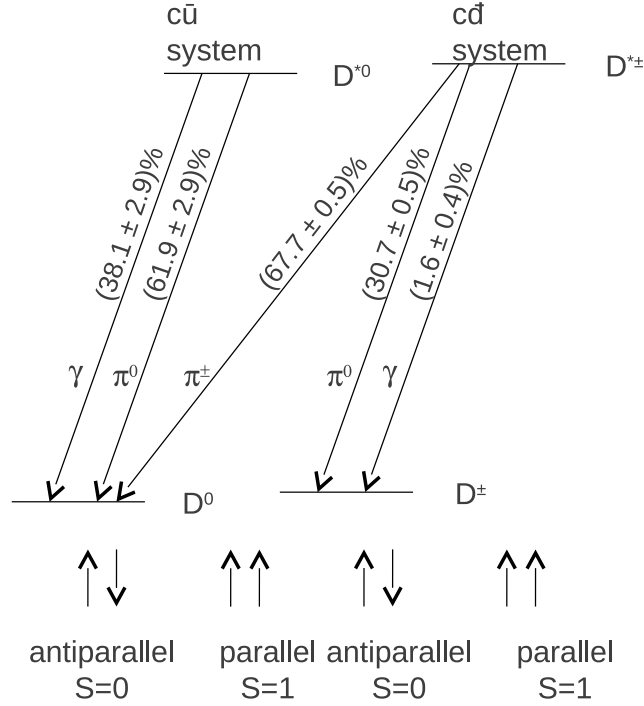


Figure 2.6: Decay modes of excited charmed mesons.

Decay of Ground-State Charmed Hadrons

The ground state charmed mesons, e.g. D^0 and D^\pm , can only decay via weak interactions. Compared to the decays of D^* mesons via the strong force, these ground state D mesons have much longer lifetimes, and their flight distances before decaying is measurable using precise tracking detectors. If the daughters of a decay are all detected, the charmed hadron are kinematically fully reconstructed via this channel. Some of these channels have significant branching ratios, and are used for charmed hadron reconstruction in experiments. Their branching ratios are listed below [7]:

$$\begin{aligned}
 \mathcal{B.R.}(D^0 \rightarrow K^- \pi^+) &= 3.88 \pm 0.05\%, \\
 \mathcal{B.R.}(D^+ \rightarrow K^- \pi^+ \pi^+) &= 9.13 \pm 0.19\%, \\
 \mathcal{B.R.}(D_s^+ \rightarrow K^+ K^- \pi^+) &= 5.49 \pm 0.27\%.
 \end{aligned}
 \tag{2.2}$$

These charged kaons and pions from the decays of D mesons can be detected by tracking detectors in a magnetic field. These tracks can be identified by the fact that they originate from the decay vertex of D mesons, which results in an impact parameter $\sim 100 \mu\text{m}$ to the primary collision vertex. The identification of these particles requires high spatial resolution detection in the vicinity of the primary vertex.

2.2 Perturbative QCD in Heavy Quark Production

Given asymptotic freedom [31] as a key characteristic of the strong force, the strong coupling constant α_S is small at short distance (i.e. high energy) interactions, see Fig. 2.7. This allows perturbative methods to be applied in calculations of these short distance strong interactions. One of these applications is heavy quark production in hadron collisions [32]. The hard interaction cross section of heavy quark production $\hat{\sigma}$ can be calculated perturbatively. Its perturbative expansion in terms of α_S is:

$$d\hat{\sigma} = d\hat{\sigma}^{(0)} + \alpha_S d\hat{\sigma}^{(1)} + \alpha_S^2 d\hat{\sigma}^{(2)} + \dots \quad (2.3)$$

The prerequisite to make $\hat{\sigma}$ calculable in perturbative QCD (pQCD) is the heavy quark mass M , for two reasons listed in the following:

- The gluon emission of a moving quark is suppressed in the cone $\theta < m/E$. For a heavy quark, its mass M provides a cut-off of collinear divergence. This ensures that the heavy quark cross section is finite in the pQCD calculation. On the other hand, for a light quark with a mass $m \sim 0$, the collinear gluon emission are not calculable in a fixed order pQCD calculation.
- M is much larger than the QCD scale. The strong coupling constant is $\alpha_S \sim \ln(\frac{\mu}{\Lambda_{QCD}})^{-1}$. In the heavy quark hadro-production process, the energy scale μ of the process is of the order of the heavy quark mass M . In order to make the powers of α_S small in the expansion, M should be large compared to the QCD scale Λ_{QCD} . The QCD scale Λ_{QCD} defines a scale where the coupling constant becomes large, and $\Lambda_{\overline{MS}}(N_f = 5) = 213 \pm 8 \text{ MeV}$ [33], where N_f is the number of active quark flavors.

The production cross sections of charm, bottom and top quarks meet these prerequisites and allow to be calculated perturbatively. These quarks

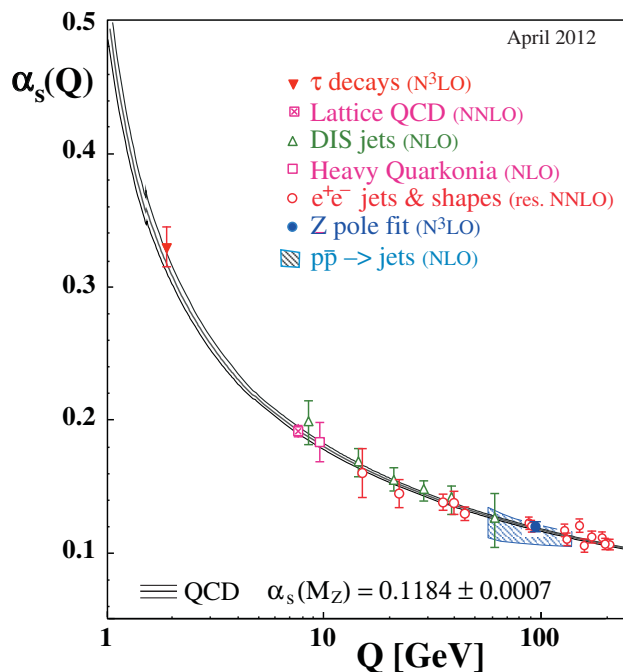


Figure 2.7: Summary of the strong coupling constant α_S measured in different experiments, as a function of energy scale [33]. A clear signature of the energy dependence of α_S is observed, which is consistent with the feature of asymptotic freedom at large values of Q .

are much heavier than Λ_{QCD} , and are called heavy quarks. The other three quarks are considered light quarks. The production cross sections of light quarks are calculable with pQCD only when the momentum is larger than the QCD scale.

In the pQCD calculation of the productions of each heavy quark flavor, the perturbative effects are different due to their different masses. The heavier the mass is, the smaller the strong coupling constant becomes, and thus the smaller the high order corrections of $\mathcal{O}(\alpha_S^n)$ are. Hence, given the perturbative calculation at the same order, the uncertainty of the charm cross section calculation is larger than that of bottom, and even larger than that of top.

The mass of the quark M defines the scale of the strong coupling, which is the relevant scale when one calculates the total cross section. If one wants to calculate differential cross sections in p_T, y phase space, one will have to face another scale of energy of the quark E (or transverse momentum p_T). E and p_T are correlated. In high-energy hadron collisions, we have to deal with the fact that the scale of E and p_T can be much larger than the scale of the heavy

quark mass. Also, at a fixed collision energy, the charm production involves partons with much lower Bjorken- x value than the bottom and the top. The uncertainty of parton distribution at low x addresses larger uncertainty of the charm cross section in hadron collisions.

Factorization

The hard scattering process of charm production happens in a very small space-time scale, while the hadronization process is a long distance interaction. The strong coupling constant is very small ($\alpha_S \ll 1$) at short distance (ultraviolet side (UV) in spectroscopy), and becomes large ($\alpha_S \sim 1$) at long distance (infrared side (IR) in spectroscopy), see Fig. 2.7. The distinct behavior of the strong interaction in these two regimes enables us to calculate them separately, separating the hard process and the hadronization. This separation is called factorization. The factorization scale μ_f is introduced to enable the calculations in both the short and long distance regimes. The short distance process are calculated with perturbative methods. The factorization scale is arbitrary, as there is no clear border between short distance and long distance. In pQCD models, the value of the factorization scale are chosen to minimize the perturbative uncertainties.

In proton-proton collisions, the production of charmed hadrons is calculated as,

$$d\sigma(pp \rightarrow D + X) = \sum_{i,j} \int dx_1 dx_2 dz f_i(x_1, \mu_f) f_j(x_2, \mu_f) \times d\hat{\sigma}_{ij \rightarrow cX}(\alpha_S, x_1, x_2, \mu_f) \times D_c^D(z), \quad (2.4)$$

where i and j are the colliding partons, carrying a fraction x of the momentum of the proton; c is the outgoing charm quark. The calculation of the charm hadron cross section in pp uses three ingredients:

- The parton distribution function (PDF) $f(x, \mu)$, which is the probability density that a parton has a fraction x of the the proton momentum in the Breit frame, as shown in Fig. 2.3;
- The cross section of hard partonic interaction $d\hat{\sigma}_{ij \rightarrow cX}$ of the charm quark production;
- The charm-to-hadron ($c \rightarrow D$) fragmentation function (FF) $D_c^D(z)$, which is the probability density that a charmed hadron carrying a certain proportion of the momentum of its parent charm quark. The parameter z is the ratio of the momentum of the D hadron to the momentum of the c quark.

The PDF of a proton and FF are assumed to be universal functions and do not depend on the collision system or energy. The proton PDF is mostly measured in Deep Inelastic Scattering (DIS), and FF is measured in $e^+ - e^-$ collisions. However, there are singularities in two regimes of the calculation. They are:

- UV singularities due to the infinite loop diagrams;
- IR singularities due to soft gluon emissions;
- Collinear singularities due to collinear gluon emissions.

The soft and collinear singularities are absorbed into the PDF by using the factorization theorem, while the UV singularities are absorbed into the strong coupling constant by using renormalization.

Renormalization

In pQCD calculations, the UV singularities remain, even after the factorization method has been applied. The contribution of these loop diagrams may cause unrealistic infinite momenta. Thus renormalization is needed in the calculation. By including the integration up to an energy scale limit μ_r , the ultraviolet singularities from the loop diagrams are absorbed into the strong coupling constant α_s . The renormalization scale μ_r defines the scale of the strong coupling constant in pQCD calculations.

Modified PDF

The distributions of partons in a proton are non-perturbative features. However, to deal with the soft collinear infinities, the PDFs are included into perturbative calculations. By reproducing the modified parton distribution functions, the singularities in the long distance regime are absorbed in the bare parton distribution functions. Some of the soft and collinear singularities appear both in the virtual and real gluon emission diagrams, and their integration over the emitted partons cancel each other out. The remaining singularities are absorbed into the parton distribution function. The factorization scale μ_f acts as an ultraviolet cutoff of the emitted soft gluons.

In the calculation of heavy quark production, the modifications used to absorb the singularities are applied on two aspects. One is by including the heavy quark in the initial state. Heavy quark pairs are created from gluon splitting in the proton. The modified heavy quark distribution function is thus calculable with perturbative methods. The other is by including a

perturbative fragmentation function, which defines the kinetic relation from a light parton to a heavy quark. It is worth noting that this fragmentation function is different from the quark-to-hadron fragmentation function. The light-parton-to-heavy-quark fragmentation function is perturbatively calculable, whereas the non-perturbative quark-to-hadron fragmentation function must be extracted from experiments and its distribution at other scales must be calculated with evolution equations. With these modifications, the soft collinear singularities are absorbed in the perturbative heavy quark PDF and the perturbative light-parton-to-heavy-quark fragmentation function.

In pQCD calculations, the modified PDF is described as a running parton distribution function $f(x, \mu_f)$, in terms of parton momentum fraction x of the proton and the factorization scale μ_f . We can not get the absolute value of $f(x, \mu_f)$ from pQCD calculations. However, by using the DGLAP evolution equation [34], we are able to determine its μ_f dependence.

In practice, a PDF is measured at a given scale μ_0 . Then the evolution equations are solved to determine the PDF at other scales. The parton splitting function in the evolution equation depends on α_S , and needs to be calculated perturbatively. It is expressed as a power series of α_S . Currently, the calculation of the DGLAP evolution equation has been up to the precision level of NNLO.

Fragmentation Function

Hadronization is a soft process that happens $\sim 1fm/c$ after the parton scattering. The factorization theorem indicates that it is independent from the hard scattering process, both in time scale and energy scale. A fragmentation function, which links the kinematics of the quark and the hadron, must be modelled to meet the experimental results. The hadronization process can not be calculated perturbatively, given the fact that it is a long distance interaction. The quark-to-hadron fragmentation function is measured from experiments and parametrized in different models.

One example of a non-perturbative quark-to-hadron fragmentation function model is that from C. Peterson [35]. It is parametrized as the ratio between the hadron energy and the incident quark energy. Thus, this fragmentation function is assumed to be universal, as it does not depend on the absolute energy of the quark. Peterson's fragmentation function is parametrized as

$$D_Q^H(z) \propto \frac{1}{z(1 - (1/z) - \epsilon_Q/(1 - z))^2}, \quad (2.5)$$

where $D_Q^H(z)$ is the quark-to-hadron fragmentation function representing the fragmentation probability density, $z = E_H/E_Q$, E_H is the outgoing hadron energy, and E_Q is the incoming heavy quark energy. Although the parameter ϵ_Q corresponds to $(m_q/m_Q)^2$, it is taken in practice as a free parameter and is then fitted to experimental results. For charm and beauty quarks, $\epsilon_c = 0.06$ and $\epsilon_b = 0.006$ are commonly used values in this calculation.

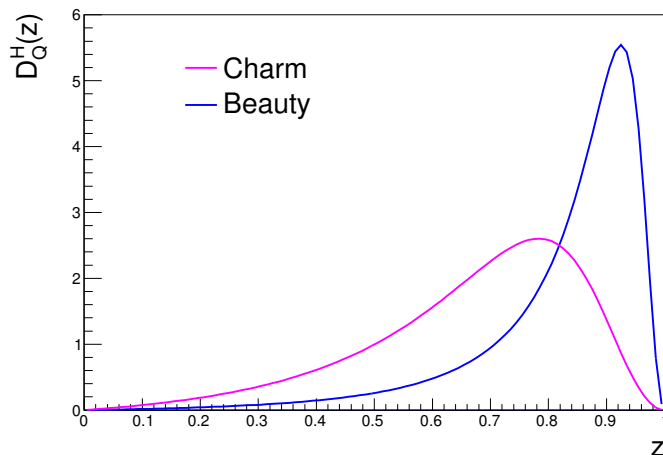


Figure 2.8: Peterson's fragmentation function, with $\epsilon_c = 0.06$ and $\epsilon_b = 0.006$.

There are other fragmentation functions which are also commonly used, such as the Kartvelishvili-Likhoded-Petrov function [36], the Bowler function [37] and the Collins-Spiller function [38]. All of these fragmentation functions must be further constrained by experimental data.

The Scale Factors $\mu_{r,f}$

In a complete calculation, the physical cross section is independent of the choice of the μ_r and μ_f , which makes the observables (i.e. charmed hadron cross section) calculable. This key feature of pQCD is called the renormalization group equation (RGE):

$$\mu_{r,f} \frac{d\sigma}{d\mu_{r,f}} = \frac{d\sigma}{d\ln\mu_{r,f}} = 0. \quad (2.6)$$

Although the scale factors $\mu_{r,f}$ are arbitrary, their values may not be chosen freely. The RGE is valid when the physical observable is calculated in all orders, which is not feasible presently. It is obvious that the higher the orders one takes into the calculation, the less varied the calculation becomes,

and so the dependence on the choice of scale decreases. With the applicable theoretical calculation, one may calculate up to a certain precision level with different scales, and check the variation of the calculated observable.

In order to reduce the dependence of an observable on the scale as much as possible, we need to choose an optimum scale $\mu_{r,f}$ to cope with the limited precision level we have achieved. The running coupling gives a convenient way of describing the variations under the change of the interaction energy scale.

The calculation shows that the QCD corrections depend on the logarithm of the scale factor over the hard scale. To minimize the coefficient factors of the perturbative terms, the arbitrary scales should be chosen as the order of the hard scale, i.e. the charm quark mass in the case of charm production. When the differential cross section is calculated, a second scale p_T must be introduced. Thus, the scale factors are usually chosen as $\mu_{r,f} = \sqrt{M^2 + p_T^2}$, in order to match the two scales.

2.3 pQCD Calculation Models

As discussed above, pQCD calculation is only able to provide the cross section at the level of the fundamental fields of QCD. Therefore, non-perturbative inputs, the PDFs as well as the FFs, are needed to compare the theory with the actual measurements. Furthermore, the measurements does not extend over full phase space, whereas many relevant theoretical calculations are provided over large or full phase space.

In order to overcome these shortcomings and to make a comparison between the measurements and the calculations, two kinds of methods have been applied. One is to make the comparison of the total cross section. We have to apply a correction to the data. The correction is obtained either from Monte Carlo simulation or theory calculation. The correction deconvolutes the hadronization, and extrapolates the measurement to full phase space. The shortcoming of this method is its poor precision level. It depends strongly on the simulation or the theory one chooses, as the results are usually extrapolated by one or two orders of magnitude.

The other method is to use a multi-differential experimental result. The corresponding observable in the theory calculation must be refined to make a comparison possible. This method minimizes the effect of theoretical correction and extrapolation, but raises two challenges in the calculation. First, it requires a better understanding of the perturbative calculation in the regions of phase space where the pQCD has large uncertainties. Second, it requires precise non-perturbative ingredients, the PDF and FF, as inputs.

These must be extracted from data, and matched well with the calculation.

2.3.1 Resummation

The issue of scale dependence arises when the p_T differential cross section is calculated. Due to the existence of a second scale of energy E , in addition to the scale of quark mass M , a large scale dependence of the cross section at high p_T is found in a standard NLO pQCD calculation. The heavy quark production cross section can be decomposed as the following, in terms of the quark mass m over energy scale E ,

$$\sigma_Q(E, m) = \sigma_0 \left(1 + \sum_{n=1} \alpha_s^n \sum_{k=0}^n c_{nk} \ln^k \left[\frac{E^2}{m^2} + O\left(\frac{m}{E}\right) \right] \right), \quad (2.7)$$

where σ_0 is the Born cross section, c_{nk} is a coefficient that also contains functions of m and E , and c_{nk} vanishes as powers of m/E , when $E \gg m$.

The logarithmic term $\ln(E^2/m^2)$ originates from the collinear gluon emission. Its soft components are absorbed by factorization, and the rest contributes a higher order correction in the high- p_T region in the differential cross section. These higher order corrections become non-negligible in the region where $p_T \gg m$. Hence, a resummation of the higher order logarithmic terms of the pQCD calculation is important for heavy flavor p_T differential cross section calculations.

The resummation is calculated in many different ways for varying models. It may contain the resumming leading ($\alpha_s^n \ln^n(E^2/m^2)$, *LL*) or also next-to-leading ($\alpha_s^n \ln^{n-1}(E^2/m^2)$, *NLL*) logarithmic terms. State-of-the-art models like ACOT(χ) [39], FONLL [3], GM-VFNS [4], and BSMN [40] all share the same methodology.

These perturbative approaches need to omit the higher orders of the m/E terms and use a resummation factor for the logarithmic terms, which are not accurate at a low energy scale where $E \sim m$. This has been a challenge of the pQCD calculation of the heavy quark production cross section, and needs experimental data to extrapolate to the low momentum scale for comparisons. Aside from the energy scale, the uncertainty of quark masses m_Q for charm and beauty contributes to the total systematic uncertainty.

The resummation predicts a result of a massless particle, which is only valid in the $E \gg m$ region. To obtain a prediction over the full energy range, one needs to interpolate the result with a fixed order calculation, which is valid also in the $E \sim m$ range.

The available pQCD models follow this method of calculation, but differ in two aspects. One is the perturbative order evaluated in the initial PDFs.

The other is the way of matching the resummed cross section with fixed order calculations.

2.3.2 MNR

The framework MNR [41] was devised by Mangano, Nason and Ridolfi, and aimed for the description of heavy quark production in strong interactions. It provides a massive pQCD calculation in NLO accuracy. Here, “massive” means that the heavy quarks are considered massive, while the light quarks are considered massless. The resummation of the logarithmic terms is not used, thus it is classified as a standard fixed order (FO) calculation. The active flavor number in the initial state is fixed to $n_{lf} = 3$, which means that the heavy quarks only appear in the final state. For that reason, this calculation is also classified as Fixed Flavor Number Scheme (FFNS). The factorization and renormalization scales μ_f, μ_r are taken in units of μ_0 , where $\mu_0 = m_T = \sqrt{m_Q^2 + p_T^2}$. The choice of $\mu_0 = m_T$ includes both the scales of M and p_T , thereby containing both of the hard scales. This choice of μ_0 makes the differential cross section calculable.

The lack of resummation of the higher order logarithmic terms makes the cross section more scale-dependent in the region where $p_T \gg M$. While the p_T -differential cross section is less accurate in the high- p_T region, the total cross section is not significantly affected, since the total cross section is dominated by the low- p_T region. Thus, standard NLO models, e.g. MNR, are reliable for the total cross section calculations.

2.3.3 FONLL

The name of FONLL (Fixed Order plus Next-to-Leading Log resummation) explains its matching method, which matches a standard fixed order (FO) calculation at next-to-leading order with a full resummation of next-to-leading order logarithms (NLL). The FO calculation includes all the terms of order α_S^2 and α_S^3 . The resummation includes all of the leading logarithm (LL) terms $\alpha_S^2(\alpha_S \ln p_T/m)^k$ and all of the next-to-leading logarithm (NLL) terms $\alpha_S^3(\alpha_S \ln p_T/m)^k$. The matching of NLL resummation and the fixed order calculation is presented as the following,

$$\sigma_Q^{\text{FONLL}}(p_T, m) = \text{FO} + (\text{RS} - \text{FOM0})G(m, p_T), \quad (2.8)$$

where FO stands for the NLO fixed order calculation with non-zero quark mass, and RS is the resummed calculation with massless quarks. FOM0 represents the terms that are double counted both in FO and RS. The

expression of FOM0 indicates that it is calculated at the massless limit as m/p_T approaches zero. $G(m, p_T)$ is an arbitrary factor for power suppressed terms, as

$$G(m, p_T) = p_T^2 / (p_T^2 + c^2 m^2), \quad (2.9)$$

where $c = 5$. This factor is introduced because in the region of $p_T < 5m$, where the massless limit gives unreliable results, the contribution has to be suppressed. This factor does not affect the NLO+NLL accuracy, since it only applies to the the energy scale beyond the perturbation-effective region.

With more details, the FO, RS and FOM0 in Eq. 2.8 can be written as the following:

$$\begin{aligned} \text{FO} &= \sum_{i,j \in \mathcal{L}} f_i f_j \hat{\sigma}_{ij \rightarrow QX}(p_T, m), \\ \text{RS} &= \sum_{i,j,k \in \mathcal{L} + \mathcal{H}} f_i f_j \hat{\sigma}_{ij \rightarrow kX}^{\overline{MS}}(p_T) D_{k \rightarrow Q}, \\ \text{FOM0} &= \sum_{i,j \in \mathcal{L}} f_i f_j \hat{\sigma}_{ij \rightarrow QX}(p_T, m \rightarrow 0). \end{aligned} \quad (2.10)$$

The initial states applied in the calculation of FO and FOM0 terms are the light flavored PDFs, where no heavy quark participates. In the calculation of the RS term, however, heavy quarks are included in the perturbatively calculated modified PDF. Moreover, a perturbative light-parton-to-heavy-quark fragmentation function is included in the final states, which describes the fragmentation of a parton into a heavy quark. The inclusion of the modified PDF and light-parton-to-heavy-quark fragmentation function absorbs the collinear divergences.

The uncertainties of the FONLL calculation are categorized in the following:

- **Uncertainty of the Scales**

The factorization and renormalization scales μ_f, μ_r determine the running coupling constant α_S and the parton distribution function PDF. The scale factors are arbitrary parameters. We choose $\mu_f, \mu_r \sim m_T$ to minimize their effect on the calculation of the cross sections. But there are still uncertainties originating from the choice of the scales. The scaling uncertainties are determined as the region between the maximum and the minimum cross sections when varying μ_f and μ_r in the range $0.5 < \frac{\mu_f}{m_T}, \frac{\mu_r}{m_T} < 2$, while keeping the ratio within the range $0.5 < \frac{\mu_f}{\mu_r} < 2$.

- **Uncertainty of the Heavy Quark Mass**

The mass of the charm and bottom quarks are not well known, since

we only observe them in bound hadronic states. Typically, in pQCD calculations, the charm quark mass is set to $1.5 \pm 0.2 \text{ GeV}/c^2$, and the bottom quark mass is set to $4.75 \pm 0.25 \text{ GeV}/c^2$.

- **Uncertainty of Parton Distribution Function**

The gluon densities at low x and high Q^2 region in the PDF are not well constrained from existing measurement, since it requires hadronic collisions at high center of mass energies.

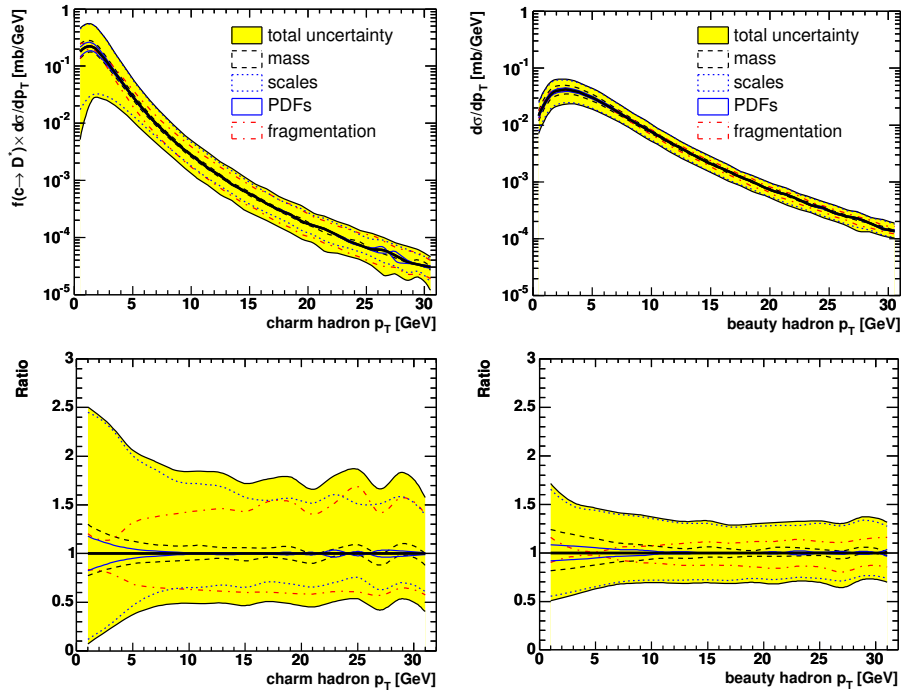


Figure 2.9: Breakdown of the different components of the uncertainty on $d\sigma/dp_T$ for charmed and beauty hadrons at LHC [42]. The cross sections and the uncertainties are calculated with MNR model.

Among these uncertainties, the one from the variation of the scales represents the perturbative uncertainty, which originates from the discarded high-order perturbative terms. The other two represent the uncertainties arises from the input, which include the Λ_{QCD} , m_c , m_b , PDF and FF.

Figure 2.9 shows the uncertainty components of the heavy flavor hadron cross sections calculated with MNR model. Comparing the uncertainties of the MNR calculation, FONLL has much smaller scale variation uncertainty in the high- p_T region. Nevertheless, the other properties of the uncertainties

are also applicable for the FONLL uncertainties, as the FONLL calculation is merely the MNR with the resummation.

The uncertainty from the scale variation is dominant, especially in the low- p_T region. This uncertainty originates from the perturbative calculation. We calculated the cross section at a certain precision level, and the higher order terms are discarded. Those discarded terms are reflected as the uncertainties from scale variation.

The perturbative uncertainty of the charm cross section calculation is much larger than the perturbative uncertainty of the beauty cross section. The difference between the beauty quark mass and the QCD scale is much larger than the difference between the charm quark mass and the QCD scale. Given the fact that the perturbative scale is chosen to be the heavy quark mass in the heavy quark cross section calculations, the perturbative method fits more in the beauty cross section calculation than in the charm cross section calculation. In another word, the higher order terms, which are discarded, are much smaller in beauty cross section calculation and are larger in charm cross section calculation.

In the charm hadron p_T -differential cross section, the uncertainty from the fragmentation function is also large, especially at high- p_T region. If we use a resummed calculation, of which the scale variation uncertainty is reduced in the high- p_T region, the fragmentation uncertainty is dominant in the high- p_T region.

The uncertainties from the quark masses and the PDFs are negligible compared to the scale variation uncertainties. The uncertainties from quark masses and the PDFs are larger in the low- p_T region, but they are still smaller than the scale variation uncertainties in that region.

The differences between FONLL and a standard NLO calculation are summarized in the following:

- **Collinear Resummation**

FONLL has a smaller scale dependence than a NLO calculation in the high- p_T region, since it provides resummed logarithmic terms in the NLL accuracy as a correction, in addition to a standard NLO calculation.

- **Zero Heavy Quark Mass**

The resummation is calculated with massless heavy quarks, while the FO calculation is still based on massive quarks. Since resummation aims only in the region where $p_T \gg m$, it is safe to assume the heavy quark massless.

- **Variable Flavor Number Scheme (VFNS)**

The renormalization and factorization scheme in FONLL is the standard modified minimal subtraction scheme (\overline{MS}), in which the heavy quark is considered to be an active quark. In the fixed order calculation FO, the number of active flavor quarks is equal to the light flavor number $n_f = n_{lf}$, which is 3 for charm cross section calculations and 4 for bottom cross section calculations. In the resummation calculation, the number of active flavors n_f is varied depending on the scale μ_f , the border of which is determined as the heavy quark mass M . This gives $n_f = 3$ if $\mu_f < m_c$; $n_f = 4$ if $m_c < \mu_f < m_b$; and $n_f = 5$ if $\mu_f > m_b$. The coupling constant α_S and PDF are modified according to the change in n_f .

The differences are due to the inclusion of the RS into the standard FO (NLO) calculation. This additional RS can be also regarded as a Zero Mass Variable flavor Number Scheme (ZM-VFNS) calculation. In the region where $p_T \gg m$, FONLL is equal to the RS (ZM-VFNS) calculation, since FO and FOM0 converge when $m/p_T \rightarrow 0$. In the region where $p_T \ll m$, FONLL is equivalent to FO (FFNS) calculation, since $\lim_{p_T/m \rightarrow 0} G(m, p_T) = 0$. In the region where $p_T \sim m$, FONLL has contributions from both FO and RS. In that region, the uncertainties from both sides contribute to the calculation.

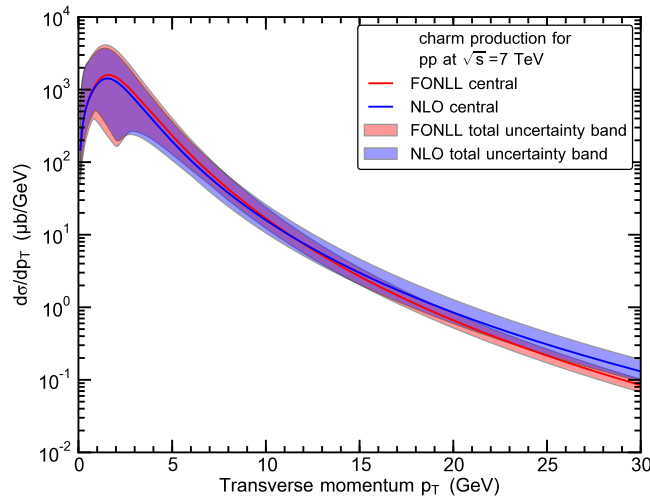


Figure 2.10: Charm cross section calculated with FONLL and standard NLO calculations in 7 TeV p-p collisions [43].

As shown in Fig. 2.11, FONLL describes the data well within its uncertainties. Due to the limitations of the perturbative calculation, the uncertainty in the low- p_T region remains large. This large uncertainty in the

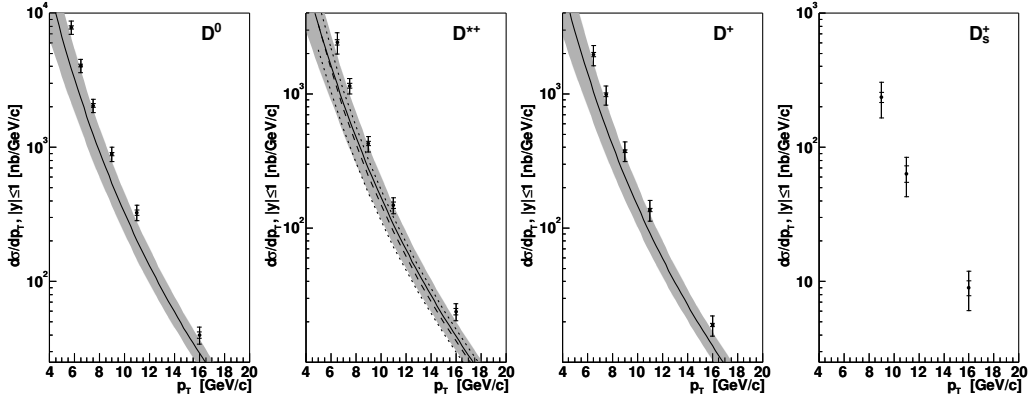


Figure 2.11: FONLL calculations of the differential cross sections of D mesons at Tevatron. The data show the measurement of the D meson cross sections from CDF Run II [6]. The grey bands represent the results from FONLL. The calculation for D_s^+ is absent due to the unavailable D_s^+ fragmentation function.

low- p_T region also exists in FO (NLO) calculation, as shown in Fig. 2.10. This leads to a large uncertainty of the total charm cross section, since most of the produced charm quarks are below 5 GeV/ c . The two models agree with each other within uncertainties, but the shape of the differential distribution is different. This is due to their different ways of handling the calculation in the high- p_T region.

2.3.4 GM-VFNS

General Mass Variable Flavor Number Scheme (GM-VFNS) uses a massless resummed calculation and combines with a massive fixed order calculation. The logarithmic terms are absorbed in the perturbatively modified PDF and light-parton-to-heavy-quark fragmentation function. In heavy flavor PDFs, the heavy quarks are considered active partons that participate in the hard scattering process. In the perturbative FF, the heavy quarks are fragmented from the light quarks. Meanwhile, the mass dependent terms are still retained in the hard process. Simply put, the GM-VFNS combines the virtues of FFNS (FO) and ZM-VFNS (RS) calculations. This idea is the same as that used in FONLL. The main difference between them is the matching method. The charmed hadron cross section in GM-VFNS calculation can be described as the following:

$$\sigma_H^{GM-VFNS}(p_T, m) = \sum_{i,j \in \mathcal{L}} f_i f_j \hat{\sigma}_{ij \rightarrow QX}(p_T, m) D_{Q \rightarrow H}^{\overline{MS}}$$

$$+ \sum_{i,j,k \in \mathcal{L}+\mathcal{H}} f_i f_j \hat{\sigma}_{ij \rightarrow kX}^{\overline{MS}}(p_T) D_{k \rightarrow H}^{\overline{MS}}, \quad (2.11)$$

where the hard cross section term $\hat{\sigma}_{ij \rightarrow QX}(p_T, m)$ is defined by:

$$\begin{aligned} \hat{\sigma}_{ij \rightarrow QX}(p_T, m) &= \tilde{\sigma}_{ij \rightarrow Q}(p_T, m) - \sigma^{sub} \\ &= \tilde{\sigma}_{ij \rightarrow Q}(p_T, m) - \tilde{\sigma}_{ij \rightarrow Q}(p_T, m \rightarrow 0) + \hat{\sigma}_{ij \rightarrow QX}^{\overline{MS}}(p_T). \end{aligned} \quad (2.12)$$

In Eq. 2.12, the cross section $\hat{\sigma}_{ij \rightarrow QX}(p_T, m)$ is calculated in a way (FO-FOM0+RS) which is similar to that in FONLL. The term σ^{sub} is the difference between the hard scattering cross section in the massless limit and the one in the genuine massless calculation. This difference, which contains the collinear logarithms, is removed from the FO cross section $\tilde{\sigma}_{ij \rightarrow Q}(p_T, m)$. In this approach, the subtraction term is convoluted with the universal non-perturbative light flavor PDF and FF.

The second term of Eq. 2.11 contains only the sub-processes that are not taken over in the first term. There, the perturbative parton PDF and light-parton-to-heavy-quark FF are applied together with the non-perturbative hadron FF, since $D_{k \rightarrow H}^{\overline{MS}} = D_{k \rightarrow Q} D_{Q \rightarrow H}$.

The differences between GM-VFNS and FONLL are summarised as the following:

- **Resummation Scheme**

In FONLL, the collinear singularities are absorbed in the perturbative PDF and light-parton-to-heavy-quark FF. In GM-VFNS, the singularities are associated with the massive quark by mass factorization, and are subtracted in the massive calculation in the massless limit.

- **Hadron Fragmentation**

FONLL calculates the heavy quark cross section. Its combination with a non-perturbative quark-to-hadron FF gives the cross section at the hadron level. However, the fragmentation used in GM-VFNS is a non-perturbative parton to hadron, whose heavy quark to hadron part has not been deconvoluted. Thus the GM-VFNS calculation is limited to only the hadron level.

- **Matching**

The FONLL model uses an artificial suppression function $G(m, p_T)$ to minimize the massless calculation in the low- p_T region, whereas GM-VFNS does not have such suppression. This implies a considerable difference between the two models in the $p_T \sim M$ region.

There are several sources of uncertainties in the GM-VFNS calculation. The uncertainty from the scale variation is the dominant one. It is also the only one illustrated in the uncertainty band. This part of the uncertainty is determined by a variation of the scales μ_r, μ_i, μ_f in the range $0.5 < \frac{\mu_r}{m_T}, \frac{\mu_i}{m_T}, \frac{\mu_f}{m_T} < 2$, while keeping the ratios within the range $0.5 < \frac{\mu_r}{\mu_i}, \frac{\mu_i}{\mu_f}, \frac{\mu_f}{\mu_r} < 2$. The region between the maximum and the minimum cross section is considered to be the uncertainty band. The variables μ_i and μ_f represent the factorization scales in the initial and final states, respectively.

The other sources of uncertainty include the uncertainty of the quark mass, and the uncertainty of the PDF and FF. Those uncertainties are much smaller than that from the scale variation [4]. Thus, they are not included in the uncertainty bracket.

Chapter 3

The LHC and ALICE

3.1 The Large Hadron Collider

3.1.1 LHC Setup

The Large Hadron Collider (LHC) located at the European Organization for Nuclear Research (CERN) near Geneva collides two counter rotating beams of protons or heavy ions at unprecedented high energy and luminosity. It is situated roughly $60 \sim 100$ m below ground in a circular tunnel of 27 km circumference. The LHC is designed to provide proton-proton collisions at luminosities of up to $10^{34} \text{ cm}^{-2} \text{ s}^{-1}$ and a maximum center-of-mass energy of $\sqrt{s}=14$ TeV [44], exceeding the maximum Tevatron energy by almost one order of magnitude. For lead-lead collisions the maximum attainable collision energy per nucleon-nucleon pair is $\sqrt{s_{\text{NN}}} = 5.5$ TeV at a design luminosity of $10^{27} \text{ cm}^{-2} \text{ s}^{-1}$. This collision energy exceeds the highest energy provided by the Relativistic Heavy Ion Collider (RHIC) at the Brookhaven National Laboratory (BNL) by a factor of 30. A Large Ion Collider Experiment (ALICE) is capable of particle tracking in high multiplicity events, which is dedicated in measuring heavy ion collisions.

A schematic overview of the CERN accelerator complex is shown in Fig. 3.1. Protons are accelerated to 90 keV and then extracted from the duoplasmatron proton-source. They are further accelerated in the linear accelerator LINAC2 up to 50 MeV and then passed to a multi ring booster synchrotron for acceleration to 1.4 GeV. In the Proton Synchrotron (PS) the bunch patterns are generated and protons reach an energy of 26 GeV. The Super Proton Synchrotron (SPS) accelerates protons to 450 GeV and serves

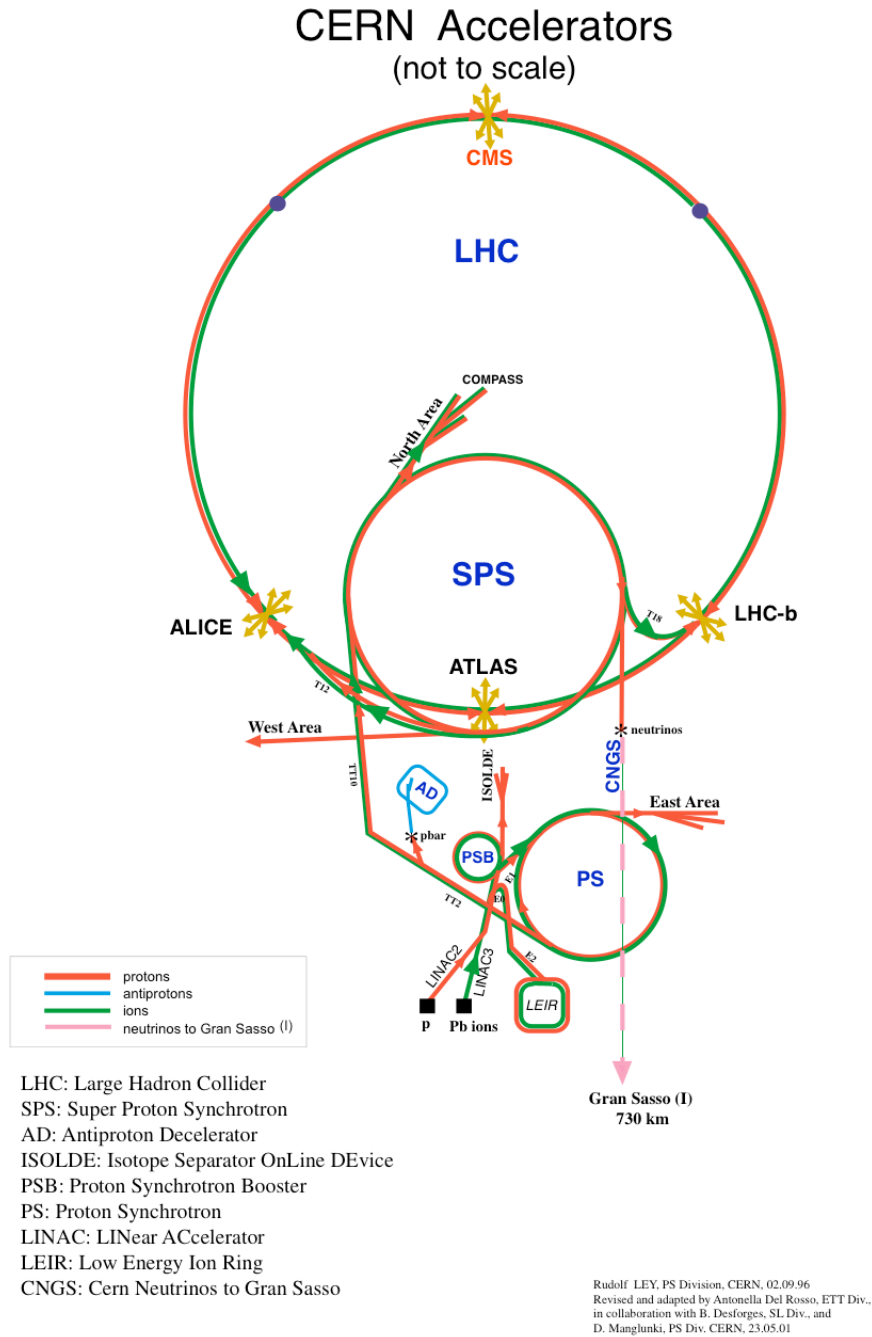


Figure 3.1: Schematic view of the accelerator complex of CERN. This figure has been taken from [45].

as an injector to the LHC where the protons reach up to 7 TeV. 1232 superconducting dipole magnets keep the proton ring inside the ring. They provide a magnetic field up to 8.3 T and are cooled down to 1.9 K by liquid helium. Focusing of the beam in transverse direction is achieved by 392 quadrupole magnets.

Lead ions are provided by an electron cyclotron resonance source, bunching and further acceleration is performed by a radio frequency quadrupole. The ions are then selected in the charge state Pb^{27+} and further accelerated in the linear accelerator LINAC3 to a kinetic energy of 4.2 MeV/nucleon. A carbon foil strips the ion charge with the charge state Pb^{54+} being selected in a filter line. They are further accelerated in the Low Energy Ion Ring (LEIR) to an energy of 72 MeV/nucleon. After transfer to the PS they are accelerated to 5.9 GeV/nucleon and sent to the SPS. In between they are fully stripped to Pb^{82+} . The SPS accelerates the fully stripped ions to 177 GeV/nucleon, before injecting them into the LHC where the lead ions reach a maximum energy of 2.76 TeV/nucleon.

The two independent particle beams orbit inside the LHC storage ring clockwise and counterclockwise, respectively. The two beams cross each other at four interaction points which are each equipped with one of the main experiments, as indicated in Fig. 3.2.

3.1.2 LHC Experiments

Three experiments (ATLAS, CMS, LHCb) were designed for proton-proton collisions. ALICE is the only dedicated experiment to investigate heavy ion collisions.

ATLAS: A Toroidal LHC Apparatus (ATLAS) is designed to give a decisive answer on the long-time postulated existence of the standard model Higgs-Boson and experimentally probe theories beyond the standard model, i.e. the search for supersymmetric particles and extra dimensions.

CMS: The Compact Muon Solenoid (CMS) is, complementary to ATLAS, the other detector at LHC aimed to investigate Higgs-Boson, supersymmetric particles and extra dimensions.

LHCb: The LHC Beauty (LHCb) experiment studies CP violation in B-meson systems. CP violation might be able to explain the asymmetry between matter and antimatter in our universe.

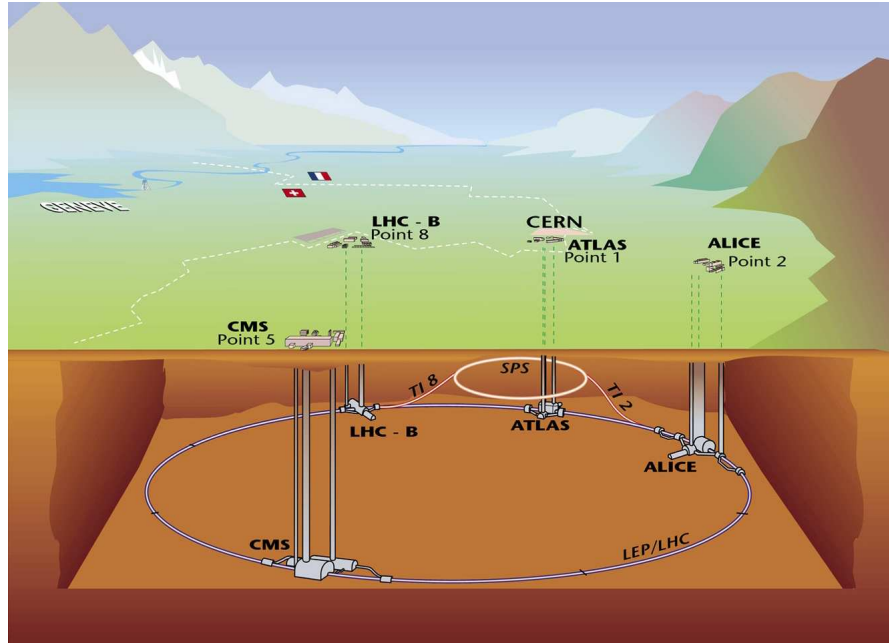


Figure 3.2: Schematic view of the Large Hadron Collider and the four major experiments ALICE, ATLAS, LHCb and CMS. This figure has been taken from [45].

ALICE: A Large Ion Collider Experiment (ALICE) is the dedicated heavy ion experiment at the LHC to identify and characterize the quark gluon plasma created in high-energy collisions of Pb-Pb nuclei.

3.1.3 LHC in Operation

The LHC provided first p-p collisions at injection energy in November 2009. In December, a collision energy of $\sqrt{s}=2.36$ TeV was achieved, exceeding the so far highest collision energy of the Tevatron of $\sqrt{s}=1.96$ TeV. A long run in 2010 with p-p collisions at $\sqrt{s}=7$ TeV followed. In November 2010, first Pb-Pb collisions were delivered. An overview of the LHC operation is given in Table 3.1.

In 2011, the proton-proton collisions have reached a peak luminosity $\sim 4 \cdot 10^{33} \text{ cm}^{-2} \text{ s}^{-1}$. The integrated luminosity versus time in the year 2010 is shown in Fig. 3.3. LHC continues running p-p collision in the years of 2011 and 2012, with one month of Pb-Pb running at the end of each year. The p-Pb collision was started in February 2013.

Date	colliding system	$\sqrt{s}(\sqrt{s_{\text{NN}}})$ (TeV)
23-Nov-2009	p-p	0.9
Dec-2009	p-p	2.36
Mar-2010	p-p	7.0
Nov-2010	Pb-Pb	2.76
2011	p-p	7.0
2011	p-p	2.76
Nov-2011	Pb-Pb	2.76
2012	p-p	8.0
2013	p-Pb	5.02
2013/2014	machine consolidation and training	
2014+	p-p	14.0
	Pb-Pb	5.5

Table 3.1: LHC schedule of operation with p-p and Pb-Pb collisions.

First Pb-Pb collisions at 1.38 TeV per beam were provided on November 7th, the Pb-Pb run ended on December 6th. The integrated luminosity collected is $\sim 150 \mu\text{b}^{-1}$.

3.2 The ALICE Detector System at the LHC

A Large Ion Collider Experiment (ALICE) is designed to identify and characterize the Quark Gluon Plasma (QGP) created in the heavy ion collisions. It is capable of determining the identity and precise trajectory of more than ten thousand charged particles over a large momentum range from 100 MeV/ c to 100 GeV/ c in transverse momentum.

The ALICE detector system is shown in Fig. 3.4, and the pseudo rapidity coverage of the ALICE sub-detectors is shown in Fig. 3.5. Topologically, the sub-detectors are placed in two groups: one is in the mid-rapidity region, and the other is in the forward-rapidity region.

The ALICE sub-detectors in the central barrel covers the mid-rapidity region approximately of $\sim -1 < \eta < 1$, and is surrounded by the L3-magnet. The L3-magnet produces a homogeneous magnetic field of up to 0.5 T parallel to the beam axis. This magnetic field provides momentum dispersion for charged particles in the plane transverse to the beam axis. Inside the L3-magnet in the central barrel, a list of sub-detectors, among which those related to this thesis are briefly presented in the following sections, are arranged in cylindrical shells around the interaction point [46]. From the inner most to the outer, those sub-detectors are: Inner Tracking

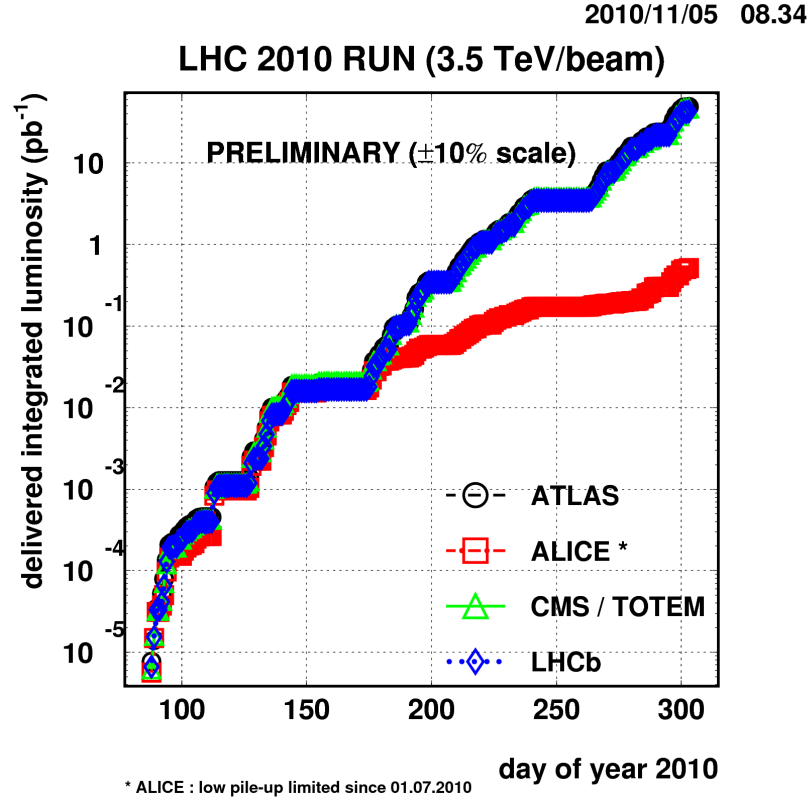


Figure 3.3: Integrated LHC luminosity in 2010. In the later runs, ALICE was applying horizontal separation between crossing bunches at the ALICE collision point (P2), not to exceed an instantaneous luminosity of $2 \cdot 10^{29} \text{ cm}^{-2} \text{ s}^{-1}$ and a collision probability per bunch-bunch crossing of less than 5%. This figure has been taken from [45].

System (ITS), Time Projection Chamber (TPC), Transition Radiation Detector (TRD), Time Of Flight detector (TOF), High-Momentum Particle Identification Detector (HMPID), PHOTon Spectrometer (PHOS), Electro Magnetic Calorimeter (EMCal), ALICE COsmic Ray DETector (ARCODE).

In addition to those in the central barrel, other sub-detectors covering the high pseudo rapidity region complete the ALICE measurement in a larger acceptance coverage. Muon Spectrometer performs the muon detection in the region of $-4.0 < \eta < -2.5$. The Forward Multiplicity Detector (FMD) is placed in the rapidity range $-3.4 < \eta < -1.7$ and $1.7 < \eta < 5.0$. The Photon Multiplicity Detector (PMD) covers the region of $2.3 < \eta < 3.7$. There is other detectors in the forward rapidity region, namely Zero Degree Calorimeter (ZDC), T0 and V0.

3.2. The ALICE Detector System at the LHC

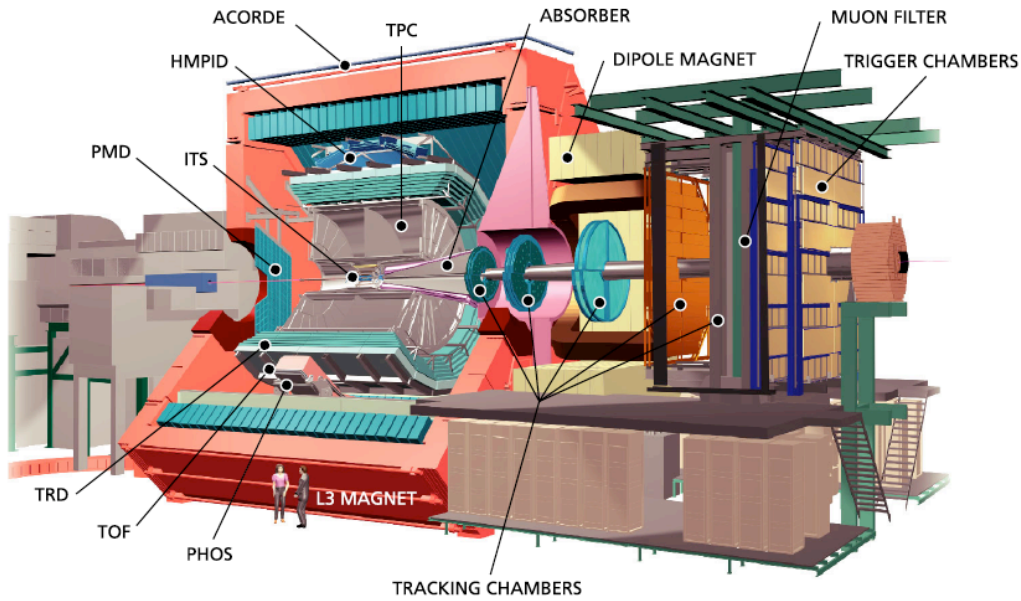


Figure 3.4: Schematic overview of the ALICE detector. This figure has been taken from [47].

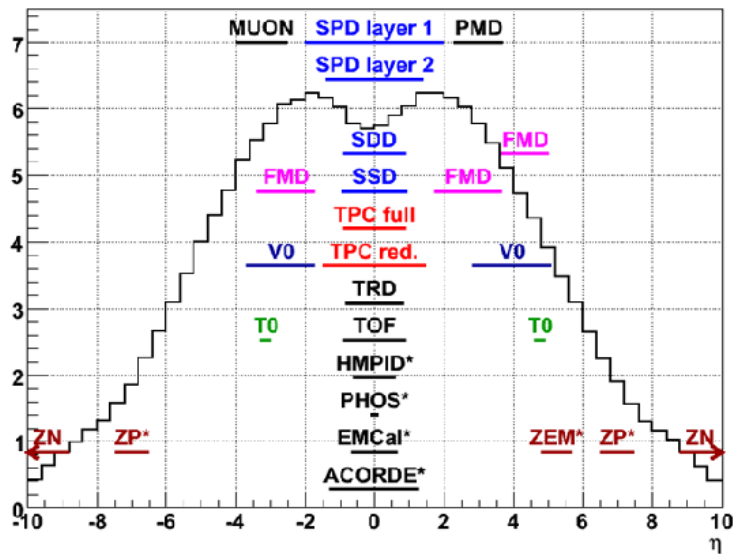


Figure 3.5: Pseudo-rapidity coverage of the ALICE detectors [48].

The ALICE detector has the following advantages in comparison with other experiments:

- ALICE is build with the hadron collision system with the highest center

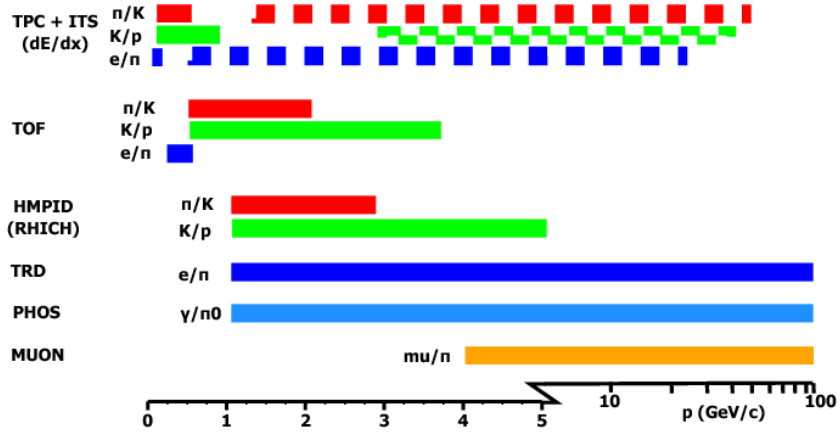


Figure 3.6: Particle identification capabilities of the ALICE detectors as a function of particle transverse momentum [48].

of mass system energy men have ever made;

- ALICE has the world largest Time Projection Chamber (TPC) with full azimuthal coverage, which provides charged particle reconstruction in high multiplicity heavy ion collisions;
- ALICE has full azimuthal coverage providing correlation studies;
- The Inner Tracking System (ITS) of ALICE detector measures as close as down to 4cm to the beam axis, which enables excellent vertex resolution and secondary particle identification;
- ALICE is able to identify particles in large transverse momentum range with various technologies. As shown in Fig. 3.6, the ALICE detectors are able to perform full particle identification in the transverse momentum range from 0.1 GeV/c to 50 GeV/c at mid-rapidity.

3.2.1 Inner Tracking System

Detector Layout

The Inner Tracking System (ITS) consists of six cylindrical layers of three different module types: two layers of Silicon Pixel Detectors (SPD), two layers of Silicon Drift Detectors (SDD) and two layers of double-sided Silicon micro-Strip Detectors (SSD), respectively from the inner layer to the outer layer. Those six layers are located at radii $r = 4, 7, 15, 24, 39$ and 44 cm [47].

The first layer of the SPD, located at only 4cm from the beam axis, covers almost four units of pseudo-rapidity to provide a continuous coverage in η for

the measurement of charged particle multiplicities, together with the forward multiplicity detectors. The two layers of SPD and the two layers of SDD are made of truly bi-dimensional devices, owing to the high particle density expected and the necessity to achieve good impact parameter resolution. The two layers of SPD have good spatial precision of $12 \mu\text{m}$ in the $r\phi$ -plane, while the two layers of SDD have good spatial precision of $28 \mu\text{m}$ in z -direction. The two outer layers are made of double-sided silicon micro-strip detectors and have $20 \mu\text{m}$ spatial precision in the $r\phi$ -plane. The precise spatial measurement in ITS allows for the extrapolation of a track back to the primary vertex of the collision with an impact parameter resolution better than $100 \mu\text{m}$. The main parameters of the constituent sub-detectors are given in Table. 3.2.

	Pixel	Drift	Strip
Spatial precision $r\phi(\mu\text{m})$	12	38	20
Spatial precision $z(\mu\text{m})$	100	28	830
Two track resolution $r\phi(\mu\text{m})$	100	200	300
Two track resolution $z(\mu\text{m})$	850	600	2400
Cell size (μm^2)	50×425	150×300	95×40000
Active area per module (mm^2)	12.8×69.6	72.5×75.3	73×40
Total number of modules	240	260	1698
Total number of cells (M)	9.84	23	2.6
Average occupancy (inner layer)(%)	2.1	2.5	4
Average occupancy (outer layer)(%)	0.6	1.0	3.3

Table 3.2: Parameters of the various silicon detector types of ITS. A module represents a single sensor element [47].

Detector Performance

The Inner Tracking System provides a precise primary vertex reconstruction. Furthermore, with the geometry information provided by ITS in the particle tracking, secondary vertices from weakly decaying particles such as hyperons and open heavy-flavored hadrons, e.g. D and B mesons, are also well reconstructed and can be separated from the primary vertex. The impact parameter of a track, which is the Distance of Closest Approach (DCA) of the track when extrapolated back to the primary vertex, is a signature of the secondary decay vertex. The resolution of the impact parameter in the transverse plane is shown in Fig. 3.7 as a function of transverse momentum. The primary vertex is calculated from all tracks but without the track under

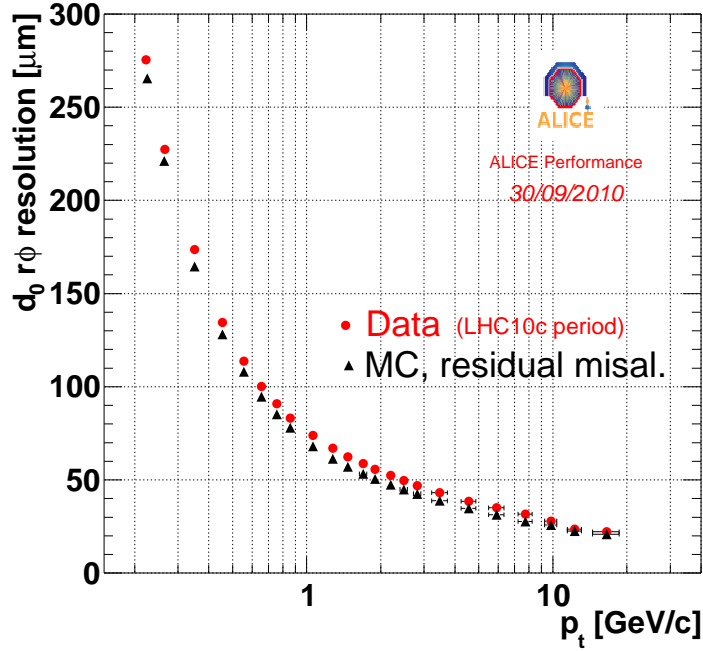


Figure 3.7: Transverse impact parameter resolution from p-p collisions. The impact parameter is the closest distance from the reconstructed collision vertex to an extrapolated particle trajectory. The plot is showing the resolution of its projection on the transverse plane, both in data and simulation.

investigation, and a constraint on primary tracks being within the beam cross section region is applied. The impact parameter resolution at 1 GeV/c is better than 80 μm , which is in the order of the D meson decay length ($\sim 100\mu\text{m}$).

3.2.2 Time Projection Chamber

Detector Layout

The Time Projection Chamber (TPC) is the main tracking detector in the central barrel of ALICE. The TPC provides charged particle momentum measurement and primary vertex determination with precise momentum resolution at large tracking efficiency of better than 90% and two-track separation in the p_T region of up to several 10 GeV/c. The TPC also provides track-by-track event reconstruction for the high-multiplicity Pb-Pb collisions at the LHC energy. In the Pb-Pb collisions at $\sqrt{s_{NN}} = 2.76\text{TeV}$ in 2010, it measures events with charged primary particle multiplicity density

of $dN_{ch}/d\eta = 1584 \pm 4(stat.) \pm 76(syst.)$ [49].

The TPC is cylindrical in shape with an inner radius of 80 cm, an outer radius of 250 cm and a overall length of 5 m, covering full azimuth and the pseudo-rapidity range of $|\eta| < 0.9$. The total material budget is kept at the level of 3% in radiation length to ensure minimal multiple scattering and secondary particle production. It consists of an 88 m³ cylindrical field cage, which is divided by a central membrane into two drift regions. The central membrane is a high voltage central electrode which defines a uniform electrostatic field. The whole drift volume in the cage is filled with a gas mixture of (85%Ne/10%CO₂/5%N₂). This drift gas requires a high drift field (400V/cm) to secure an acceptable maximum drift time of $\sim 88 \mu\text{s}$.

Charged particles traversing the active TPC volume ionize the gas along their trajectory, liberating electrons that drift towards the end plate of the chamber, where the signal amplification is provided through the avalanche effect (gas gain of 2×10^4) in the vicinity of the anode wires. Moving from the anode wire towards the surrounding electrodes, the positive ions created in the avalanche induce a negative signal on the pad plane, which is further processed by the front-end-electronics. Three-dimensional space points are reconstructed from the measured drift time (z -direction) and position on the cathode pads (x, y -direction) of the induced signal. In total, the TPC provides up to 160 space points for each particle trajectory.

Detector Performance

The momentum resolution of the TPC stand-alone tracking was measured from cosmic rays passing vertically through the TPC. The momentum resolution is estimated to be better than 2% for tracks with momentum smaller than 2 GeV/c and 7% at 10 GeV/c, as shown in Fig. 3.8. The momentum resolution for low momentum tracks is limited by multiple scattering with detector material, and at high momentum by the spatial resolution of the TPC.

The TPC provides identification of charged particles by correlating the measured specific energy deposit dE/dx and the reconstructed momentum. In general, the energy loss of a particle traveling through matter is mainly due to ionization. The energy loss is described by the Bethe-Bloch equation [7], described as following:

$$-\langle \frac{dE}{dx} \rangle = K z^2 \frac{Z}{A} \frac{1}{\beta^2} \left[\frac{1}{2} \ln \frac{2m_e c^2 \beta^2 \gamma^2 T_{\max}}{I^2} - \beta^2 - \frac{\delta(\beta\gamma)}{2} \right], \quad (3.1)$$

where $K = 4\pi r_e^2 m_e c^2 N_A = 0.30707 \text{ MeV cm}^2/\text{mol}$, Z, A are the atomic number and atomic weight of the target, I is the average ionization potential,

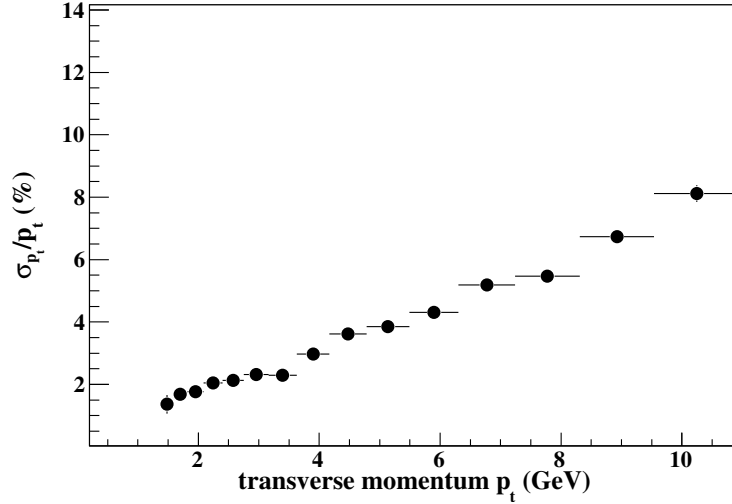


Figure 3.8: TPC transverse momentum resolution measured with events from cosmic rays. This figure has been taken from [50].

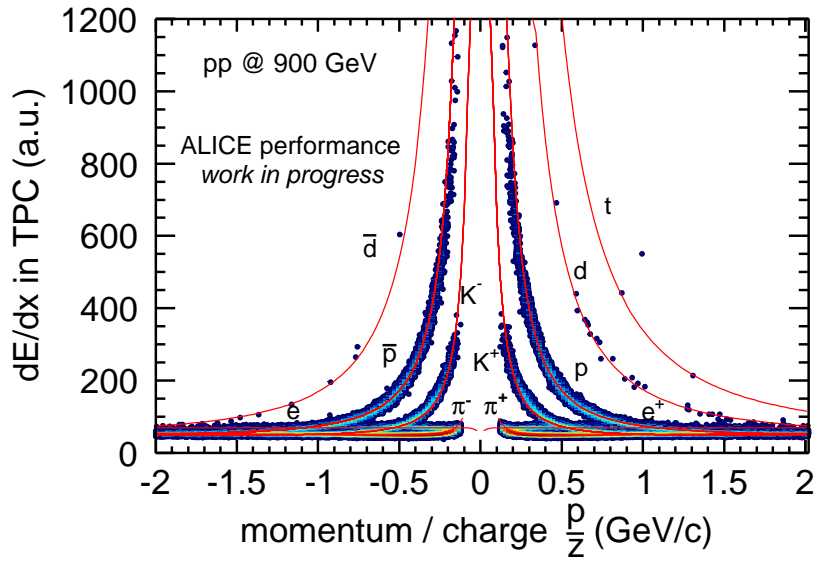


Figure 3.9: TPC dE/dx vs momentum/charge in p-p collisions at $\sqrt{s} = 900$ GeV.

T_{max} is the maximum energy transfer to a free electron in a single collision, and $\delta(\beta\gamma)$ is the correction of density effect. The energy loss is related to both

the projectile and the target. It is proportional to the electron density of the target matter, and proportional to the square of the projectile charge. More importantly, the energy loss depends on the projectile velocity, described in the equation as $\beta\gamma$. The Bethe-Bloch equation is effective from $\beta\gamma \approx 0.1$, which is comparable with "velocity" of the atomic electron, to $\beta\gamma \approx 1000$, at which velocity the radiation effects become significant. A minimum ionization corresponds a projectile at a velocity of around $\beta\gamma \approx 3$ to 4. The energy loss reaches a Fermi Plateau, when $\beta\gamma$ of the particle is larger than 100. The onset and the height of the Fermi Plateau are due to the density correction canceling the relativistic effect. The equation in terms of particle momentum varies only depending on its mass, which gives an identification of the particle species.

The measured TPC dE/dx spectrum in p-p collisions is displayed in Fig. 3.9. The energy loss statistical distribution, which is also referred as straggling function is approximately Gaussian, when the target is thick. But for the thin slice used in the ionization sampling in TPC, it follows a Landau distribution with a tail on its higher energy side. To deal with this effect, a truncated mean is applied to obtain the dE/dx . The energy loss resolution is 5% at the Fermi Plateau and is close to the design value. As a demonstration of the functionality of particle identification with TPC, the band shaped clusters of each particle species are separated well from each other. In ALICE TPC, the energy loss is parameterized with a form proposed by ALEPH [51], instead of Bethe-Bloch equation. The parameterized function is:

$$-\left\langle \frac{dE}{dx} \right\rangle(\beta\gamma) = \frac{P_1}{\beta^{P_4}} \left(P_2 - \beta^{P_4} - \ln \left(P_3 + \frac{1}{(\beta\gamma)^{P_5}} \right) \right), \quad (3.2)$$

which nicely fits the distribution. and

3.2.3 Time of Flight Detector

Detector Layout

Low

transverse momentum hadron identification is achieved via measurements of energy loss in the silicon layers and in the TPC gas. The Time of Flight detector (TOF) extends particle identification to larger momentum. Based on 1638 double-stack Multi-gap Resistive Plate Chambers (MRPC) with an intrinsic time resolution of about 60 ps, the TOF barrel covers a surface larger than 160 m² at a radius of about 3.7 m. It was optimized for the identification of hadrons with a transverse momentum below 2 GeV/c. The separation of pions and kaons is better than 3σ to keep the contamination below a 10% level in presence of a huge bulk of hadrons at low momentum.

In the ALICE MRPC, each resistive electrode is spaced one from the other with equally sized spacers creating a series of ten gas gaps, each $250 \mu\text{m}$ thin. Electrodes are connected to the outer surfaces of the stack of the resistive plates reading out all gas gaps in parallel while all the internal plates are left electrically floating. The flow of positive ions and electrons generated in the avalanche processes maintain the correct voltage between the intermediate plates. Pickup pads (96 per strip), with an area of $3.5 \times 2.5\text{cm}^2$ each, are arranged in two-row arrays.

Detector Performance

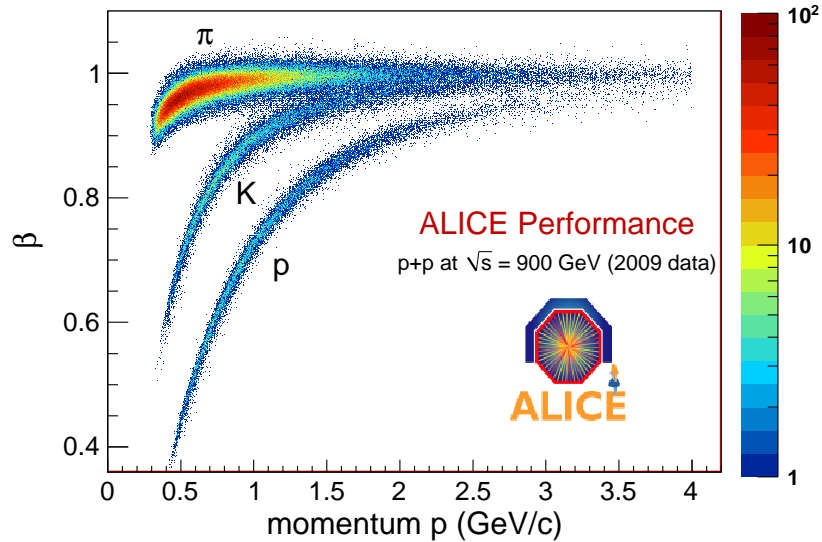


Figure 3.10: Relativistic particle velocity as function of momentum measured with TOF in p-p collision at $\sqrt{s} = 900 \text{ GeV}$. The dependence on particle mass is visible for the different particle species.

As shown in Fig. 3.10, TOF itself provides particle identification for kaons and pions up to $1.5 \text{ GeV}/c$. The measurement is from proton-proton collisions at $\sqrt{s} = 900 \text{ GeV}$. The time resolution achieved in the flight time measurement of a single track is $\approx 160 \text{ ps}$. The intrinsic timing resolution of the TOF detector was estimated to be $\approx 80 \text{ ps}$, with another contribution to the overall timing resolution from the V0 detectors, which provided the starting time of the time-of-flight measurement.

3.2.4 VZERO Detector

Detector Layout

The VZERO (V0) detector consists of two arrays of scintillator (V0A and V0C) on opposite sides of the interaction point. V0A is located 340 cm away from the interaction point in beam direction, covering the pseudorapidity range $2.8 < \eta < 5.1$. V0C is located 90cm from the interaction point, covering $-3.7 < \eta < -1.7$.

Detector Performance

The V0 detector provides both timing and amplitude information. It provides minimum bias trigger information for the central barrel detectors, and serves as a luminosity monitor in proton-proton collisions. In Pb-Pb collisions, it is used to obtain the centrality of the event and also as a centrality indicator providing two different centrality triggers.

The timing resolution of V0 is better than 1 ns. By measuring the time interval between a V0A and V0C signal, beam-beam collisions are identified from background beam-halo or beam-gas events.

3.3 Data Collection

The data used in this analysis are collected from the p-p collisions at $\sqrt{s}=7$ TeV in year 2010. The data consist 314 million minimum-bias (MB) collision events. In order to achieve the integrated luminosity, we need to calculate the trigger cross section first.

3.3.1 Minimum Bias Trigger

In the certain period, when the data used in this analysis are taken, the proton-proton collisions were triggered with minimum bias for the central barrel detectors. The minimum bias (MB) trigger is defined as the logical OR between the requirement of at least one fired readout chip in the SPD, and at least a signal in one of the two VZERO detectors. It is estimated by Monte Carlo simulation [52] that the MB trigger is about $\sim 87\%$ sensitive to the proton proton inelastic cross section.

The inelastic cross section of p-p collisions is obtained from the Van der Meer scan [53]. The Van der Meer scan is performed by displacing the two beams against each other in horizontal or vertical direction. The luminosity reduction W is a function of displacement d :

$$W(d) = \mathcal{L}(d)/\mathcal{L}_0. \quad (3.3)$$

This luminosity dependence reflects the beam profile in transverse directions. Given a Gaussian beam profile, the luminosity is described as:

$$\mathcal{L}_0 = \frac{N_1 N_2 f N_b}{4\pi\sigma_x\sigma_y}, \quad (3.4)$$

where N_1, N_2 are the beam intensities, f is the revolution frequency, N_b is the bunch number and σ_x, σ_y are the beam widths. By measuring the luminosity reduction $W(d)$, we can determine the beam profile σ_x, σ_y , and further the beam intensity N_1, N_2 , which leads to the determination of the luminosity \mathcal{L}_0 .

The $\sigma_{pp}^{inelastic} = 71.4 \pm 0.7(stat.) \pm 7.1(syst.)$ mb is measured. The MB trigger cross section is then determined as $\sigma_{trigger} = 0.87 \cdot \sigma_{pp}^{inelastic} = 62.3$ mb.

3.3.2 LHC Luminosity

During the data taking, the relative LHC luminosity at the ALICE experiment is measured by using the event rate of p-p collisions R_{pp} . One can simply obtain it from:

$$R_{pp} = \sigma_{trigger} \cdot \mathcal{L}, \quad (3.5)$$

where $\sigma_{trigger}$ is the cross section of the event trigger, and L is the luminosity of the beam. For a period of running, if we consider the triggered cross section to be constant, we get the integrated luminosity:

$$N_{pp} = \sigma_{trigger} \cdot \mathcal{L}_{int}, \quad (3.6)$$

where \mathcal{L}_{int} is determined by the number of p-p collision events N_{pp} and the triggered cross section $\sigma_{trigger}$. For data collection used in this analysis, the corresponding integrated luminosity is 5 nb^{-1} .

3.4 Offline Analysis

The ALICE Offline Framework (AliRoot) is the common framework for the analysis of ALICE data built on the basis of the ROOT [54] system. ROOT is an object-oriented software package developed by CERN providing an environment for high energy physics data analysis. AliRoot makes full use of all the ROOT potential, entirely written in C++, with some external

programs (hidden to the users) in FORTRAN. The framework itself, together with ROOT, is in continuous development.

The objective of the AliRoot offline framework is to reconstruct and analyse the physics data stemming from simulated or real collisions. AliRoot is also used to perform simulations for the study of the detector response and the evaluation of the physics performance. Figure 3.11 shows the schematic of the AliRoot work flow. In general, there are three different steps of functionality: (1) simulation, (2) reconstruction and (3) analysis.

The simulation contains event generator and transport package, where primary interaction and detector response are simulated. The reconstruction takes the detector signal or simulated signal as input, and converts the information into reconstructed vertices and tracks as well as identified particle types. The analysis framework contains many topics of physics, and the one used for charmed hadron reconstruction is described in Chapter 4.

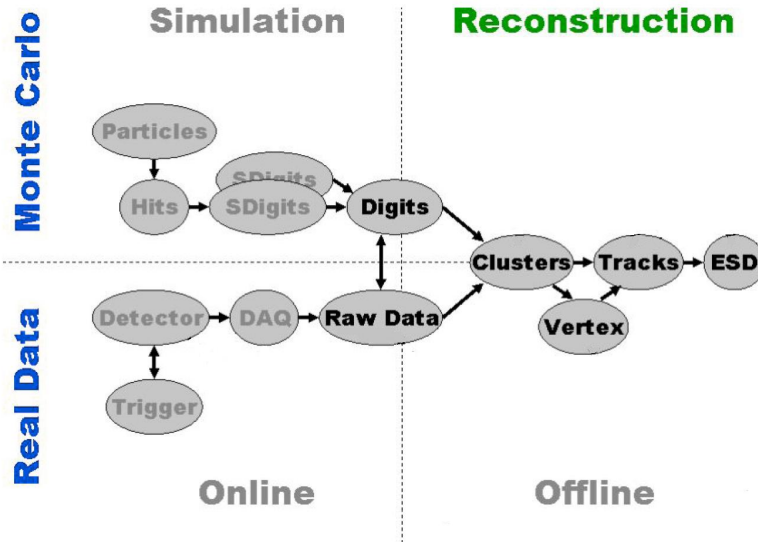


Figure 3.11: Schematic work flow of the AliRoot offline framework. This figure has been taken from [55].

3.4.1 Monte Carlo Simulations

The $p+p$ interactions are simulated via the event generator package PYTHIA 6.4 [29]. It is based on a combination of analytic results and various QCD models. Other event generators are also available in AliRoot for rare signal generations, e.g. HIJING [56] is used as a generator for jets in heavy ion collisions.

After their generation, particles in the final state are fed into the transport program. These particles are transported through the simulated material of each sub-detector, and the interaction with the material is also simulated. The material and geometry of the detectors are simulated with GEANT3 [57]. At each interaction point between the particle and the material, the energy deposition and location of the interaction are with a data type called *hits*.

The simulation of the detector response generates the *summable digits (sdigits)* from the energy deposition. The *sdigits* are the detector analog responses, before the analog-digital conversion. The front-end electronics and the data acquisition system are simulated. The *sdigits* are then converted to the digitized *digits*. The truncation of the signal is also included in the digitization. The output *digits* closely resemble the *raw data* collected from the detector. These two formats are interchangeable.

3.4.2 Reconstruction

The reconstruction is the process of converting the raw data/digits information into that used in the physics analysis. The reconstruction process in AliRoot involves three steps: clusterization, tracking (including vertexing), and event reconstruction.

Clusterization is operated by the local reconstruction within each sub-detector separately. In this step clusterization is done first to convert adjacent *digits* into *clusters*. A *clusters* is acquired by combining the digits of adjacent pads that were presumably generated by the same particle that interacted with the detector. Weighted center position and sum of the signal (proportional to the total energy deposition) is saved in a cluster.

The tracking procedure assigns space points to *tracks* and reconstructs their kinematics. It is the main part of the reconstruction procedure and also one of the most challenging tasks of the experiment. It involves the reconstruction of a particle trajectory and the primary collision *vertex* as well as the secondary vertices from particle decay (e.g. $D^0 \rightarrow K^- \pi^+$, $\Lambda \rightarrow p \pi^-$). The Kalman filtering [60] approach is used in the tracking in the mid-rapidity region.

The general tracking strategy in the mid-rapidity sub-detectors consists of the following three steps. First, the tracking starts from the outer radius of the TPC, where the track density is minimal. The track candidates 'seeds' are found and the tracking algorithm proceeds to smaller TPC radii. This is because a seed has only a small number of clusters and the precision of its parameters is not good enough to extrapolate it outwards to other sub-detectors. When all the seeds are extrapolated to the inner radius of the TPC, the TPC tracks are prolonged as close as possible to the primary vertex. On

the way to the primary vertex, the tracks are assigned additional ITS clusters, which improves the track parameters. After all the TPC tracks are assigned to their ITS clusters, a special ITS stand-alone tracking procedure is applied to the still unassigned ITS clusters, finding the low p_T tracks.

In the second step, the tracking is restarted from the primary vertex back to the out layer of the ITS and then to the outer wall of the TPC. At this point the precision of the estimated track parameters is sufficient to extrapolate the tracks to the outer TRD, TOF, HMPID and PHOS sub-detectors. The momentum resolution is improved with more clusters assigned.

In the final step of the tracking, all tracks are refitted backwards to the primary vertex or to the most inner radius. In case of secondary tracks, they are not extrapolated with a constraint to the primary vertex, and the track parameters are good enough in the refit step.

The *vertex* position in beam direction is reconstructed by the SPD, the most inner two layers of the ITS. The correlation of the two points z_1, z_2 in the two layers is used for the reconstruction of vertex in beam axis. The reconstruction of the vertex position in the $r - \phi$ plane is acquired using the reconstructed tracks. A more precise primary vertex reconstruction with exclusion of secondary tracks is applied for D and B hadron reconstructions.

All the information acquired from the reconstruction is classified in each event, and store in the *Event Summary Data (ESD)*. The ESD is further called by a specific analysis.

Chapter 4

D^{*+} Reconstruction

In this analysis, D^{*+} mesons are kinematically fully reconstructed via the decay channels $D^{*+} \rightarrow D^0 + \pi_s^+$ and $D^0 \rightarrow K^-\pi^+$. Track quality selections and decay topology selections are applied and optimized for the D^{*+} significance. To reduce the combinatorial background, pion and kaon particles, as the daughters of D^0 , are identified using the measured signal of energy loss and time-of-flight. The raw yields of the D^{*+} signal are extracted, in several p_T intervals, from the peak in the invariant mass plot. In this chapter, the terms of D^{*+} and D^0 include their charge conjugates D^{*-} and \bar{D}^0 , if not specified otherwise.

4.1 D^{*+} Decay Channel

There are two consecutive cascade decay channels involved in the D^{*+} reconstruction. One decay product from the D^{*+} decay is the D^0 meson, which decays further into a K^- and a π^+ . The other decay product is a π^+ , which has a low momentum due to the small mass difference between D^{*+} and D^0 . In the D^{*+} reconstruction analysis, the low momentum pion is called soft pion, and is symbolized as π_s^+ or π_{soft}^+ . Thus, one first has to reconstruct the D^0 meson via the $D^0 \rightarrow K^-\pi^+$ channel. Then the reconstructed D^0 and another pion in the same collision event are paired, and the invariant mass of the D^{*+} meson candidate is calculated.

4.1.1 $D^0 \rightarrow K^-\pi^+$ Decay Channel

A D^0 meson consists of two valence quarks, a light \bar{u} quark and a heavy c quark. Its rest mass is $m_{D^0} = (1864.86 \pm 0.13) \text{ MeV}/c^2$ [7]. Since the D^0

meson is the lightest charmed hadron, it decays only through weak processes, e.g. transforming the charm quark into an s quark with a mean decay length of $c\tau = 122.9 \pm 0.5 \mu\text{m}$ [7]. The branching ratio to the decay channel $D^0 \rightarrow K^-\pi^+$ is $(3.88 \pm 0.05)\%$ [7]. The two daughter particles, K^- and π^+ , are of opposite charge. When the two daughters of the $D^0 \rightarrow K^-\pi^+$ decay are in the central rapidity region of the ALICE detector, they will be detected by the tracking detectors ITS and TPC. Due to the short decay length of the D^0 meson, the daughter particles are created before they reach any of the detectors. Thus the decay vertex, i.e. the starting point of the daughter particle trajectories, is not directly measured by the detector. It is reconstructed by extrapolating the measured trajectories in the direction towards the primary collision vertex and measuring the crossing point of the two daughter trajectories.

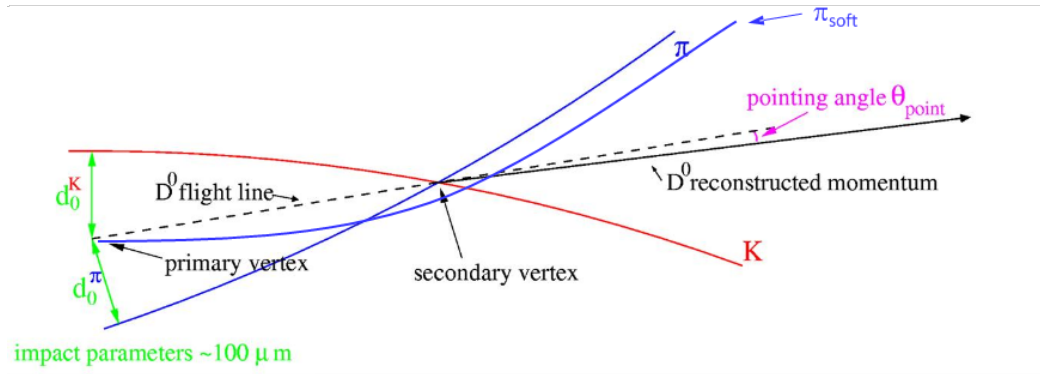


Figure 4.1: Schematic view of the $D^{*+} \rightarrow D^0(K^-\pi^+)\pi^+$ decay [8].

Figure 4.1 demonstrates a typical $D^{*+} \rightarrow D^0\pi^+$ and $D^0 \rightarrow K^-\pi^+$ decay. The two curves represent the two extrapolated trajectories of K^- and π^+ . The two curves are displaced from the primary vertex. The variables of the decay mechanism, as shown in the figure, are defined in the following:

The **primary vertex** is the proton-proton collision vertex in 3-dimensional space. It is also the production point of the prompt D^{*+} and D^0 particle. Due to the short life time of the D^{*+} , it is also approximately the production point of the D^0 which decays from a D^{*+} meson.

The **secondary vertex** is the point in 3-dimensional space where the D^0 particle decays. $(3.88 \pm 0.05)\%$ of the D^0 mesons, as listed in Tab. 4.1, decay through the $D^0 \rightarrow K^-\pi^+$ channel.

The **daughter particles** are the outgoing particles from the decay. In the case of the $D^0 \rightarrow K^-\pi^+$ decay, the K^- and π^+ are the daughter particles. In contrast to the neutral mother particle, the two daughter particles have

opposite charges. With a magnetic field in parallel to the beam direction, the flight trajectories of the daughters are curved in the transverse plane, with opposite orbiting directions. In Fig. 4.1, the two curves drawn in different color codes represent the prolonged trajectories of the two daughter particles. The daughter particles originate at the secondary vertex and move away from the primary vertex.

The D^0 **flight line** is the straight line connecting the primary vertex and the secondary vertex. It is the trajectory of the D^0 's motion, which is straight since it is a neutral particle and does not bend in the magnetic field. The dashed line in Fig. 4.1 is the prolonged D^0 flight line for better demonstration.

The **impact parameter** d_0 is the distance of closest approach between the primary vertex and the prolonged daughter particle trajectory, as d_0^K and d_0^π shown in Fig. 4.1 for the impact parameters of K^- and π^+ , respectively. The impact parameter is the distance in 3-dimensional space by definition. But in the analysis, it is calculated as the distance in the projection on the transverse plane. The reason is that the detector resolution in the transverse plane is much better than that in the beam direction, as listed in Tab. 3.2.

The **pointing angle** θ_{point} is defined as the angle between the D^0 flight line and the reconstructed D^0 momentum direction. Ideally, those two lines have identical direction, but in the measurement, they may be different due to the limited detector space resolution and momentum resolution. The pointing angle is used for D^0 candidate selection in the reconstruction.

The **DCA (Distance of Closest Approach)** is the closest distance between the prolonged trajectory of the two daughter particles. It is used for D^0 candidate selection, in order to remove false combination of two tracks which are not stemming from a D^0 decay.

The **decay angle** θ^* is the angle, in the center-of-mass coordinate system of the D^0 , between the D^0 flight line and the flight line of the daughter particles. Due to momentum conservation law, in the rest coordinate system of D^0 , the two daughters are flying back to back, and the decay angle for the two daughters to D^0 are θ^* and $\pi - \theta^*$. In the experiment, we always measure the decay angle by calculating the value $\cos\theta^*$, making it independent on the ordering of the daughter particles. The value $\cos\theta^* = 1$ represents that the daughters move in parallel to the D^0 direction, and $\cos\theta^* = 0$ represents that the daughters move perpendicular to the D^0 flight direction.

4.1.2 $D^{*+} \rightarrow D^0 + \pi_s^+$ Decay Channel

The D^{*+} meson is a vector meson with a heavy c valence quark and a light \bar{d} valence anti-quark. The total orbital momentum is $J = 1\hbar$ with the spins of

D^0 decay mode	Fraction (Γ_i/Γ)	Decay momentum (MeV/c)
$K^-\pi^+$	$(3.88 \pm 0.05)\%$	861
$K^-\pi^+\pi^+\pi^-$	$(8.08 \begin{smallmatrix} + 0.21 \\ - 0.19 \end{smallmatrix})\%$	813
$K^-\pi^+\pi^0$	$(13.9 \pm 0.5)\%$	844

Table 4.1: Main D^0 decay channels. These channels are often used in D^0 reconstructions. These numbers have been taken from [7].

both valence quarks aligned in parallel and no orbital momentum amongst them. The rest mass of the D^{*+} meson is $m_{D^{*+}} = (2010.28 \pm 0.13) \text{ MeV}/c^2$ and differs by only $\Delta m = 145.421 \text{ MeV}/c^2$ from the rest mass of the lighter D^0 meson. Strong decay to the D^0 meson occurs by emitting a charged pion which is close to the phase space boundary resulting in a low momentum of 39 MeV/c of the emitted charged pion in the rest frame of the D^{*+} meson. The branching ratio in the decay channel $D^{*+} \rightarrow D^0 + \pi_s^+$ is $(67.7 \pm 0.5)\%$ [7]. The peculiar kinematics in the decay of the D^{*+} meson leads to a rather long lifetime corresponding a narrow internal width $\Gamma = (96 \pm 22) \text{ keV}/c^2$. Thus, the width of the invariant mass of the reconstructed D^{*+} is solely defined by the experimental momentum resolution. Since the D^{*+} decay is subject to strong interactions, the lifetime is too short for topological reconstruction. Within the experimental resolution, the soft pion is emitted at the primary vertex.

D^{*+} decay mode	Fraction (Γ_i/Γ)	Decay momentum (MeV/c)
$D^0\pi^+$	$(67.7 \pm 0.5)\%$	39
$D^+\pi^0$	$(30.7 \pm 0.5)\%$	38
$D^+\gamma$	$(1.6 \pm 0.4)\%$	136

Table 4.2: D^{*+} decay channels. These numbers have been taken from [7].

4.1.3 The Soft Pion π_s^+

The transverse momentum distribution of the two daughter particles π_s^+ and D^0 from the D^{*+} decay are simulated in p-p collisions. The p_T correlation of the two daughter particles is shown in Fig. 4.2. The small kinematic momentum of the $D^{*+} \rightarrow D^0 + \pi_s^+$ decay leads to the following characteristics:

- The momenta of the two daughter particles π_s^+ and D^0 are mainly acquired from the kinetic energy of the mother particle D^{*+} .

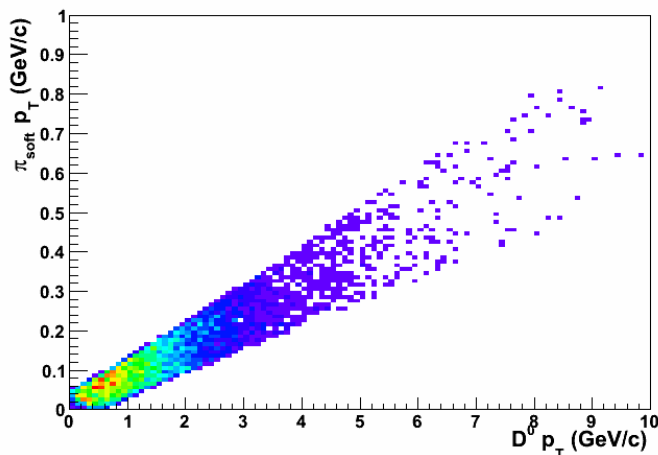


Figure 4.2: Transverse momentum distribution of π_s^+ and D^0 mesons from $D^{*+} \rightarrow D^0 + \pi_s^+$ decays from PYTHIA simulation in p-p collisions at $\sqrt{s} = 7$ TeV.

- The velocities of the two daughters π_s^+ and D^0 are almost the same as the velocity of the mother particle D^{*+} .
- The momenta of the two daughters are correlated. Their momenta are nearly proportional to their rest masses. The p_T of the soft pion is about $\sim 1/13$ of that of the D^0 .
- The direction of the two daughter particles π_s^+ and D^0 are correlated, especially for those with high momenta.

We can see most of π_s^+ are distributed with p_T about ~ 100 MeV/ c , while the D^0 has a typical p_T of ~ 1 GeV/ c . To optimize the acceptance for D^{*+} reconstruction, the soft pion has to be detected at lowest momenta. Presently, when using TPC and ITS together as tracking detectors, the lower momentum cut is $p_T > 100$ MeV/ c . This is limited by the inner radius of TPC, where low momentum particles do not reach. Due to this limitation, most of the D^{*+} particles, which have low transverse momentum soft pion daughters, are not able to be reconstructed. To overcome this, tracking with the ITS detector only is applied.

ITS stand-alone tracking

The general tracking procedure with TPC and ITS combined is started from tracking in TPC and then assign ITS clusters to the track. Aside from that,

the ITS stand-alone tracking uses ITS clusters only. It uses a grouping algorithm to group the clusters from different layers within a search window in the (θ, ϕ) angle. Then a fit is applied on the clusters, including the primary vertex, with a parabola, as shown in Fig. 4.3. This algorithm is described in [61].

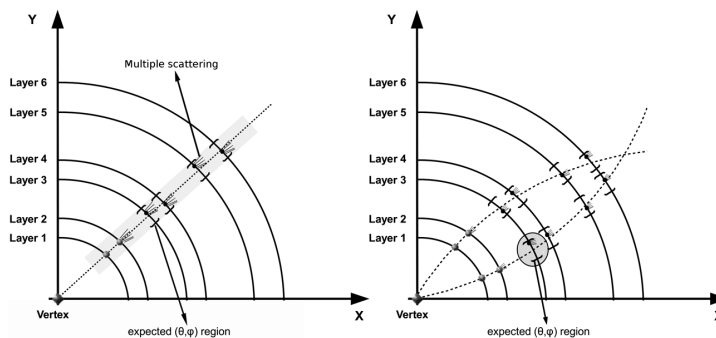


Figure 4.3: Schematic view of stand-alone tracking in the ITS. Left: tracking high p_T particles; right: tracking low p_T particles [62].

By using ITS as a stand-alone tracking algorithm, the momentum cut may be lowered down to 60 MeV/ c , see Fig. 4.4. The inclusive momentum distribution of pions from p-p collisions peaks around 500 MeV/ c and is thus much harder than the soft pion distribution from D^{*+} decay. We do not apply an upper cut on the soft pion transverse momentum, in order to have a high acceptance for D^{*+} reconstruction at large transverse momentum where the soft pion is boosted to higher momentum by the relativistic speed of the mother particle.

4.2 Reconstruction Scheme

4.2.1 Invariant Mass

In the reconstruction procedure, a D^0 candidate is retrieved from the combination of two reconstructed daughter trajectories of opposite charge, which are considered as decay products stemming from the same mother D^0 . The mass, energy and momentum vector, i.e. the 4-vector, is calculated from the reconstructed momentum vector of the two daughter candidate tracks and assuming a K^- or π^+ mass, respectively.

For a particle, in natural units, the mass M is

$$M^2 = E^2 - \|\vec{p}\|^2. \quad (4.1)$$

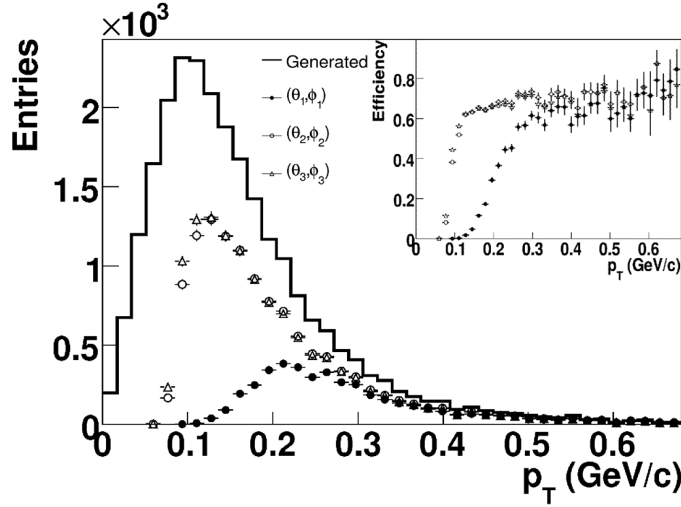


Figure 4.4: p_T distribution of the soft pion from the D^{*+} decay. The three sets of (θ, ϕ) represent the searching window settings in the ITS stand-alone tracking. The (θ_1, ϕ_1) is the conservative setting for Pb-Pb runs, and the other two are for pp runs [62].

In the current case, with one mother of mass M and two daughters, this results in,

$$M = \sqrt{(E_1 + E_2)^2 - \|\vec{p}_1 + \vec{p}_2\|^2}. \quad (4.2)$$

Here, with D^0 as the mother and two daughter particles of total energy E_1 and E_2 , and three momentum \vec{p}_1 and \vec{p}_2 , the invariant mass of the initial state is calculated.

The reconstruction of the D^{*+} requires only one more step, by combining the reconstructed D^0 candidate with a π^+ , and calculated the invariant mass difference Δm , makes a D^{*+} candidate. Likewise, combining a \bar{D}^0 candidate with a π^- makes a D^{*-} candidate.

4.2.2 Δm Distribution

The D^{*+} reconstruction is presented by the difference in invariant mass $\Delta m = m_{D^{*+}} - m_{D^0}$ between both reconstructed D mesons. The mass resolution in Δm is solely defined by the momentum resolution of the soft pion π_s^+ . The D^{*+} signal is then expected as a narrow peak in the Δm distribution close to the phase space boundary and thus on a rather low combinatorial background.

4.2.3 Particle Combination

In p-p collisions at LHC energies, more than 100 charged particle tracks are reconstructed in the central barrel in a single event. The possible combinations of each two tracks are too large a number, and, most importantly, will introduce a large background with false combination compared to the tiny amount of real D^0 found.

Thus, the topological selection is used in the reconstruction scheme as a powerful tool to enhance the signal to background ratio. A $D^0 \rightarrow K^- \pi^+$ decay is a typical two-prong decay from a neutral mother into daughters of opposite charge. The decay vertex is the creation point for both of the two daughter particles, and the vanishing point of the mother particle. Such a decay vertex is called a secondary vertex, which is displaced from the primary vertex of the beam-beam interaction. From the measurement, the tracks from a decay cross at the decay vertex within some deviation due to the finite resolution. By extrapolating the two track trajectories, a virtual crossing point is established and considered the secondary vertex of the D^0 candidate.

The secondary vertex is reconstructed both online and offline. The online vertexer gives fast reconstruction of the particle vertex in the event reconstruction procedure, while reconstructing tracks from the the summable digits. But this could not be applied to the reconstruction of secondary vertices from the decay of charmed meson, which has a typical decay length of $100\mu\text{m}$, which is too close to the primary collision point and outside the detector sensitive area. The offline secondary vertex reconstruction is used in this analysis. There are two alternative algorithms for the offline vertexing, one using the minimization of the the Distance of Closest Approach (DCA) of two daughter tracks, another using the Kalman Filter for vertex reconstruction [63].

In an event, to get all the D^{*+} candidates, a secondary vertexing algorithm contains the following tasks. First, a pre-selection (see Sec. 4.3) is applied for all charged ESD tracks, and grouped in two parts according to the charge sign, positive and negative. Every combination of one positive and one negative track is taken into account. Then a set of topological selections are applied on those D^0 candidates. Those selections are made by applying cuts on the topological objects of the D^0 secondary vertexing, including impact parameter ($d_0^{K,\pi}$), product of impact parameter ($d_0^K \times d_0^\pi$), distance of closest approach (DCA), transverse momentum of the daughter track ($p_{T_{K,\pi}}$), pointing angle ($\cos\theta_{\text{point}}$), and decay angle ($\cos\theta^*$). These selected D^0 candidates are combined with a soft pion candidate, D^0 with a positive pion, and \bar{D}^0 with a negative pion. Further selections on the D^{*+}

are applied afterwards.

4.2.4 Vertexing Algorithm

The secondary decay vertex of the D^0 meson is typically $123 \mu\text{m}$ away from the primary vertex, which is a very short distance. The discrimination of these decay vertices of D^0 meson requires a good reconstruction performance of both the primary and secondary vertices.

Primary Vertex The primary vertex is reconstructed by extrapolating all tracks in the ITS inwards in direction of the beam axis. The tracks are grouped in all possible pair combinations, and the weighted center of the minimum distance of approach of the track pair is considered a primary vertex candidate. The primary vertex is determined by searching for the minimum χ^2 to those candidates in 3-dimensions.

In order to remove tracks that are not from the primary vertex, the χ^2 of primary vertex is re-calculated by removing tracks one by one. A track is removed from the primary vertex calculation, if the contribution to the χ^2 of the track is larger than a threshold. The final primary vertex is acquired, when no such tracks are left, and the χ^2 difference by removing tracks is always smaller than the threshold. This method removes strange decay particles from the primary particle calculation.

Secondary Vertex The secondary vertex of a D meson decay is reconstructed by calculating the minimum distance of approach of the two tracks. The algorithm is the same as the one used in determining primary vertex candidates when reconstructing the primary vertex. The tracks are propagated to the vicinity of the primary vertex. The secondary vertex is determined as a weighted center of the segment of minimum approach of the two prolonged tracks.

The D^0 daughter tracks have typically $\sim 100 \mu\text{m}$ impact parameter to the primary vertex, which is too close to the primary vertex and can not be excluded in primary vertex reconstruction. However, in the determination of the secondary vertices of the D^0 mesons, their daughter tracks should be removed from the primary vertex reconstruction. Especially in p-p collisions, where the multiplicity is relatively low, the primary vertex is spoiled by the secondary tracks. In the analysis of charmed hadron reconstruction via hadronic decay channels, the primary vertex is re-calculated for each secondary candidate, by removing the tracks used for the secondary vertex from the primary vertex reconstruction.

4.3 Track Selection

In the reconstruction of D^{*+} mesons, the first step is the selection of the daughter track candidates. Those daughter track candidates are then combined to reconstructed D^0 and D^{*+} candidates. The track selection involves selections on the track quality, its topology and the track kinematics.

The track selection is made on the daughter particles candidates of D^0 , but not on the soft pion decayed from D^{*+} . Given the poor reconstruction efficiency of the soft pion, the selection criteria of the soft pion candidates is kept as loose as possible.

The signal tracks represent those K, π daughter tracks, which decay from the $D^0 \rightarrow K^- \pi^+$ channel. The background tracks are those not stemming from the $D^0 \rightarrow K^- \pi^+$ channel.

4.3.1 Selection on Track Quality

The quality of a reconstructed particle track is determined by the number of space points assigned to the track. A reconstructed track with good quality has more space points assigned along its trajectory. In the ITS detector, there are 6 layers of detectors. Each layer is able to provide one hit for a track. In the TPC detector, moving charged particles ionize the gas, and the induced signal from the ionized gas is grouped in a so-called cluster. The TPC can measure up to 160 clusters for a track. If a track is measured by more than one sub-detectors, the track quality is much improved by the space point given by those detectors.

Tracks assigned with more measured space points are preferred. As a track with good quality, its probability of being a false track is minimal. It also has good momentum and spatial resolution.

Selection on Track Status Measurement at various distances to the beam can improve the quality of the track. For a reconstructed track at mid-rapidity, four sub-detectors may take part in the tracking procedure. They are ITS, TPC, TRD and TOF. Their presences are tagged as the status of the track.

There are three passes in the global track reconstruction flow of the central barrel. The first pass is track finding and fitting in the inward direction inside the TPC and then to ITS. Tracks are found by connecting the clusters. The next pass is propagating the track back outwards, which reconstructs the track by starting with the ITS via TPC and TRD to TOF. In the last pass, the tracks are refitted inward passing through TRD, TPC and ITS, consecutively. The first pass is aimed for track finding and fitting; the second is to include

all available detector information into the tracking; and the third pass is to extract the track parameters.

For the present analysis, each track is required to have both TPC and ITS contribute in the refit procedure. A selection on tracks reconstructed with TPC in the refit procedure guarantees a good track momentum resolution. Since the TPC has the most measured space points in the tracking, a track reconstructed with TPC will lead to a best fit with the space points to the track.

A track with ITS in the refit procedure has optimal spatial resolution near the collision point. A track is extrapolated from the measured ITS points to the primary vertex. The impact parameter of the tracks from the D^0 decay can be used to distinguish the secondary particles from the primary particles. The ITS measurement also improves the space resolution of the primary vertex, because we are able to exclude the secondary tracks from the primary vertex reconstruction procedure.

Selection on Number of Track Clusters The TPC provides a maximum of 160 clusters of reconstructed space points. The more clusters are assigned to a track, the better spatial and kinematic resolution it has. The selection on the number of TPC clusters of a track is a decisive selection on the quality of the reconstructed track. By selecting tracks with a minimum of 70 TPC clusters, most poorly reconstructed tracks are excluded from the analysis.

The ITS provides clusters at the positions which are close to the collision vertex. These ITS clusters play the most important role in determining the track topology when the track is extrapolated to the primary vertex. Since the innermost measurement is most critical to estimate of the displaced vertex, the applied selection is crucial for reconstruction of a secondary vertex close to the collision point. In the present analysis, tracks are required to have at least one SPD hit.

4.3.2 Selection on Track Kinematics

Selection on Transverse Momentum Tracks with low transverse momentum are strongly bent in the magnetic field. Additionally, they suffer from multiple scattering in the detector material. The extrapolation of a low momentum track to the primary vertex implies large uncertainties.

Most of the particles with low momentum are not from D^0 decays. Decays of resonances (e.g. $\Delta^{++} \rightarrow p\pi^+$) generate low momentum pions. Also, δ -electrons traversing the TPC gas have very low momenta. On the other hand, most daughter particles from the $D^0 \rightarrow K^-\pi^+$ decay channel have momentum above 500 MeV/c. The transverse momentum distribution of

both signal and background tracks are shown in Fig. 4.5. A selection of $p_T > 0.5$ GeV/c is made for a track. This selection rejects a large fraction of background tracks while keeping most of the signal tracks.

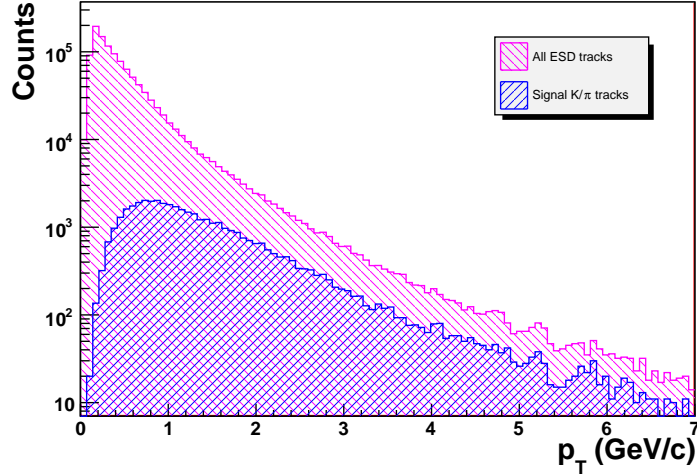


Figure 4.5: Transverse momentum distribution of tracks before selection. Magenta: all tracks from both signal and background; Blue: daughter tracks K, π from D^0 decays. The data are from a minimum bias simulation with PYTHIA.

Selection on Pseudorapidity There is a selection on the pseudorapidity of the tracks. It requires a track to have $|\eta| < 0.8$. Given the acceptance of the TPC detector is $|\eta| < 0.8$, this selection removes the tracks that may be affected by the edge effect. It ensures that in the selected η region, the track reconstruction efficiency is homogeneous.

4.3.3 List of Single Track Pre-Selection

Table 4.3 lists the criteria used for track selection. These selections are applied to the track candidates for D^0 reconstruction. These selections improve the signal to background ratio of the reconstructed D^0 candidates.

4.4 Topological Selections

The selection of D^{*+} on topological variables consists of two parts. One part of the selections is made on the topology of the $D^0 \rightarrow K^- \pi^+$ decay. The

Track selection	threshold value
Track status	ITSrefit TPCrefit
Clusters in SPD (max. 2)	≥ 1
Clusters in TPC (max. 160)	≥ 70
Transverse momentum p_T (GeV/ c)	> 0.5
Pseudorapidity $ \eta $	< 0.8

Table 4.3: List of parameters used for track selection. Only tracks passing all these selection criteria are used for D^0 reconstruction.

other part of the selections is made on the $D^{*+} \rightarrow D^0\pi^+$ decay (shown in Fig. 4.1).

The decay length of the D^{*+} meson is in the order of ~ 1 pm. It is impossible to identify the D^{*+} decay point from its production point. Thus, in a reconstructed event, the $D^{*+} \rightarrow D^0\pi^+$ decay topology is very simple. Both the daughter particles D^0 and π_s^+ are stemming from the primary vertex.

On the other hand, the decay length of the D^0 meson is in the order of $\sim 100\mu\text{m}$. With the help of the ITS detector, we are able to identify the D^0 decay point from its production point. By applying topological selections, we are able to enhance the D^0 signal in the D^0 candidates.

4.4.1 Topological Selections of D^0

Shown in Fig. 4.1, a $D^0 \rightarrow K^-\pi^+$ decay has a general two-prong decay topology, where the two curves of secondary particle trajectories have a superposition as considered a secondary decay vertex. Based on the two-prong decay topology, a number of selections and cuts are made to improve the significance of signal from background:

- cut on $p_{\text{TK},\pi}$ (transverse momentum of a secondary track), which represents the curvature of the track;
- cut on $d_0^{K,\pi}$ (track impact parameter with respect to the primary vertex);
- cut on $d_0^K \times d_0^\pi$ (product of the two impact parameters);
- cut on DCA (Distance of Closest Approach);

- cut on $\cos\theta_{\text{point}}$ (pointing angle), the angle between reconstructed D^0 momentum vector and the vector from the primary vertex to the secondary vertex;
- cut on $\cos\theta^*$ (decay angle), the angle between the momentum vector of reconstructed D^0 in laboratory frame and the momentum vector of reconstructed positive secondary particle in the center of mass frame;
- cut on the invariant mass of D^0 ;
- cut on $p_{T(\pi_s)}$ (transverse momentum of the soft pion),

The distributions of these topological variables are different between the signal and the background. The selections on the topological variables improve the signal to background ratio. The threshold of each selection is chosen to be the value at which a maximum D^{*+} significance is obtained.

In the topological selections of the D^0 mesons, the signals are the D^0 candidates with both K, π tracks originating from a D^{*+} meson. Those D^{*+} mesons decay into D^0 mesons, and the D^0 mesons decay further into K and π mesons. The other D^0 candidates with K, π not inherited from a same D^{*+} meson are considered background.

One thing is worth noting here. There are such D^0 candidates with the combination with K, π tracks which are decayed from a D^0 mesons, but such D^0 mesons are not stemming from a D^{*+} decay. These D^0 candidates are not considered as signals, although they have the same topological distribution as the signals. In the Δm distribution, these D^0 candidates will behave as background anyway, since they do not form a D^{*+} resonance with a pion.

Selection on p_T of the Daughter Tracks As shown in Fig. 4.5, the daughter tracks of D^0 background are heavily weighted at low p_T . The daughter tracks of D^0 signals have relatively higher most probable value of p_T . A selection on the p_T with a lower threshold may increase the significance of the D^0 . It will also increase the signal D^0 as daughters from D^{*+} decay.

This selection is different from the p_T selection on the single track. Those tracks failed the single track selection are not used in the D^0 reconstruction. They are not combined with another track to reconstruct the D^0 candidates. However, this p_T selection is made on the D^0 candidates, by comparing the threshold with the p_T of their daughter tracks. As the threshold is chosen differently for each p_T interval of the D^{*+} meson, a track that fails the selection in one D^0 candidate may pass the selection in another D^0 candidate.

Selection on Impact Parameter d_0 of Daughter Tracks The impact parameter is the distance of closest approach between a track and the primary vertex. The impact parameter can be disentangled into two projections, the projection in transverse plane $r-\phi$ and in beam axis z . The impact parameter in the $r-\phi$ plane is defined as:

$$d_0(r\phi) = q[\rho - \sqrt{(x_V - x_0)^2 + (y_V - y_0)^2}]. \quad (4.3)$$

Here q is the charge sign of the particle, ρ is the radius of the track curve projected in the transverse plane, and (x_0, y_0) is the center of the projected (arch shaped) curve. The primary vertex point has the coordinates (x_V, y_V) . The impact parameter projection in beam direction z is:

$$d_0(z) = z_{track} - z_V, \quad (4.4)$$

where z_V is the position of the primary vertex in beam direction, and z_{track} is the z direction projection of the closest approach point to the primary vertex on the track. Due to the resolution of the ITS detector, the measured impact parameter in the $r-\phi$ plane is much more precise than the measured impact parameter in z direction. Thus, the selection is made only on $d_0(r\phi)$. In the thesis, the term d_0 implies $d_0(r\phi)$.

The D^0 daughter tracks K, π originate from the secondary vertex, which is displaced from the primary vertex by typically $c\tau = (123.0 \pm 0.4) \mu\text{m}$. The impact parameter d_0 of the daughter tracks has similar magnitude. The average impact parameter is $d_0^{K,\pi} \approx 105 \mu\text{m}$ in the rapidity range $|y| < 1$, according to a calculation from [8].

Figure 4.6 shows the distribution of impact parameters d_0 for π tracks from different sources. The sign for the impact parameter indicates the direction from the primary vertex to the track, as shown in Eq. 4.3. For a positive charged track, it has a positive d_0 if the primary vertex is outside the curve, and a negative d_0 if the primary vertex is inside the curve. It is the opposite for a negative charged track.

The data is from PYTHIA simulation. At large absolute values of d_0 , the signal is limited by statistics. The background is dominated by wrong combinations of primary tracks. Other background track sources are given by tracks with large impact parameter coming from the decay of hyperons, e.g. Λ, Ξ , and Ω and decays from K_S^0 . Some of the primary tracks undergo multiple scattering in the material of the beam-pipe and of the innermost detector layer and appear at large impact parameter. Annihilation of \bar{p} and \bar{n} in the beam-pipe and the innermost SPD layer also lead to background tracks with large impact parameter. Both the signal and the background tracks are heavily distributed at small d_0 . A selection on the absolute value

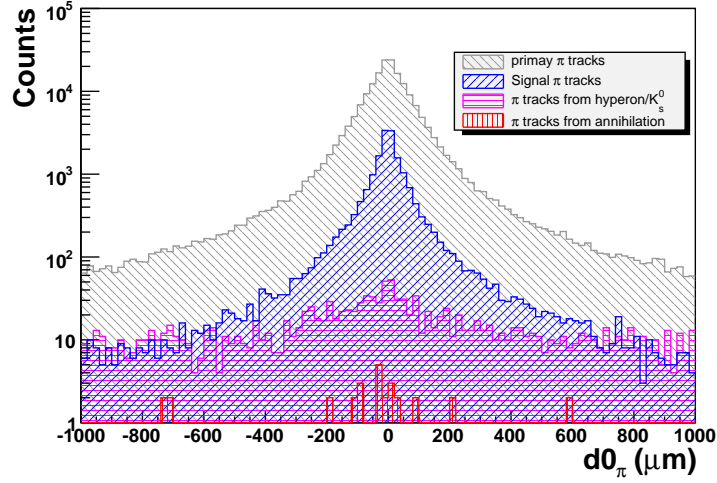


Figure 4.6: Impact parameter distribution of π tracks. Gray: primary π tracks; Blue: Secondary π daughter tracks from D^0 decay; Magenta: π tracks from hyperons, e.g. Λ , Ξ , and Ω decay and from K_S^0 decay; Red: π tracks decay from \bar{p} annihilation in the beam pipe or detector material.

of d_0 with a upper threshold may reduce many of the D^0 background. The removal of the background tracks may increase the D^{*+} significance. At the same time, the removal of the signal tracks may also decrease the D^{*+} significance. However, the removal of the background makes a larger effect on the D^{*+} significance, since the number of D^0 candidates scales approximately with the square of the track number, and most of them are background D^0 .

Selection on Impact Parameter Product $d_0^K \times d_0^\pi$ of the Daughter Tracks The impact parameter indicates not only the distance of closest approach from the primary vertex to a track, but also the relative position from the primary vertex to a track. For a track with positive charge, the impact parameter is positive if the primary vertex is outside the track curve, and the impact parameter is negative if the primary vertex is inside the track curve. For a track with negative charge, the sign of the impact parameter is reversed. As is shown in Fig. 4.7, the product of impact parameters of the daughter tracks from a signal D^0 has a negative sign.

In the case of the $D^0 \rightarrow K^-\pi^+$ decay topology, the two signal tracks in a combination stemming from the same mother D^0 meson have the primary vertex relatively either both inside or outside. Considering the opposite charge of the two tracks, the product of the impact parameters in a signal combination has a negative value. The distribution of the product $d_0^K \times d_0^\pi$

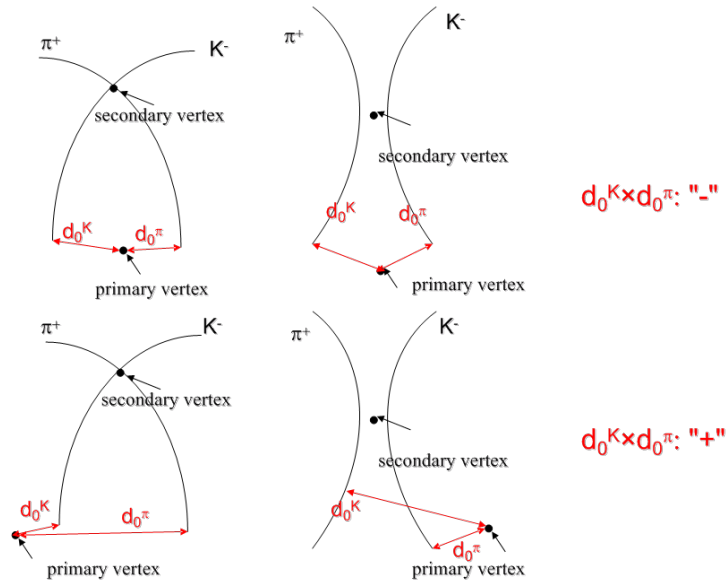


Figure 4.7: Sign of the product of the impact parameters of the two tracks from the decay of D^0 in the transverse plane. The ones with negative impact parameter products are candidates track pairs from D^0 decays .

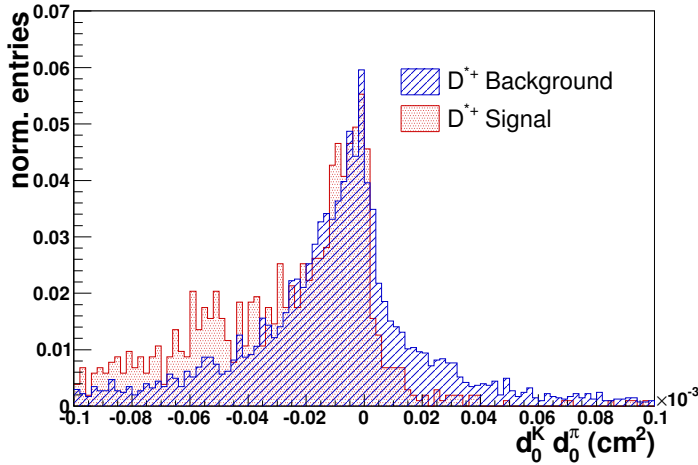


Figure 4.8: The product of the impact parameters of the K, π tracks from D^0 candidates. The signals are the D^0 candidates decayed from D^{*+} mesons. The background are the other D^0 candidates.

is shown in Fig. 4.8. The difference between the signal and background is significant. The distribution is deteriorated due to the finite resolution of the primary vertex reconstruction. Thus there are some signal entries with

positive values of $d_0^K \times d_0^\pi$. The background is from random combination of tracks with equal positive and negative impact parameters, thus the distribution of their product is symmetric.

An upper threshold of $d_0^K \times d_0^\pi$ is applied in the selection. A large portion of the background D^{*+} mesons are removed, while most of the signal D^{*+} mesons are kept.

Selection on DCA of Daughter Tracks The distance of closest approach directly represents the topological correlation between two K, π daughters stemming from a D^0 decay. The distance is calculated from the two extrapolated track curves, and then projected on the $r - \phi$ plane. With perfect tracking, the signal combinations have a DCA of 0, which means the two curves cross at the decay vertex. In practice with finite spatial resolution, the DCA distribution of the signal is dispersed from 0, while the background distribution is much wider, as shown in Fig. 4.9.

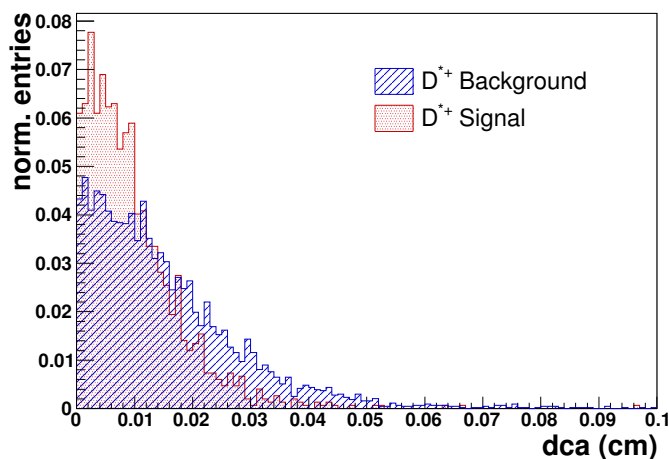


Figure 4.9: Distribution of the distance of closest approach of the two daughter tracks.

An upper threshold of DCA is applied in the selection, in order to increase the D^{*+} significance.

Selection on Pointing Angle $\cos \theta_{\text{point}}$ of the Reconstructed Mother Particle In the case of the $D^0 \rightarrow K^- \pi^+$ decay topology, the pointing angle is the angle between the direction of the reconstructed D^0 momentum and the direction from the primary vertex to the secondary vertex. This distribution is shown in Fig. 4.10. Since the D^0 is originating from the primary vertex,

the decay angle of a signal D^0 is distributed around 0° . The signal entries with large decay angle are from D^0 decays at short decay length. This is because that the resolution of the pointing angle becomes very low, when the distance between the primary and secondary vertex is short.

The $\cos\theta_{\text{point}}$ distribution of the background is much flatter. More entries are distributed where $\cos\theta_{\text{point}}$ is small. A lower threshold of $\cos\theta_{\text{point}}$ will remove background combinations, while keeping most of the signals.

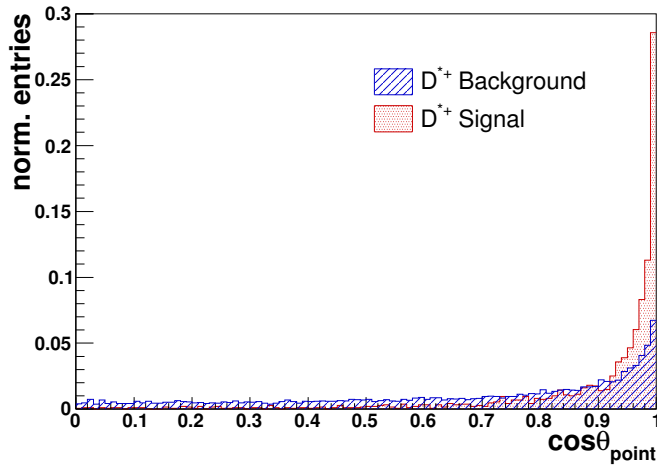


Figure 4.10: Cosine of the pointing angle between D^0 flight line and its reconstructed momentum direction. Hereby shown are the distributions of signal and background from $D^{*+} \rightarrow D^0\pi^+$ decays.

Selection on Decay Angle $\cos\theta^*$ of the Decay The decay angle θ^* is defined as, in the reference frame of the D^0 particle, the angle between the pion momentum and the D^0 flight direction. The θ^* of the signal D^0 mesons is distributed in the direction where the daughter momenta in the D^0 frame is perpendicular to the D^0 flight line. On the other hand, the background is more enhanced in the direction where the daughter momenta is along or opposite to the D^0 flight direction. The $\cos\theta^*$ distribution of signal and background are shown in Fig. 4.11.

An upper threshold of the decay angle is applied in the selection, in order to increase the D^{*+} significance.

Selection on Invariant Mass of D^0 The selection of the reconstructed D^0 candidates which pass the selections on the invariant mass spectrum will

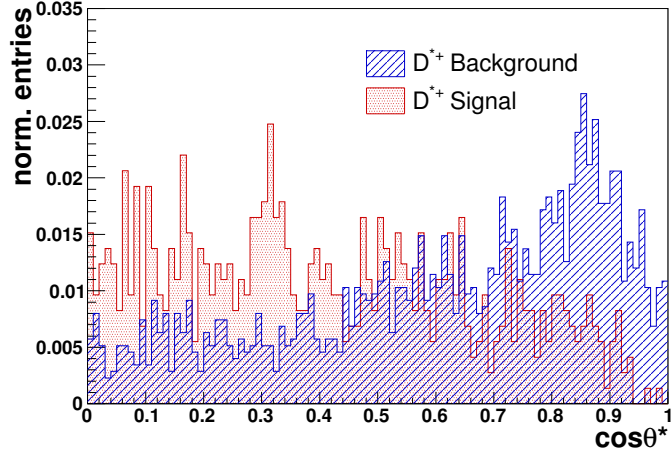


Figure 4.11: The distribution of $\cos \theta^*$. Hereby shows respectively the entries of signal and background from $D^{*+} \rightarrow D^0 \pi^+$ decay.

remove most of the background from the candidate D^0 which is used for the combination with soft pion. The selection is made in the region of $\pm 3\sigma$ of a Gaussian fit on the D^0 invariant mass peak.

4.4.2 Cuts Optimization

Both the D^{*+} signal and background counts depend on the threshold value of the selection, so does the D^{*+} significance. We show the distribution of the significance as a function of the threshold value in Fig. 4.12. The thresholds may be chosen such that the D^{*+} significance is the largest.

However, the cut variables are not independent from each other. Correlations between the cut variables exist, e.g. between the $d_0^{K,\pi}$ and $d_0^K \times d_0^\pi$. The significance of the reconstructed D^{*+} mesons is a function of the multi-dimensional cut variables. We need to find a point in this multi-dimensional space, where the significance reaches its maximum.

The idea of optimizing the cut value is to approach the optimum multi-dimensional coordinate in one direction after another direction. Firstly, no topological cuts are applied. The significance dependencies on each variable are plotted. The cut threshold on each variable is chosen where the corresponding significance reaches its maximum. These threshold values are the initial values. If there are no correlations between cut variables, these values will be the final optimum threshold values. Secondly, the initial cuts are applied on all the variables. The significance dependency on one variable is plotted. A new optimum value is found, and the threshold value of the cut

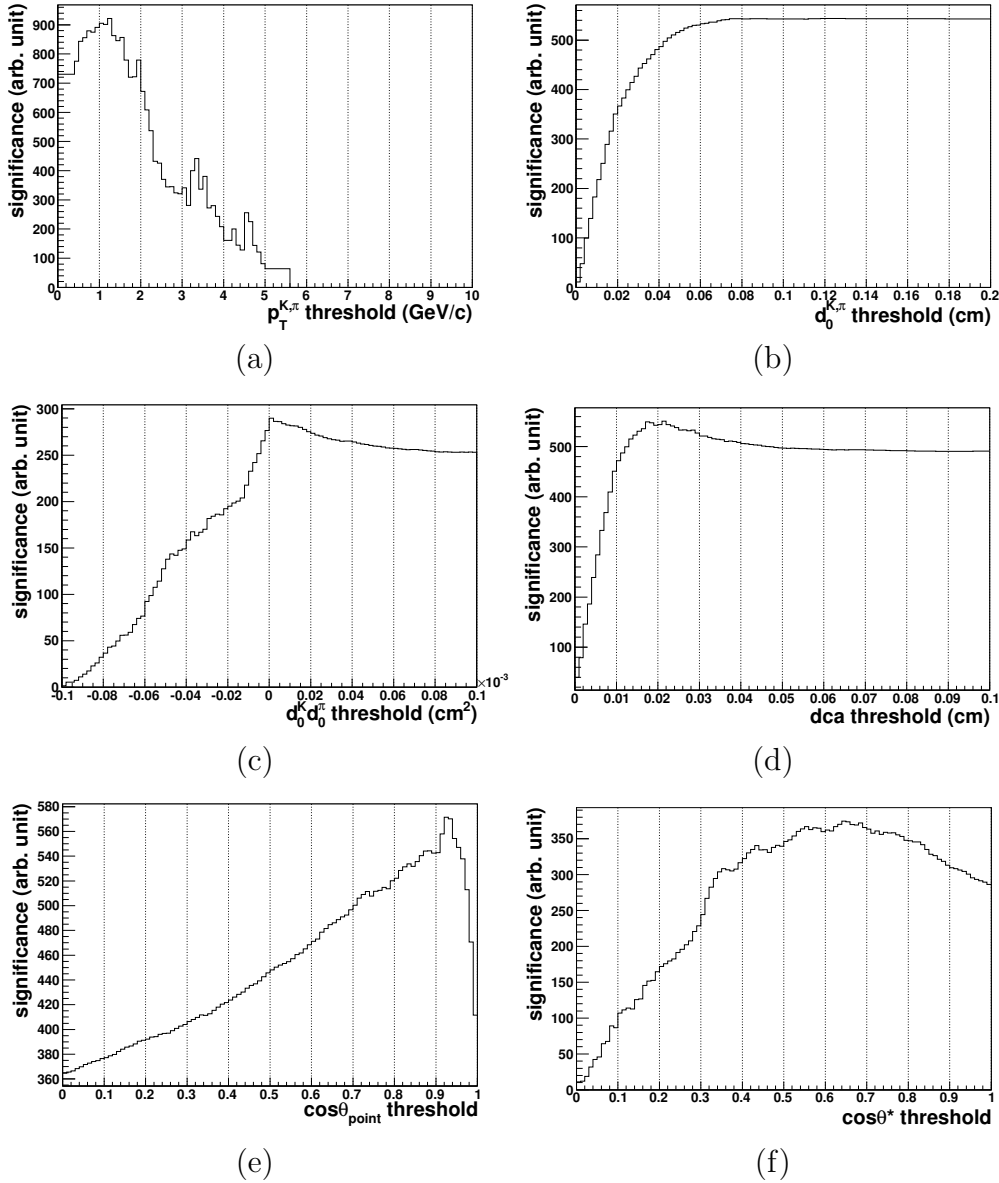


Figure 4.12: Significance of reconstructed D^{*+} as functions of selection thresholds. The selections are applied on 6 topological variables independently. These variables are $p_T^{K,\pi}$ (a), $d_0^{K,\pi}$ (b), $d_0^K \times d_0^\pi$ (c), DCA (d), $\cos\theta_{\text{point}}$ (e), $\cos\theta^*$ (f). This was studied with 150M simulated p-p collision events with PYTHIA.

on this variable is updated by the new value. Then, the updated cut values are applied. The significance dependency on another variable is plotted. The

threshold value of the cut on this variable is also updated. This procedure is done for all the variables consequently. When all variables are processed, more iterations over the variables are performed, until the difference of every cut values to the previous iteration is smaller than a quantified threshold.

The cut optimization is operated on PYTHIA simulation. The cut values are determined in several $p_T(D^{*+})$ bin, as shown in Table. 4.4. The cut variables reach their optimum values and are stable after 5 iterations. The distributions shown in Fig. 4.12 are after the optimization procedure, where the optimized thresholds are applied on all the variables.

p_T (GeV/c)	dca (cm)	$\cos\theta^*$	$p_T^{K,\pi}$	$d_0^{K,\pi}$ (cm)	$d_0^K \times d_0^\pi$ (cm ²)	$\cos\theta_{\text{point}}$
1-2	< 0.03	< 0.7	> 0.8	< 0.1	< -0.00002	> 0.9
2-3	< 0.03	< 0.7	> 0.8	< 0.1	< -0.00002	> 0.9
3-5	< 0.03	< 0.7	> 0.9	< 0.1	< -0.000002	> 0.8
5-8	< 0.03	< 0.7	> 1.0	< 0.1	< -0.000002	> 0.8
8-24	< 0.03	< 0.7	> 1.0	< 0.1	< -0.000002	> 0.8

Table 4.4: Optimized thresholds of the topological selections in various p_T intervals.

4.5 Particle Identification

The particle identification (PID) is applied on selections of the tracks used for D^0 reconstruction are kaons and pions. The PID is not applied on soft pion π_s^+ candidates. The PID information is acquired from TPC and TOF respectively. The TPC provides identification of kaon and pion up to a transverse momentum of 0.7 GeV/c, and the TOF makes it up to 2 GeV/c.

4.5.1 PID Selections on D^0 Daughter Particles

The TPC identifies kaon and pion clearly up to a momentum of 0.7 GeV/c. One can see from the dE/dx distribution as a function of track momentum, where the kaon and pion bands are separated more than 3 times of the standard deviation below 0.7 GeV/c. For tracks above 0.7 GeV/c kaon and pion bands starting to merge in the dE/dx distribution, where the identification of kaon and pion is not 100% effective.

In the present analysis, the the PID method is applied in a way that an optimum efficiency has priority. In other words, the PID information is only used to discard identified wrong tracks. Practically, we select a $\pm 2\sigma$ band-shaped region of a kaon distribution, and the particles outside the region are

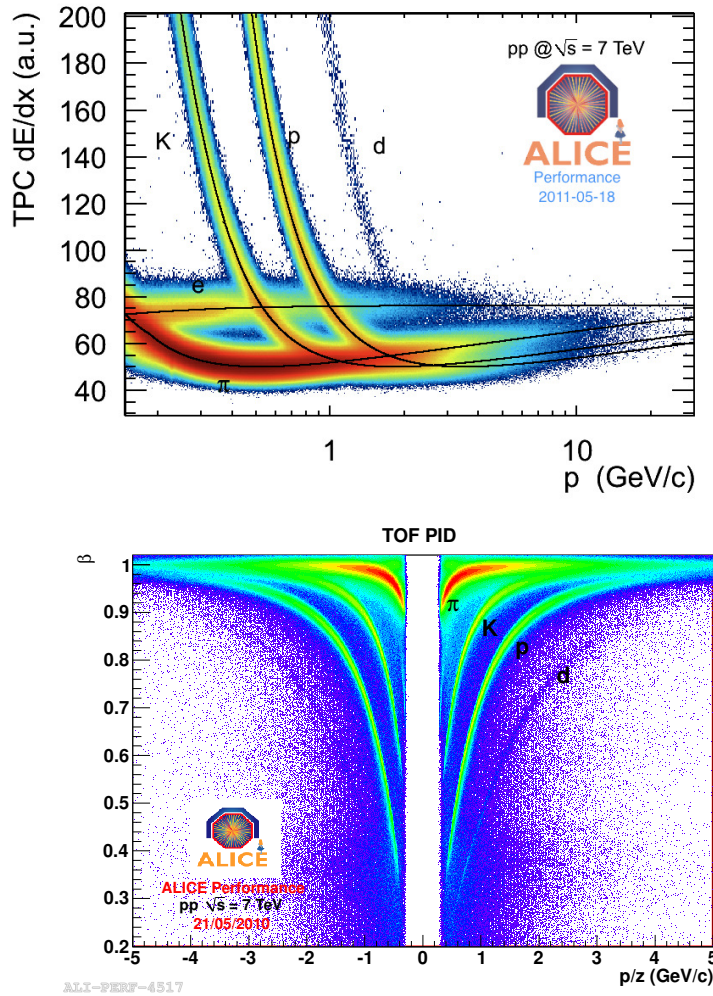


Figure 4.13: Top: TPC Signal of particle energy loss versus the momentum. Bottom: TOF Signal of particle velocity versus the momentum divided by the charge.

considered not a kaon. The same method is used for pion selection. The tracks in the region where two bands are overlapping are considered both as a candidate of kaon and pion.

There is PID information provided by time of flight, too. The distribution of kaon and pion tracks are also in a band-shape region in the flight time distribution as a function of particle momentum. The two band from kaon and pion are separated 3σ up to a momentum of 1.5 GeV/c. Here the selection of $\pm 3\sigma$ of kaon and pion band is applied. The region outside the region is considered not a kaon and not a pion.

The combination of the two PID method is rejection on identified non kaon or non pion. i.e., a track is excluded from kaon candidates, if it is identified a non kaon by either TPC or TOF, and the same for pion.

The PID efficiency is not 100% from TPC and TOF. A track may hit the non-effective area of the detector, do not have enough hits to have a valid PID information or do not have enough transverse momentum to hit the detector. The TPC has a PID efficiency nearly 100% for tracks over 150 MeV/ c . But TOF has only 60% efficiency for track over 500 MeV/ c . To have the optimum efficiency of the selections, we keep the tracks without PID information also as particle candidates of kaon and pion.

Table. 4.5 shows the TPC PID and TOF PID application algorithm for kaon and pion. The combined PID is require both TPC and TOF PID return TRUE value. This is because by definition, either of the two gives a nearly perfect rejection efficiency.

TPC PID availability	TPC in 2σ	TPC PID
YES	YES	TRUE
YES	NO	FALSE
NO	-	TRUE
TOF PID availability	TOF in 3σ	TOF PID
YES	YES	TRUE
YES	NO	FALSE
NO	-	TRUE

Table 4.5: TPC and TOF PID criteria for a given track (valid for both kaon and pion).

Candidate Charge and Reflection The selection is applied on both tracks used for the combination, *i.e.* one kaon track and one pion track. For the present analysis, both D^0 and \overline{D}^0 are reconstructed, via the channels $D^0 \rightarrow K^-\pi^+$ and $\overline{D}^0 \rightarrow K^+\pi^-$ respectively. From reconstruction, we reconstruct D^0 by assigning negative tracks the kaon mass and positive tracks the pion mass and calculate the invariant mass of the two, and vice versa for \overline{D}^0 reconstruction. Without the PID information, the invariant mass distribution is contaminated by the combination with a wrong mass assigned, *i.e.* a positive pion and a negative pion are combined with a wrong mass assigned to the positive particle and make up an entry in the invariant mass distribution of \overline{D}^0 .

With the help of TPC and TOF PID, this contamination is reduced to the extent where the efficiency is still not affected. What remains

in contamination is dominated by the combinatorial background from uncorrelated tracks. But there is another source of background which from real D^0 and \bar{D}^0 daughters but assigned by the wrong mass to daughter candidates. While the entry with correct mass assigned is still in the invariant spectrum, this wrong-mass-assigned invariant mass is a reflection. It has fewer entries than the signal, since it requires both of the two tracks are in the overlapping region in TPC dE/dx and Time of Flight spectra. But it needs to be corrected afterwards, since it distributes around the D^0 mass and has entries beneath the peak area in D^0 and \bar{D}^0 invariant mass spectrum.

4.5.2 PID Selection on the D^{*+}

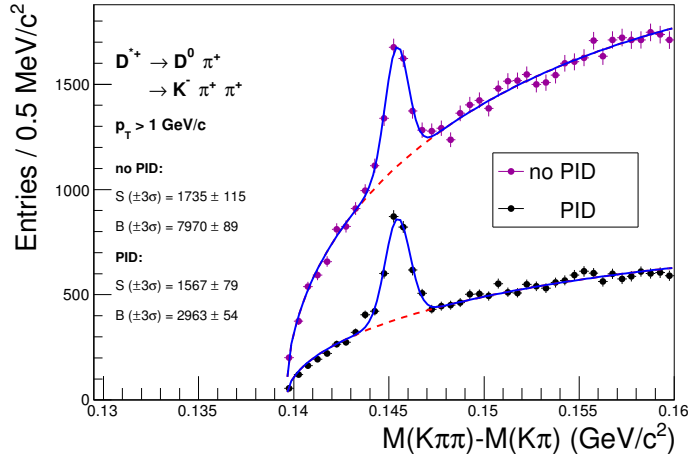


Figure 4.14: $\Delta m = m_{D^{*+}} - m_{D^0}$ invariant mass spectrum from p-p collisions at $\sqrt{s} = 7$ TeV without particle identification, and with a 2σ selection from the specific energy loss in the TPC, and an additional 3σ selection in the time of flight.

Particle identification has been applied to the daughter candidate K, π tracks of D^0 . It is not applied on the soft pion for two reasons. One is that, the soft pion detection efficiency is low. The second is that, at the low momentum region, pions are dominant in the amount, where PID does not increase the purity significantly. So for the D^{*+} reconstruction, the PID is applied on the D^0 daughters.

The effect of PID selection is shown in Fig. 4.14. Pions and kaons were selected within a 2σ band from the specific energy loss in the TPC, and an additional 3σ selection in the time of flight has been applied. While the

background is drastically decreasing, we have checked that 90% of the D^{*+} signal survives the selection, as one would expect.

4.6 Yield Extraction

To extract the yield of the signal, the distribution of both the signal and the background should be understood well. The signal is expected to follow a Gaussian distribution. The background, on the other hand, can not be parametrized in a simple way. The distribution of the background is both statistical and kinematical. Furthermore, the peak in the ΔM invariant mass distribution is at the edge near the kinetic boundary, where the entry density decreases deeply with ΔM getting smaller. Here, two methods are used to describe the background, fit with parametrized function and use D^0 side bands to simulate the background shape.

4.6.1 Background Fit

The fit function for D^{*+} background is the product of square root function and exponential function, which was used in [6]. It is written as

$$f_{BKG}(\Delta M) = A\sqrt{\Delta M - m_\pi} \cdot e^{B(\Delta M - m_\pi)}. \quad (4.5)$$

The signal is fitted by Gaussian function

$$f_{SIG}(\Delta M) = \frac{A}{\sqrt{2\pi}B} e^{-\frac{(\Delta M - C)^2}{2B^2}}. \quad (4.6)$$

The fitting procedure is in three steps. First, the non-peak region of the spectrum is fitted with the background function only. Second, using the parameter from last step, fit the whole spectrum with signal + background function. Third, recalculate the background function with fit signal + background function over the whole spectrum.

The yield of the Gaussian fit over signal is obtained from the integral, parameter A. Thus the raw yield is A normalized by the bin width.

4.6.2 Bin Counting

Another signal yield extraction method is bin counting. The signal + background in -3σ to 3σ of the peak region is obtained by adding the counts

in the corresponding bins. The 3σ is mostly not at the bin edge position, one may choose a counting with or without the last bin.

The background is obtained by an integration of the fit function of the background shape, over the selected bin range. Then the subtraction between the counted count and the integration is the signal yield.

4.6.3 D^0 Sideband

The background distribution is also estimated by using the D^0 sideband background. The background D^0 candidates near the peak in D^0 invariant mass spectrum are kinetically similar to the signal region. Thus a calculation of this D^0 background and soft pion gives a good approximation of the background distribution in the signal region.

The D^0 sideband is selected from $\pm 10\sigma$ to $\pm 4\sigma$, while the signal D^0 is selected from -3σ to 3σ . The width of selection is twice as that of the signal, which is because on one hand, the statistical error of the side band is smaller with larger statistics, and on the other hand, the sideband is still not too far away from the signal that the kinetic behavior of those candidates are still similar to the signal. The sideband background in ΔM invariant mass spectrum is then normalized to the measured spectrum, and then subtracted from the latter. The subtracted spectrum is fitted with Gaussian function.

4.6.4 Raw Yields

Finally, the yield is extracted from the reconstructed spectrum. Figure 4.15 shows the invariant mass spectrum.

The resulting invariant mass $\Delta m = m_{D^{*+}} - m_{D^0}$ distribution from p-p collisions is shown in Fig. 4.16 for 10 different p_T regions. The D^{*+} signal appears as a narrow peak of width $\sigma \approx 0.6 \text{ MeV}/c^2$ centered at a mean of $(145.4 \pm 0.1) \text{ MeV}$, which is in excellent agreement with values from the PDG [7]. Note that the width of the reconstructed D^0 meson is in the order of $10 \text{ MeV}/c^2$. By taking the mass difference $\Delta m = m_{D^{*+}} - m_{D^0}$, the width in the reconstructed D^{*+} meson is solely given by the momentum resolution of the soft pion and thus much narrower. The background is kinematically restricted at lower invariant mass at a value corresponding to the pion rest mass of $m_{\pi^+} = 139.57 \text{ MeV}/c^2$ [7]. With the given statistics, the signal extends up to $p_T < 24 \text{ GeV}/c$ and is almost background-free at these high momenta.

The background is smoothly increasing with invariant mass and steeply decreasing with the transverse momentum of the reconstructed D^{*+} . This reflects the inclusive single particle spectra of daughter candidates K^-, π^+

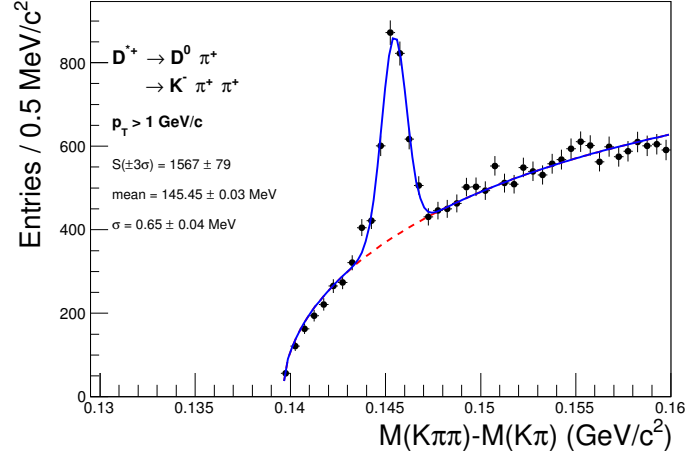


Figure 4.15: ΔM invariant mass spectrum from minimum bias p-p collisions at $\sqrt{s} = 7$ TeV, integrated over $p_T > 1$ GeV/ c and $|\eta| < 0.8$.

p_T bin (GeV/ c)	Signal	Background	Significance
1 - 2	46 ± 21	525 ± 23	1.9 ± 0.9
2 - 3	265 ± 49	1373 ± 37	6.5 ± 1.2
3 - 4	435 ± 43	1013 ± 32	11.4 ± 1.1
4 - 5	323 ± 27	257 ± 16	13.4 ± 1.1
5 - 6	209 ± 19	87 ± 9	12.1 ± 1.1
6 - 7	119 ± 15	41 ± 6	9.4 ± 1.2
7 - 8	74 ± 9	7 ± 3	8.2 ± 1.0
8 -12	101 ± 11	14 ± 4	9.4 ± 1.0
12 -16	22 ± 5	2 ± 1	4.6 ± 1.0
16 -24	9 ± 3	0 ± 0	2.9 ± 1.0

Table 4.6: The reconstructed yields of $D^{*+} + D^{*-}$ signal and background in 10 p_T intervals. The corresponding significances ($\frac{\text{signal}}{\sqrt{\text{signal}+\text{background}}}$) are shown as well.

which is steeply decreasing with momentum leading to less combinatorial background.

4.7. QA of the D^{*+} Reconstruction

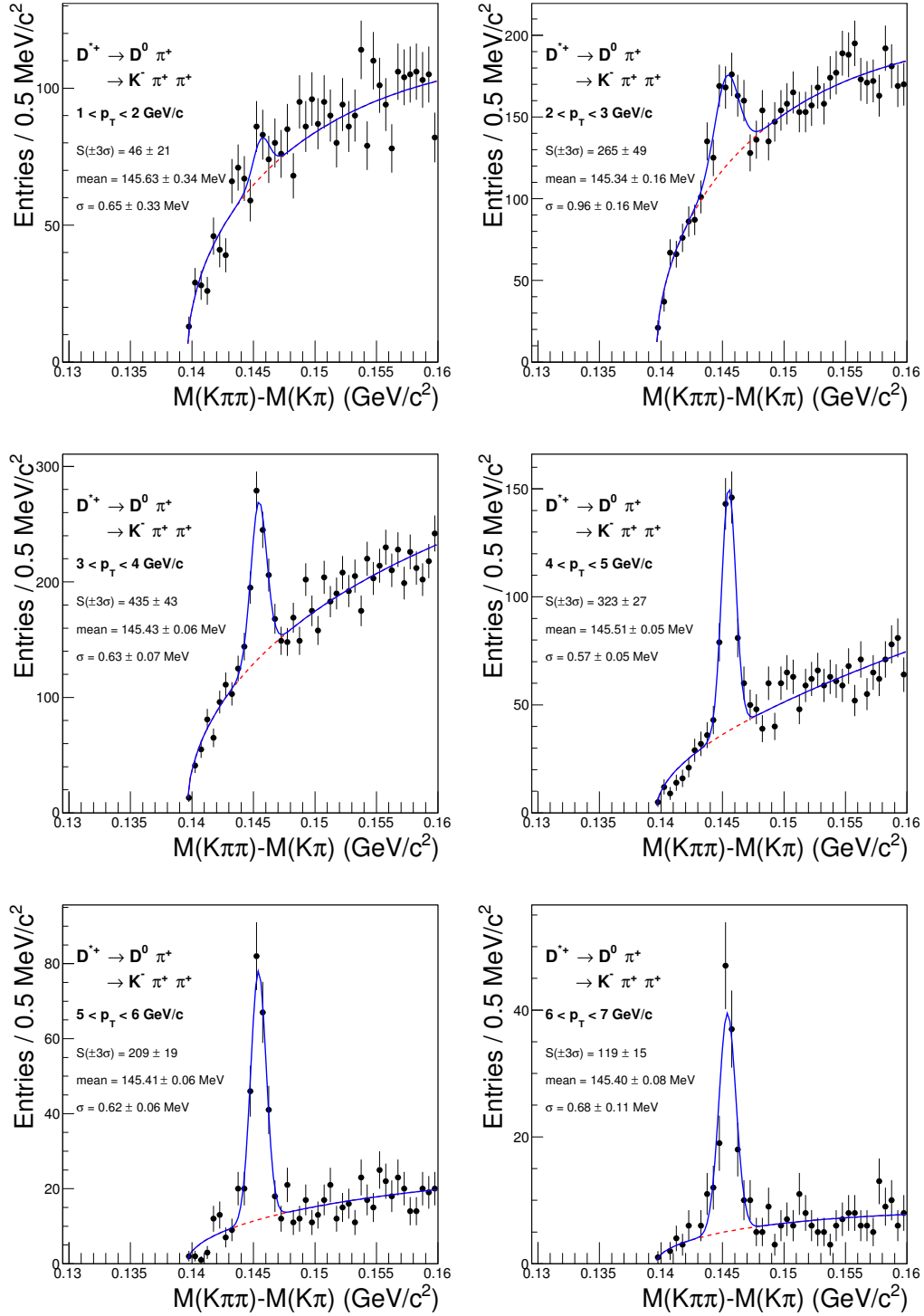


Figure 4.16: $\Delta m = m_{D^{*+}} - m_{D^0}$ invariant mass spectrum in 10 p_T bins from 1 GeV/c to 24 GeV/c for minimum bias p-p collisions at $\sqrt{s} = 7$ TeV.

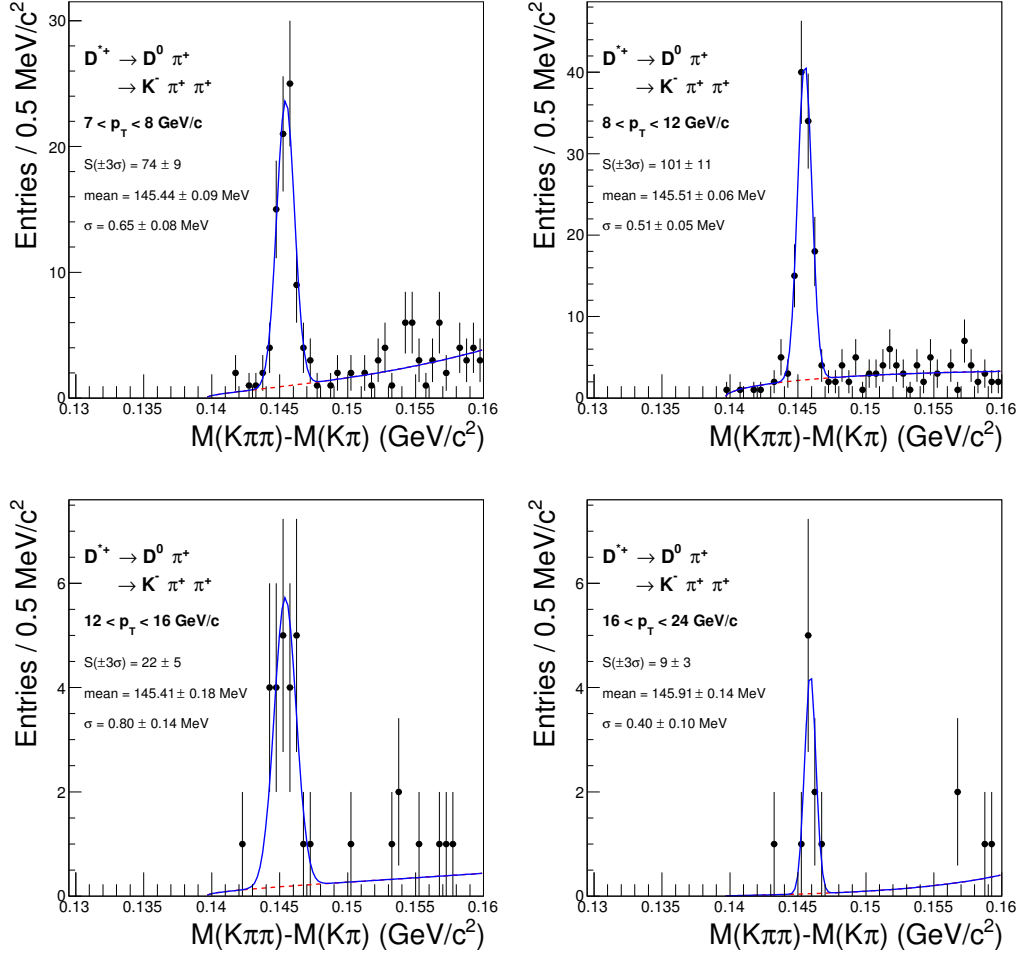


Figure 4.16: $\Delta m = m_{D^{*+}} - m_{D^0}$ invariant mass spectrum in 10 p_T bins from 1 GeV/c to 24 GeV/c for minimum bias p-p collisions at $\sqrt{s} = 7$ TeV.

4.7 QA of the D^{*+} Reconstruction

4.7.1 Reconstructed D^{*+} Yield

The signal of reconstructed D^{*+} are extracted from the integral of a Gaussian fit over the invariant mass peak. Similarly, the background yields are extracted from the integral of a fit function over the background within $\pm 3\sigma$, where σ is the width of the invariant mass peak. Their signal and background yield in each p_T bins are shown in Fig. 4.17.

The distribution of the signal raw yields has a maximum in the bin of $3 < p_T < 4$ GeV/c. This is because, at low p_T , the reconstruction

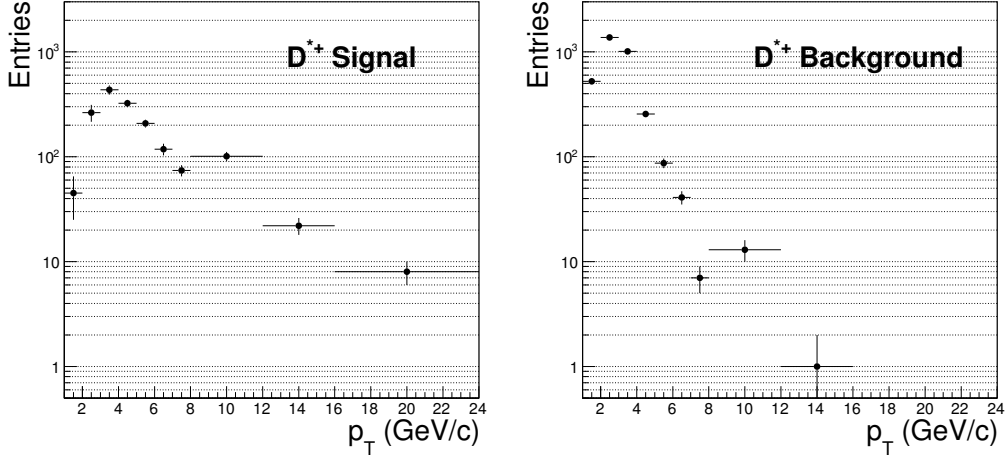


Figure 4.17: Extracted D^{*+} signal and background in $\pm 3\sigma$ region, from minimum bias p-p collisions at $\sqrt{s} = 7$ TeV. The results are shown in 10 p_T bins from 1 GeV/ c to 24 GeV/ c .

has tight selection to reduce the background count, where the efficiency is low. At higher p_T , the cross section is small, where the yield suffers from low production. The background distribution has a similar shape, with a maximum in the bin of $3 < p_T < 4$ GeV/ c . The difference between the signal and background distribution is that the background decreases more rapidly with increasing p_T . This indicates that the signal spectrum is "harder" than the background spectrum, since charmed hadrons have a higher average p_T . Note the step in the raw yield at 8 – 24 GeV/ c , due to the increase of the bin width.

The Significances of the reconstructed $\Delta m = m_{D^{*+}} - m_{D^0}$ invariant mass distribution are shown as a function of D^{*+} p_T in Fig. 4.18. Except for the first and last p_T bin, all the D^{*+} signals are reconstructed with large significances. The large significances verify our D^{*+} reconstruction measurement, and also guarantee relatively small statistical and systematic uncertainties .

4.7.2 Reconstructed D^{*+} Mass

The reconstructed D^{*+} masses are shown in the left panel of Fig. 4.19. Those masses are extracted from the fit with Gaussian over the invariant mass spectra in a certain p_T range. The center and its standard deviation are determined by the free parameter C in the fit function Eq. 4.6.

The current PDG value is $\Delta m = 145.421 \pm 0.010$ MeV/ c^2 . The result

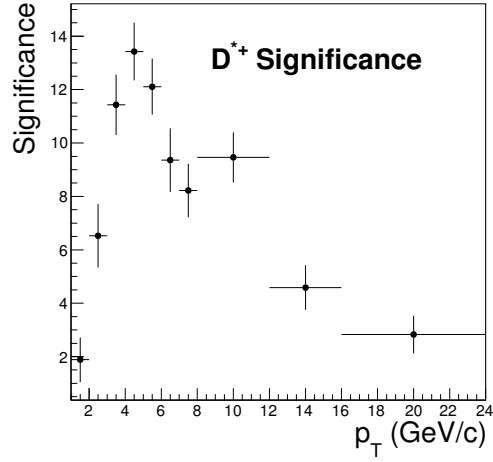


Figure 4.18: Significances of the reconstructed D^{*+} peaks, from minimum bias p-p collisions at $\sqrt{s} = 7$ TeV. The results are shown in 10 p_T bins from 1 GeV/ c to 24 GeV/ c .

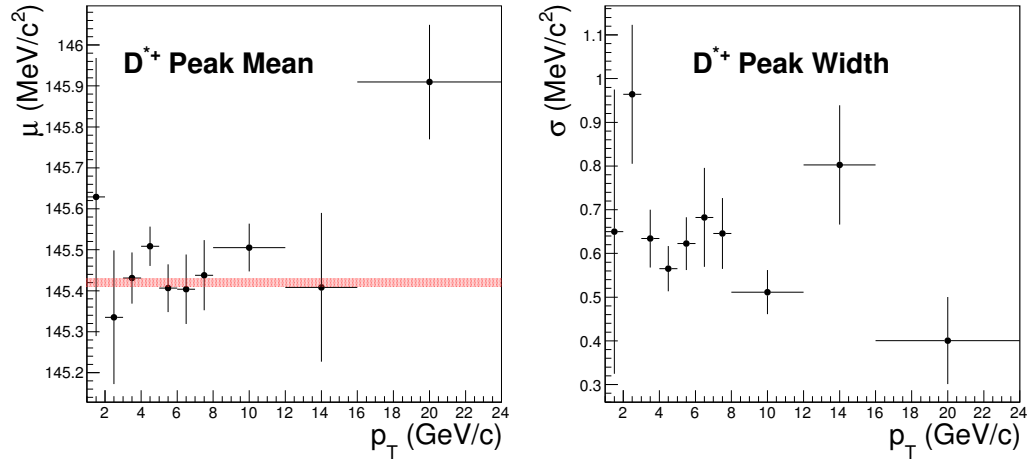


Figure 4.19: Mean and width of $\Delta m = m_{D^{*+}} - m_{D^0}$ invariant mass peak, from minimum bias p-p collisions at $\sqrt{s} = 7$ TeV. The results are shown in 10 p_T bins from 1 GeV/ c to 24 GeV/ c . The value of Δm from PDG [7] is shown in red.

is well distributed around the PDG value. The standard deviation is only ~ 0.1 MeV/ c^2 , which is at a 0.07% level. The uncertainty is mainly due to the binning and the finite statistics. The bin width used for the invariant mass spectrum is 0.5 MeV/ c^2 , and the invariant mass peak range contains

6 – 8 bins. The result of mass center with an uncertainty of 1/5 bin width is acceptable. Another reason for the uncertainty of the mass peak is from the statistics of signal. The first and last p_T bin have few signal counts, and the means of the peaks have larger uncertainties.

For comparison, the measurement of D^0 in these events, from the channel of $D^0 \rightarrow K^- \pi^+$, has a mass center of $m(D^0) = 1.867 \pm 0.001 \text{ GeV}/c^2$. The absolute uncertainty is ten times larger, but the relative error (0.06%) is at the same level of D^{*+} measurement. This consistency supports the result of our analysis.

4.7.3 Reconstructed D^{*+} Mass Width

The peak widths of reconstructed D^{*+} are shown in the right panel of Fig. 4.19. Those widths of the peaks are extracted from the fit with a Gaussian over the invariant mass spectra in each p_T bin. The width and its standard deviation are determined by the free parameter B in the fit function Eq. 4.6.

The intrinsic width of the D^{*+} due to its life time accounts to $\Gamma = 96 \pm 22 \text{ keV}/c^2$. The peak width we observe in the analysis is $\sim 0.7 \text{ MeV}/c^2$, which is 7 times larger than the intrinsic width. The experimental result is dominated by the momentum resolution of the reconstructed daughter particles, is much larger than the decay width, and the latter one is "hidden" in the measured wider peak.

The width of the Δm invariant mass is much smaller than other resonance particles (e.g. the peak width of $D^0 \rightarrow K^- \pi^+$ is $14 \text{ MeV}/c^2$). This is because of the Δm is the subtraction between the D^{*+} and D^0 reconstructed masses, and K, π we used for calculating the D^0 mass are the same ones used in calculating the D^{*+} , with an additional soft π . The subtraction of the two masses cancels the K, π momentum resolution effect and only keeps the one from the soft π . Due to the subtraction between D^{*+} and D^0 invariant mass with, the momentum uncertainty of the daughter K^-, π^+ of D^0 is removed, and the width of Δm peak is only affected by the momentum uncertainty of the soft pion.

4.7.4 The D^0 and D^{*+} Invariant Mass Spectra

On the way of making the $\Delta M = M(D^{*+}) - M(D^0)$ distribution, we have made both the D^0 and the D^{*+} plots. But the background level is too high for us to see the signal peak there. However, we can apply selection around the peak in the $\Delta M = M(D^{*+}) - M(D^0)$ distribution and plot the invariant

mass of D^0 and D^{*+} . Their distributions of invariant mass spectra are shown in Fig. 4.20.

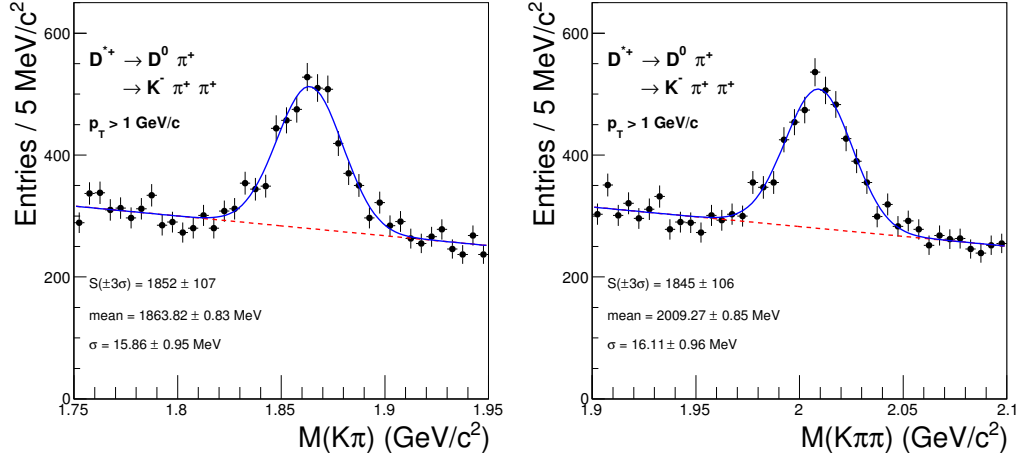


Figure 4.20: Invariant mass spectra of D^0 and D^{*+} from minimum bias p-p collisions at $\sqrt{s} = 7$ TeV, integrated over $p_T > 1$ GeV/c.

Both the mass peaks of D^0 and D^{*+} are well distributed around its value from Particle Data Group. Comparing the peak width to that of D^{*+} in ΔM invariant mass spectrum, the width is much larger for the reason that it corresponds to two track resolution combined, while the later correspond to the resolution of soft pion only. The signal count from the ΔM spectrum is slightly smaller than the count from the D^0 and the D^{*+} spectra, which is due to the cut on the D^0 invariant mass.

Chapter 5

Corrections

The reconstructed particles do not represent an identical set of the produced particles from the collisions. Detector geometry, detection efficiency, particle identification and reconstruction algorithm may affect the efficiency for detection. Thus, the efficiency is evaluated with simulated collision events, by calculating the ratio of reconstructed particles of a certain kind to the number of generated particles of the same kind. Then, the efficiency is used for correcting the extracted raw yield. In this chapter, the efficiency is defined first, and then the correction method is described. The efficiency of D^{*+} reconstruction is shown, followed by a study of correction on D^{*+} mesons feed-down from B mesons, a D^{*+} production source which is not negligible.

5.1 D^{*+} Efficiency

The reasons for a finite efficiency can be classified into two parts. One reason for the loss is the limitation in the detection method, e.g. detector geometry and detection efficiency. The other reason is due to artificial selections in the D^{*+} reconstruction. These artificial selections sacrifice the D^{*+} signal quantity, but improve the D^{*+} signal quality and reduce the uncertainty. In the analysis, the efficiency is unfolded into two steps, the acceptance and the reconstruction efficiency.

The acceptance is a pure instrumental effect. The D^{*+} acceptance is the ratio of the D^{*+} in the detector acceptance to the generated D^{*+} . The D^{*+} in the detector acceptance represent those D^{*+} mesons, the daughter particles

of which pass through the sensitive area of the detector. It is expressed as

$$Acc = \frac{N_{det}}{N_{gen}}, \quad (5.1)$$

where N_{gen} is the generated D^{*+} particles, N_{det} is the number of D^{*+} where all three daughter particles pass through the sensitive area of the ALICE detector.

Simply put, the reconstruction efficiency represent the ratio of the D^{*+} is reconstructed to the D^{*+} that are accepted. It is caused by both detector properties and artificial selection criteria. It consists of the efficiencies from particle detection, D^{*+} reconstruction, particle track quality selection, particle identification selection, kinematic selection and decay topology selection. The reconstruction efficiency Eff_{rec} is defined as

$$Eff_{rec} = \frac{N_{rec}}{N_{det}}, \quad (5.2)$$

where N_{rec} is the number of reconstructed D^{*+} , which is extracted from the entries in the peak of the D^{*+} invariant mass spectrum.

From the point of the analysis, the acceptance and the reconstruction efficiency both behave as one part of the total efficiency. The term of efficiency ϵ indicates acceptance times reconstruction efficiency $Acc \times Eff_{rec}$, which equals

$$\epsilon = Acc \times Eff_{rec} = \frac{N_{rec}}{N_{gen}}. \quad (5.3)$$

5.2 D^{*+} Corrections

The efficiency is calculated by applying the analysis on results from Monte Carlo simulations of proton-proton collisions. The simulation is performed using PYTHIA [29] with Perugia-0 tune. The propagation of a particle through the detector geometry and the electronic response is simulated with the GEANT3 [57] package. The reconstruction, including event reconstruction, primary and secondary vertex reconstruction, and selections on tracks and decay topology, is applied with the same algorithm as for real data.

The D^{*+} yield is evaluated in nine steps of the D^{*+} reconstruction analysis, starting from the generation of D^{*+} mesons in a limited acceptance in the rapidity range $|y| < 0.5$ to the D^{*+} mesons fulfil the topological and PID selections. The steps where the D^{*+} yield is evaluated in the reconstruction are listed in the following:

Generated Limited is the step where the D^{*+} (or D^{*-}) is fragmented from a c (or \bar{c}) quark. The yield is evaluated that the D^{*+} mesons are in the limited rapidity range $|y| < 0.5$. The generated events are in the range of $|y| < 2$, which is safely covering the rapidity acceptance. In order to provide a corrected result in a rapidity unit centered at $|y| = 0$, we use a limited D^{*+} yield for correction.

Generated in Acceptance is the step where all three generated daughter particles from the $D^{*+} \rightarrow K^- \pi^+ \pi_s^+$ decay pass through the acceptance of the central barrel sub-detectors, which is $|\eta| < 0.8$ and $p_T > 0.1$ GeV/c for K, π particles from D^0 decays, and $|\eta| < 0.8$ and $p_T > 0.05$ GeV/c for the soft pions from D^{*+} decays. In the event simulation, all the daughter particles of one D^{*+} are required to have induced signals in the detector.

Generated Vertex step is where the event with the D^{*+} candidate has a generated primary vertex which is in a reconstructible range along the z -axis.

Generated Refit step is where the generated D^0 daughter particles K, π are successfully reconstructed in the third iteration of the track reconstruction procedure with ALICE central barrel sub-detectors.

Reconstructed is the step where the D^{*+} is reconstructed and all its daughter tracks have passed the pre-selections.

Reconstructed in Acceptance is the step where the reconstructed daughter tracks are in the acceptance.

ITS Clusters Request is the step where the tracks from D^0 decays has a minimum of 5 ITS clusters (max. 6), and at least 1 cluster in the SPD (max. 2).

Topological Selections is the step where the reconstructed D^{*+} passes the topological selections that is the same as described in the analysis with data.

Reconstructed with PID step is where the reconstructed tracks from D^0 decays pass the TPC and TOF PID selections. The selection method is the same as described in the analysis with data.

The D^{*+} efficiency at each step with respect to the first step is shown in Fig. 5.1. The effect of each selection step on the D^{*+} efficiency is demonstrated. Among these steps, the track pre-selections and the

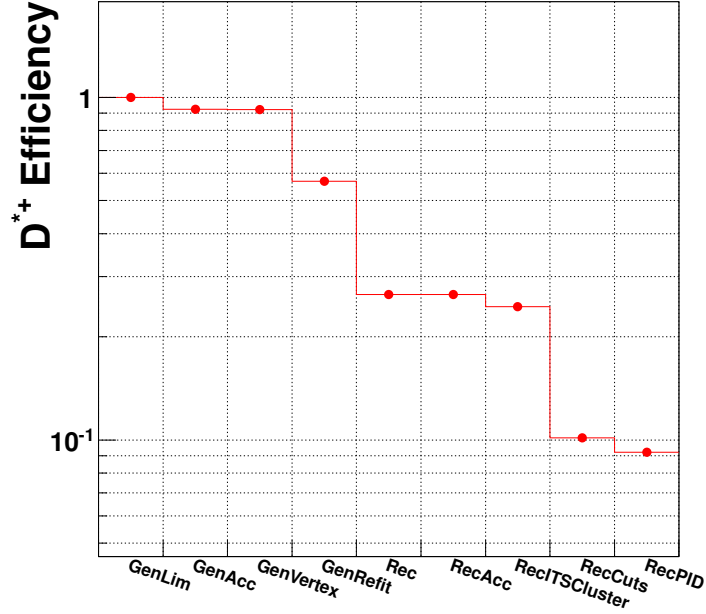


Figure 5.1: Relative D^{*+} yield as each step in the reconstruction procedure. The yield is normalized to the Generated D^{*+} yield in the limited rapidity range $|y| < 0.5$.

topological selections account for most of the signal loss. The integrated efficiency at the final step is $\sim 9\%$.

The acceptance is extracted between the step of *Generated in Acceptance* and *Generated Limited*. The reconstruction efficiency is extracted between the step of *Reconstructed with PID* and *Generated in Acceptance*. The product of acceptance and efficiency is extracted between *Reconstructed with PID* and *Generated Limited*. They are shown in Eq. 5.4.

$$\begin{aligned}
 Acc|_{p_T, \eta} &= \frac{\text{Yield}(\text{Generated in Acceptance})|_{p_T, \eta}}{\text{Yield}(\text{Generated limited})|_{p_T, \eta}}, \\
 Eff|_{p_T, \eta} &= \frac{\text{Yield}(\text{Reconstructed with PID})|_{p_T, \eta}}{\text{Yield}(\text{Generated in Acceptance})|_{p_T, \eta}}, \\
 \epsilon|_{p_T, \eta} &= \frac{\text{Yield}(\text{Reconstructed with PID})|_{p_T, \eta}}{\text{Yield}(\text{Generated limited})|_{p_T, \eta}}, \tag{5.4}
 \end{aligned}$$

Hence, the reconstruction efficiency here in this analysis is the ratio between reconstructed D^{*+} after topological selections, quality selections and

PID selection to the generated D^{*+} in ALICE central barrel acceptance. It can be further unfolded into the detector efficiency and the selection efficiency. The ratio of *Reconstructed in Acceptance* to *Generated in Acceptance* is the efficiency from the detector effect. The ratio of *Reconstructed with PID* to *Reconstructed in Acceptance* is the efficiency from the selection in the D^{*+} reconstruction algorithm. The reconstruction efficiency as functions of p_T and y are shown in Fig. 5.2.

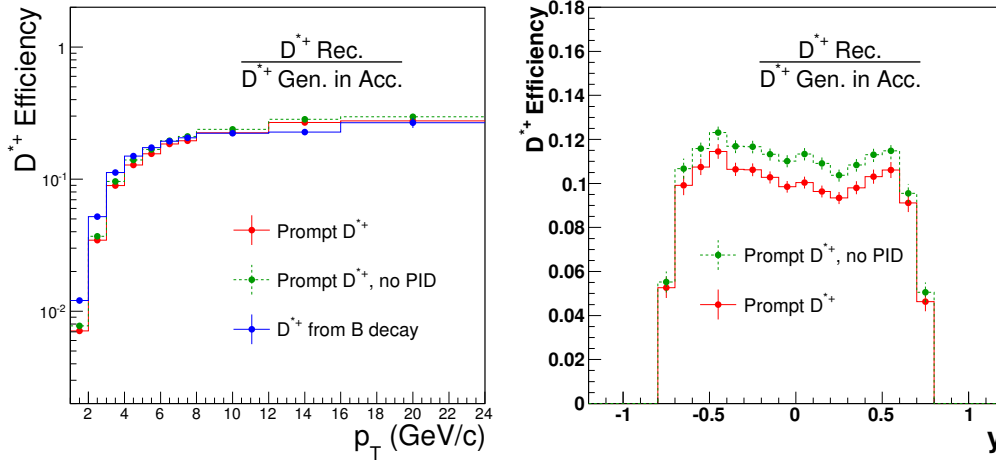


Figure 5.2: D^{*+} reconstruction efficiency as functions of p_T (left) and y (right). The efficiencies of prompt D^{*+} and D^{*+} from decay of b-hadrons are shown separately. The prompt D^{*+} efficiency without PID is also shown as a control of PID quality.

The D^{*+} reconstruction efficiency is increasing as a function of p_T . It is due to the different selections applied in each p_T bin. At low p_T , where the selections are stronger, the efficiency is from below 1% to a few percent. For D^{*+} at $p_T \sim 10$ GeV/c, the efficiency is about $\sim 20\%$ and the increase slows down. The efficiency is in favor of D^{*+} at high p_T . This is because that the selection of the impact parameter product $d_0^K \times d_0^\pi$ is in favor of D^0 with longer decay length. Thus, the high p_T D^{*+} mesons, most of which have long D^0 decay length, have higher efficiency than the low p_T D^{*+} mesons.

The difference between the efficiencies with and without PID selections is constant, proving that the PID efficiency is nearly $\sim 90\%$. The difference between the prompt D^{*+} efficiency and D^{*+} from B feed-down efficiency is significant at low p_T , where the latter one is larger. This is due to the large flight length of B mesons, compared to that of D mesons, is favoured by the impact parameter selections on the decay daughters. At high p_T , where the

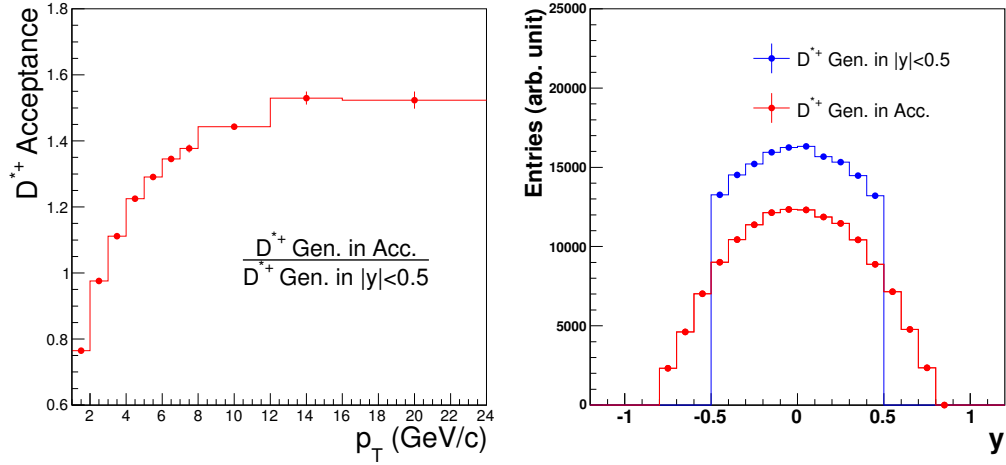


Figure 5.3: Left: the detector acceptance of D^{*+} mesons as a function of p_T . The acceptance is normalized with respect to the generated D^{*+} in the rapidity range $|y| < 0.5$. Right: the rapidity distributions of the generated D^{*+} mesons in the limited rapidity range $|y| < 0.5$ and the generated D^{*+} mesons in the detector acceptance.

selection is much looser, this effect is smaller, thus the efficiencies of the two are similar.

The D^{*+} reconstruction efficiency as a function of y has a plateau in the range $|y| < 0.6$, and drops at the edges. This is because for D^{*+} mesons at the rapidity edge, some of their daughter particles may fall out of the detector acceptance.

The D^{*+} acceptance is shown in the left plot in Fig. 5.3. The efficiency is increasing as a function of p_T . The main reason is that the low p_T D^{*+} mesons have large opening angle between daughters. This may lead to that some daughters fall out of the detector acceptance. It is worth noting that at high p_T the acceptance exceeds 1. This is because that the D^{*+} in acceptance is not a subset of the D^{*+} generated. The generated D^{*+} mesons are limited in the range $|y| < 0.5$. This normalized range in rapidity is where we want to measure the differential cross section. This is confirmed by the right plot in Fig. 5.3, where both distributions of the D^{*+} generated in $|y| < 0.5$ and the D^{*+} in acceptance are shown.

The total efficiency ϵ is shown in Fig. 5.4. Both the efficiencies of prompt D^{*+} and D^{*+} from B mesons decay are shown. The prompt D^{*+} efficiency is $\sim 0.5\%$ at the lowest p_T bin and $\sim 40\%$ at the highest p_T bin.

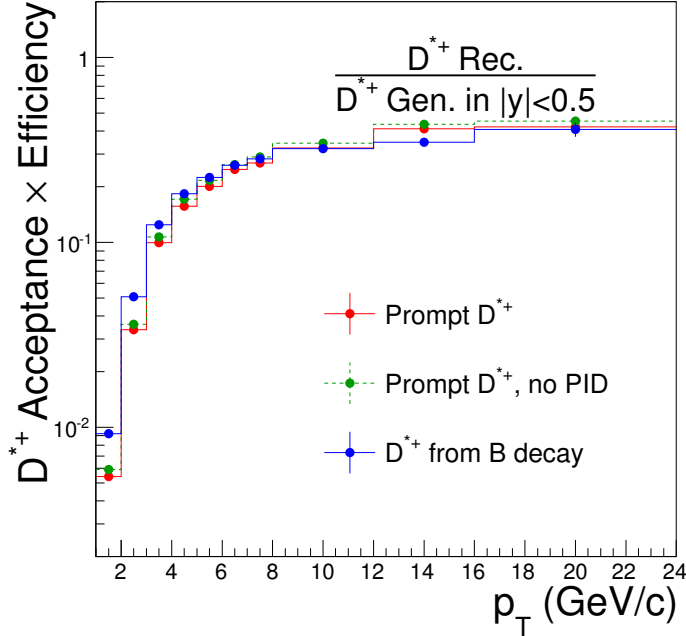


Figure 5.4: The product of acceptance and efficiency of D^{*+} reconstruction as a function of p_T (left). The efficiencies of prompt D^{*+} and D^{*+} from decay of b-hadrons are shown separately. The prompt D^{*+} efficiency without PID is also shown as a control of PID quality.

5.3 B Feed-down Correction

At LHC collision energies, $b - \bar{b}$ quark pair production is not negligible compared to the charm cross section. Figure 5.5 shows various modes of B meson decays to D mesons. The branching ratio of $B^\pm/B^0/B_s^0/b - baryon$ admixture decay to D^{*+} is $(17.3 \pm 2.0)\%$ [7]. As pointed out in Table. 5.1, all B hadrons produced at mid-rapidity is about 6.5% of all D hadrons produced for 14 TeV p-p collisions.

This charm production from B feed-down is due to the process of weak decay. Apart from the charm production in the hard process from the collisions, this feed-down source should be moved out in order to calculate the charm cross section.

N_b method

One method for the correction of B feed-down is feed-down subtraction, called the N_b method. The corrected differential spectrum is

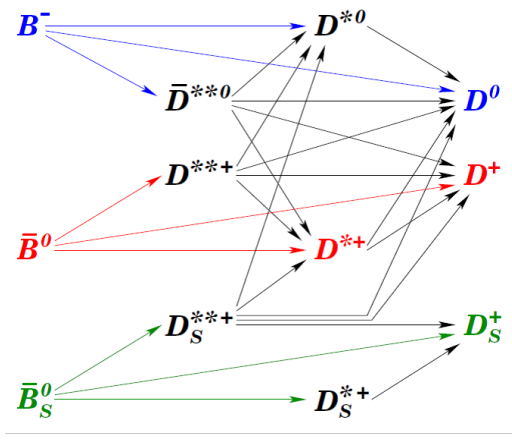


Figure 5.5: B mesons as D meson source.[64]

Particle	Yield	$\langle dN/dy \rangle_{ y _{ab} < 1}$
$D^0 + \bar{D}^0$	0.1908	0.0196
$D^+ + D^-$	0.0587	0.0058
$D_s^+ + D_s^-$	0.0362	0.0038
$\Lambda_c^+ + \bar{\Lambda}_c^-$	0.0223	0.0026
$B^0 + \bar{B}^0$	0.00577	0.00084
$B^+ + B^-$	0.00576	0.00083
$B_s^0 + \bar{B}_s^0$	0.00168	0.00025
$\Lambda_b^0 + \bar{\Lambda}_b^0$	0.00106	0.00016

 Table 5.1: Total yield, average rapidity density for $|y| < 1$, for hadrons with charm and beauty from PYTHIA simulations in p-p collisions at $\sqrt{s} = 14$ TeV [30].

$$\begin{aligned}
 \frac{1}{\epsilon_{c \rightarrow D}} \cdot \left(\frac{dN_D^{raw}}{dydp_T} - N_b \right) &= \frac{1}{\epsilon_{c \rightarrow D}} \cdot \left(\frac{dN_D^{raw}}{dydp_T} - \frac{dN_{B \rightarrow D}^{raw}}{dydp_T} \right), \\
 N_b &= L_{int} \cdot \Delta y \cdot \epsilon_{trigger} \cdot B.R._b \cdot \epsilon_{B \rightarrow D} \cdot \frac{d\sigma_{B \rightarrow D}^{real}}{dydp_T}. \quad (5.5)
 \end{aligned}$$

N_b is the subtracted B feed-down raw counts, which is derived from the FONLL cross section calculation $\frac{d\sigma_{B \rightarrow D}^{real}}{dydp_T}$. In Eq. 5.5, L_{int} is the integrated luminosity, $\epsilon_{trigger}$ is the trigger efficiency, $\epsilon_{B \rightarrow D}$ is the B feed-down efficiency. The derivation between the cross section and the raw counts is further discussed in Chapter. 7, see Eq. ???.

This method is independent from the theory calculation of charm cross section. But it leads to higher uncertainty due to introducing the luminosity, trigger efficiency, compared to the other f_c method.

f_c method

Another method of correcting the B feed-down is evaluated by a factor f_c , which is the ratio between measured D^{*+} from c quark and all measurable D^{*+} . The factor f_c is calculated by the following formula:

$$f_c(p_T, y) = \frac{1}{1 + \frac{\epsilon_{B \rightarrow D}}{\epsilon_{c \rightarrow D}} \cdot \frac{\frac{dN_{B \rightarrow D}^{real}}{dy dp_T}}{\frac{dN_{c \rightarrow D}^{real}}{dy dp_T}}}, \quad (5.6)$$

where the yields $\frac{dN_{B \rightarrow D}^{real}}{dy dp_T}$ and $\frac{dN_{c \rightarrow D}^{real}}{dy dp_T}$ are from FONLL calculations, and the efficiencies $\epsilon_{B \rightarrow D}$ and $\epsilon_{c \rightarrow D}$ are from the correction framework on PYTHIA simulations.

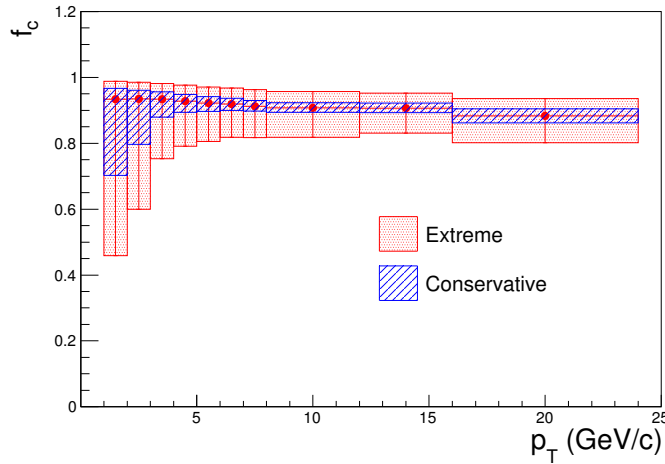


Figure 5.6: B feed-down correction factor f_c for D^{*+} , as a function of p_T . The prompt and non-prompt D^{*+} are from FONLL calculations, and the efficiencies are from PYTHIA simulation, as shown in Fig. 5.2. The uncertainty is from the FONLL calculation.

Figure 5.6 shows the distribution of the B feed-down correction factor, as a function of p_T . One observes that the fraction of reconstructed prompt D^{*+} is more than 90%, and a little higher at low p_T region. The B feed-down effect is slightly larger at higher p_T .

This method depends on the theory calculation of cross section on both prompt D^{*+} meson and D^{*+} meson from feed-down, but is only sensitive to the relative ratio. The uncertainty is mostly from the theory calculation. The extreme uncertainty is obtained while assuming no correlation between the FONLL uncertainties of prompt D^{*+} and D^{*+} from feed-down. The conservative uncertainty is calculated while assuming the uncertainties are fully correlated.

Chapter 6

Systematic Uncertainties

The systematic uncertainty from the analysis is caused by the method of the analysis. There are eight sources of systematic uncertainties considered in this analysis. They are either from the reconstruction or from the correction. Each of them is evaluated by comparing the result with that from a different method.

6.1 Systematics from Reconstruction

Yield extraction The yield extraction of the raw signal has an uncertainty mainly caused by the small statistics of signal in the invariant mass spectrum. The statistic is even smaller if we split the analysis in p_T bins.

Comparing to the statistic uncertainty, the systematic uncertainty from yield extraction is relatively small. In the analysis, the yield is extracted by the integration of the Gaussian fit over the signal peak. In order to estimate the systematics of the yield extraction method, we used the bin counting method for comparison.

The fitting function is, for the signal and background respectively, the sum of a Gaussian function (Eq. 4.6) and a square root times exponential function (Eq. 4.5). In the fitting method, the yield is the integral of the Gaussian within $\pm 3\sigma$ range. In the counting method, the yield is the sum of the bin values within $\pm 3\sigma$ range with the integral of the background subtracted. Figure 6.1 presents this comparison. The fluctuation of the center value of the yield ratio represents the systematic uncertainty, while the error bars represent the statistic uncertainty. The relative systematic uncertainty of the yield extraction is below 10%. The statistic uncertainty is still dominant.

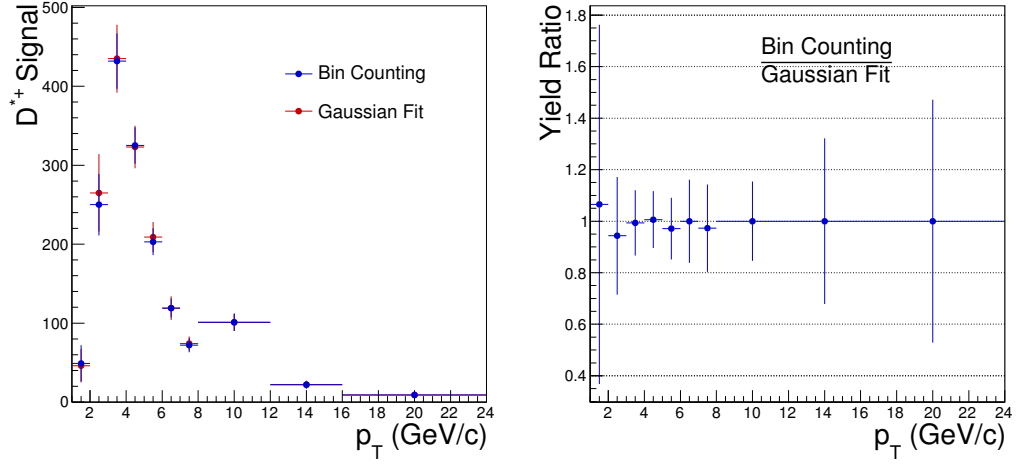


Figure 6.1: Systematics of yield extraction methods. The fitting method is compared with the bin counting method.

PID The inclusion of the particle identification is another source of systematic uncertainty. The efficiency is affected if we introduce the PID method on the track selections. This source of systematics is evaluated by the efficiency of PID selection, defined as the ratio of the yield with PID applied to the yield without PID applied. The difference between the PID efficiency in the data reconstruction and from the simulation represents the systematics introduced by the PID method.

The track selection on PID method from energy loss and time of flight is sensitive to the detector response, and also the selection criteria. The systematics originates from the Gaussian distribution of the energy loss signal and flight time. The center value and the width of the Gaussian rely on the calibration of the detectors. During the operation, the detectors are calibrated at each run period. The distributions of the energy loss and time of flight are well parametrized. Furthermore, the PID selection criteria used in this analysis are chosen to be simple to minimize the systematic effects, which is described in Chap. 4. We select the distribution within $\pm 2\sigma$ in dE/dx and $\pm 3\sigma$ in time of flight. These selection criteria are rather loose, where the probability density is already smaller than 5%, so the effect on the systematics is kept small.

As shown in Fig. 6.2, the yield ratio between with and without PID method is distributed over the expected value. The expected value of the ratio is:

$$R = R_{TPC}^2 R_{TOF}^2 = 0.954^2 \times 0.997^2 = 0.906, \quad (6.1)$$

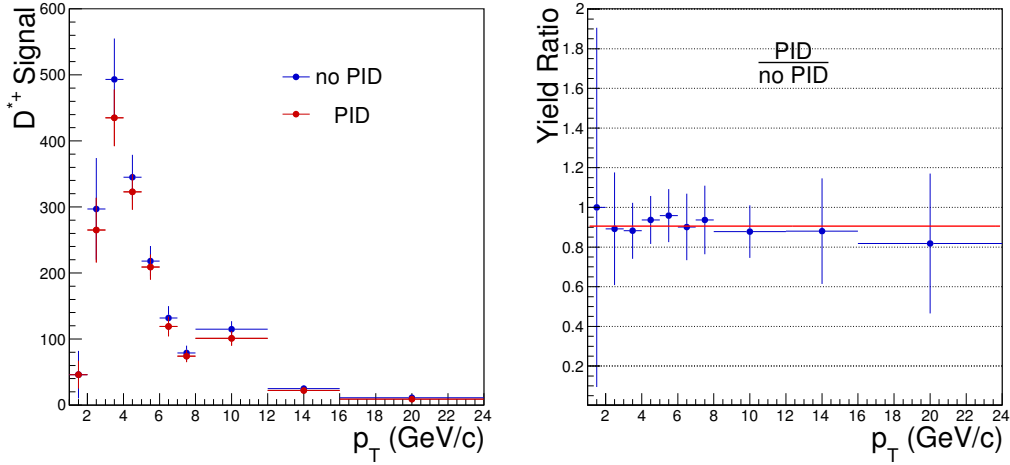


Figure 6.2: Systematics of PID methods. The D^{*+} yield with PID method using TPC $\pm 2\sigma$ and TOF $\pm 3\sigma$ is compared with the yield without applying any PID selection. The ratio of the yield with PID to the yield without PID is drawn in the right plot. The expected value of the ratio is drawn in red.

where, R_{TPC} and R_{TOF} are the expected efficiency from the selection on the Gaussian distribution. The PID selection is applied on the two daughter particles K, π from the D^0 decay, thus the ratio is calculated with power of two. The systematic uncertainty of the PID method is presented by the fluctuation of the center value of the yield ratio, which is found to be below 5%.

Tracking The systematic uncertainty of the tracking efficiency using ITS and TPC in ALICE is studied by varying the track selection criteria. The comparison between the simulation and the data shows a systematic of 8% for the two body $D^0 \rightarrow K^- \pi^+$ decay [19]. The corresponding systematics of a single track efficiency is 4%. However, some soft pions from low p_T D^{*+} decays are only reconstructed by ITS alone. Those tracks, which mainly have $p_T < 150$ MeV/c, will have an additional contribution to systematic uncertainty for the reconstructed D^{*+} in the range of $p_T < 3$ GeV/c. This results a systematic uncertainty of 13% for D^{*+} below 3 GeV/c, and 12% for D^{*+} above 3 GeV/c.

Selection Efficiency The systematic effect becomes significant when the distribution of the cut variables are different between data and simulation. This effect is even more significant if the cut threshold is very tight. To

understand this systematic effect, we apply a modified cut and compare the corrected yields. The result shows that the systematic uncertainty is 22% at $1 < p_T < 2$ GeV/c, and is 10% at $p_T > 2$ GeV/c [19].

6.2 Systematics from Correction

B feed-down Among those D^{*+} mesons reconstructed in the analysis, about 10% are generated from the decay of B mesons, as shown in Fig. 5.6. These D^{*+} mesons from $b \rightarrow D^{*+}$ are subtracted, and what is remaining are prompt D^{*+} mesons from the hadronization of charm. Here the ratio of $\frac{c \rightarrow D^{*+}}{b, c \rightarrow D^{*+}}$ is estimated the pQCD calculations within FONLL. The model has been tested with the bottom production at Tevatron [65] and LHC [66, 67], and it describes the data well. A systematic uncertainty is included by adopting the uncertainty $\frac{c \rightarrow D^{*+}}{b, c \rightarrow D^{*+}}$ ratio from the calculation, the relative uncertainty is shown in Fig. 6.3.

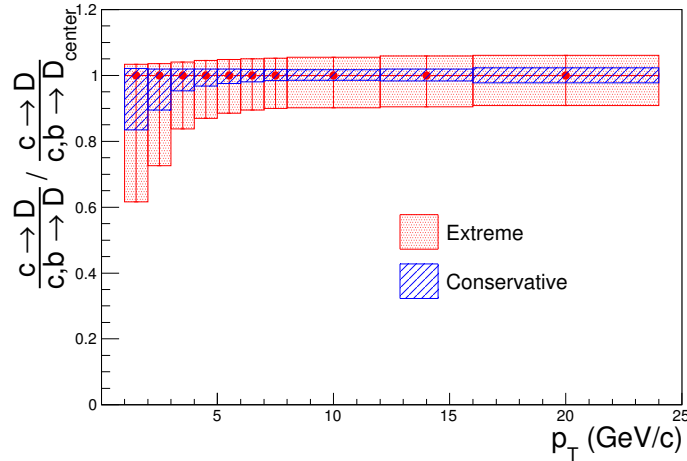


Figure 6.3: The ratio of $\frac{c \rightarrow D^{*+}}{b, c \rightarrow D^{*+}}$ to its center value. The distribution is calculated with FONLL. The error bars represent the systematic uncertainty of the B feed-down calculation.

The systematic uncertainty is determined by varying the parameters of factorization and resummation scales and the mass of the bottom quark. By using the extreme parameters in the calculation with the FONLL model, we determine the minimum and maximum values of the ratio of $\frac{c \rightarrow D^{*+}}{b, c \rightarrow D^{*+}}$ allowed in the FONLL model. The center value is calculated with the parameters at their center values.

The systematic uncertainty is calculated separately for each p_T bin. The uncertainty is larger at low p_T . The large uncertainty at low p_T is from the limit of perturbative calculation at this energy scale.

p_T shape The efficiency used for D^{*+} correction is determined from Monte Carlo simulation with the PYTHIA event generator using the Perugia-0 tune. Its slope in p_T differential cross section is different from that of the FONLL calculation, especially the slope at high p_T . This will lead to a systematic uncertainty in the efficiency, and affect the cross section in the shape of p_T distribution.

This systematic uncertainty due to different p_T shape between simulation and FONLL is estimated from the relative difference between the efficiencies from the two. The difference in the D^{*+} efficiency due to p_T shape is 3% at $1 < p_T < 2$ GeV/ c , and is less than 1% at $p_T > 2$ GeV/ c [19].

Normalization The normalization is based on the integrated luminosity L_{int} . The systematic uncertainty of the normalization is from the determination of the integrated luminosity. As shown in Eq. 3.6, the determination of the integrated luminosity needs a precise measurement of Minimum bias trigger cross section σ_{MB} , which is further determined by the measurement of $\sigma_{V0AND}/\sigma_{MB}$ ratio. This relative factor is measured to be ≈ 0.87 , with uncertainty within 4% over the analyzed data sample.

Branching ratio The branching ration is taken from the Particle Data Book [7]. The branching ratio of $D^0 \rightarrow K^- \pi^+$ decay is $(3.88 \pm 0.05)\%$, and that of $D^{*+} \rightarrow D^0 + \pi_s^+$ decay is $(67.7 \pm 0.5)\%$. The branching ratio of the two decays is $(2.61 \pm 0.04)\%$, where the systematic uncertainty is 1.5%.

6.3 Systematics Summary

The systematic uncertainty is summarized in Tab. 6.1. The total systematics is the quadratic sum of all. The dominant systematics are the B feed-down subtraction, the tracking efficiency and the selection efficiency. The systematics at high p_T are smaller than those at low p_T .

p_T	1-2	2-3	3-4	4-5	5-6	6-7	7-8	8-12	12-16	16-24
Yield	10%			5%						
PID	5%									
Tracking	13%		12%							
Selection	22%	10%								
Feed-down	+3%	+4%	+4%	+4%	+5%	+5%	+5%	+6%	+6%	+6%
	-38%	-27%	-16%	-13%	-11%	-10%	-10%	-10%	-10%	-9%
p_T shape	3%	1%								
Norm.	4%									
B.R.	1.5%									

Table 6.1: Summary of the systematic uncertainties of D^{*+} cross section in the p_T intervals in the range $1 < p_T < 24$ GeV/ c .

Chapter 7

Charm Cross Section

As mentioned in Chap. 2, in order to make a comparison between measurements and theoretical calculations, the result of charm production measurement is presented in two ways. One is the differential charmed meson cross section, the other one is the integrated charm total cross section.

In this Chapter, both the D^{*+} differential cross section and the total charm cross section are shown as the result of this analysis. The measurements are compared with theoretical calculations. The differential and total cross sections of other charmed mesons measured with the ALICE experiment are also presented. Moreover, the production ratios of charmed mesons are calculated. A discussion of the results is given in the end.

7.1 Differential Charmed Meson Cross Section

Comparing to the measurement of total charm cross section, the measurement of differential cross section of a charmed meson is more straight forward and less calculation-involved. Although it raises many difficulties in the theoretical calculations to make a corresponding prediction, such as resummation, fragment function, etc. The comparison between theory and experiment at this level reveals much more information, and helps us understand more about pQCD.

7.1.1 Differential D^{*+} Cross Section

Method of Calculation

The ideal differential cross section of D^{*+} is shown as a distribution in the two-dimensional (p_T, y) phase space, as $\frac{d^2\sigma^{D^{*+}}(p_T, y)}{dydp_T}$. However, the ALICE central barrel sub-detectors limit our measurement in the central rapidity region of the phase space. We present the differential cross section of D^{*+} as a function of p_T , of which the values are integrated over the rapidity range $|y| < y_{max}$. The D^{*+} (D^{*-} not included) cross section is given by the following formular:

$$\frac{d\sigma^{D^{*+}}(p_T)}{dp_T}\Big|_{|y|<0.5} \equiv \frac{1}{2} \frac{1}{\Delta p_T} \frac{f_c(p_T) \cdot N_{reco}^{D^{*+}, D^{*-}}(p_T)}{\epsilon(p_T) \cdot B.R. \cdot \mathcal{L}_{int}}. \quad (7.1)$$

The number $N_{reco}^{D^{*+}, D^{*-}}(p_T)$ is the raw signal yield of both reconstructed D^{*+} and D^{*-} mesons in the mid-rapidity region. The acceptance of D^{*+}, D^{*-} reconstruction with ALICE central sub-detectors is $|y| < 0.8$. The variables $\epsilon(p_T)$ and $f_c(p_T)$ are the efficiency and the feed down correction factor respectively. Both are calculated from PYTHIA simulation, shown in Chap. 5. $B.R.$ stands for the branching ratio of $D^{*+} \rightarrow D^0\pi^+$ and $D^0 \rightarrow K^-\pi^+$ cascade decays. The integrated luminosity is represented by \mathcal{L}_{int} .

The efficiency ϵ composes both the acceptance and the reconstruction efficiency, and ϵ is normalized to the D^{*+}, D^{*-} in the rapidity range $|y| < 0.5$. The feed down correction factor f_c subtracts the measured D^{*+} mesons those originating from B meson decay. Thus, the part of $\frac{f_c(p_T) \cdot N_{reco}^{D^{*+}, D^{*-}}(p_T)}{\epsilon(p_T) \cdot B.R.}$ in Eq. 7.1 is equal to the number of produced prompt D^{*+} and D^{*-} mesons in the rapidity region $|y| < 0.5$.

The corrected yield of D^{*+} and D^{*-} mesons is normalized by the p_T bin width Δp_T . Since we the cross section of only D^{*+} mesons will be given as the result, the D^{*-} is removed by dividing the cross section by 2. Last, the normalized yield is divided by the integrated luminosity \mathcal{L}_{int} . The integrated luminosity is calculated as $\mathcal{L}_{int} = N_{pp}/\sigma_{pp}$, where N_{pp} is the number of proton-proton collisions and σ_{pp} is the minimum-bias trigger cross section of the proton-proton collisions. The calculation of \mathcal{L}_{int} was discussed in Chap. 3.

There are two approximations in the calculation of D^{*+} p_T -differential cross section. They are:

- The calculation assumes that the rapidity distribution of D^{*+} meson cross section in the range $|y| < 0.5$ is flat. The validity of this

assumption is confirmed by the PYTHIA 6.4 [29] and FONLL [3]. These calculations suggest that the D^{*+} cross section are uniform with 1% in this rapidity range. To make a more precise claim, we present our result as a p_T -differential cross section integrated over 1 unit in the rapidity direction ($\frac{d\sigma^{D^{*+}}(p_T)}{dp_T}|_{|y|<0.5}$), instead of a double differential cross section ($\frac{d^2\sigma^{D^{*+}}(p_T,y)}{dydp_T}|_{y=0}$).

- The calculation assumes that, in proton-proton collisions, D^{*+} and D^{*-} mesons are produced equally in the measurable (p_T, y) phase space. In proton-proton high energy collisions, the charm and anti-charm quarks are equally produced. Additionally, the net charge density of the collision system is nearly zero. Thus, there is no preference in the D^{*+} and D^{*-} production procedure, and the assumption is valid. Based on this assumption, the D^{*+} cross section $\sigma^{D^{*+}}$ is calculated as $\frac{1}{2}(\sigma^{D^{*+}} + \sigma^{D^{*-}})$.

Result

The p_T -differential cross section of D^{*+} meson is determined from Eq. 7.1, and the result is shown in Fig. 7.1. The data were collected from LHC proton-proton collisions at 7 TeV in the year 2010. 314 million minimum-bias collision events were analysed. The corresponding integrated luminosity is $\mathcal{L}_{int} = 5 \text{ nb}^{-1}$.

The measurement is applied in the rapidity region $|y| < 0.8$. The result is not shown in divided rapidity bins. First, because this is only a small rapidity coverage in the full rapidity range. Second, the distribution in this region is nearly flat. Last, separation of the data leads to larger statistical uncertainty. Thus, the result is integrated over the rapidity region $|y| < 0.8$, and further normalized into 1 rapidity unit. In the region $1 < p_T < 24 \text{ GeV}/c$, the data are distributed in 10 bins. The coverage is limited at both ends. At the lower edge, the measurement is limited by the minimum p_T threshold of which a particle is detectable. At the higher edge, the measurement is limited by the reconstruction efficiency and the statistics of the collected data.

In Fig. 7.1, the data points are drawn at each bin center. However, the value $d\sigma/dp_T|_{|y|<0.5}$ do not correspond to the value at the p_T bin center. Instead, it represents the integrated and normalized value over the D^{*+} mesons in the range of certain p_T bin. Accordingly, the center of mass value $\langle p_T \rangle$ represents the mean p_T value of the D^{*+} mesons in certain p_T bin. The $\langle p_T \rangle$ for each p_T bin is calculated from the reconstructed D^0 mesons from $D^0 \rightarrow K^-\pi^+$ decay channel. In each p_T bin, the invariant mass is

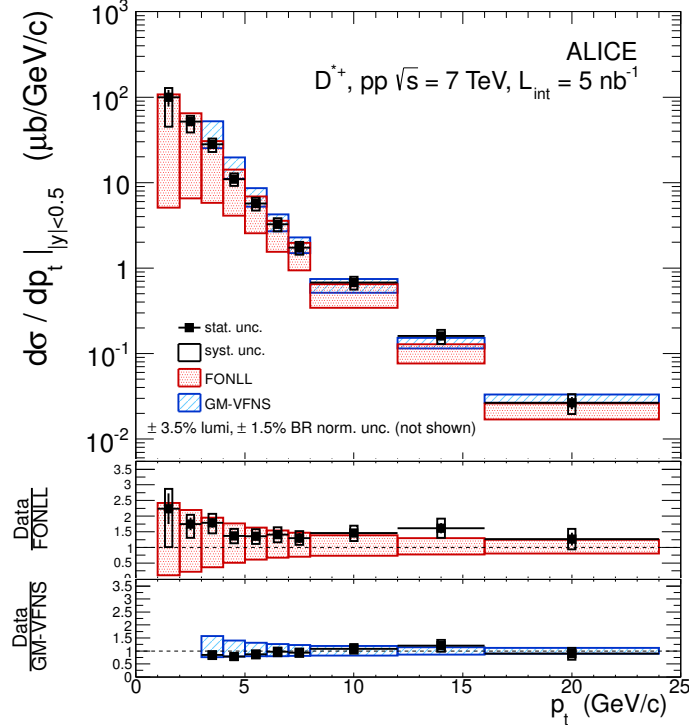


Figure 7.1: D^{*+} p_T differential cross section in proton proton collisions at $\sqrt{s} = 7$ TeV. The result is compared with FONLL (in red) and GM-VFNS (in blue) calculations.

plotted first. The p_T distribution of the entries in the mass peak region is then made. The contribution from combinatorial background is further subtracted by using the entries from two side bands near the mass peak in the invariant mass plot. The $\langle p_T \rangle$ of the residual is calculated. This $\langle p_T \rangle$ values are compatible for D^{*+} meson. The values of $\langle p_T \rangle$ and $d\sigma/dp_T|_{|y|<0.5}$ are shown in Table 7.1.

The data show a clear trend of decreasing D^{*+} cross section as the p_T increases. The systematic uncertainties are larger than statistical uncertainties in every p_T bin. The relative systematic uncertainty is much more significant at low p_T bins, especially in the bin $1 < p_T < 2$ GeV/c. This originates from the correction of B feed-down D^{*+} mesons, where the FNOLL calculation introduces large uncertainty at low p_T . The values of $\langle p_T \rangle$ have larger uncertainties at both low p_T bins and high p_T bins. At the lower edge, it is from the large statistical uncertainty of the combinatorial background. At the higher edge, it is from low statistics of the signal.

The FONLL and GM-VFNS calculations are both presented in Fig. 7.1 in

7.1. Differential Charmed Meson Cross Section

p_T bin (GeV/c)	$\langle p_T \rangle$ (GeV/c)	$\frac{d\sigma(D^{*+})}{dp_T} \Big _{ y <0.5} \pm \text{stat.} \pm \text{syst.}$ ($\mu\text{bc/GeV}$)
1-2	1.5 ± 0.3	99 ± 22 ⁺²⁸ ₋₅₄
2-3	2.5 ± 0.2	51.6 ± 5.9 ^{+8.7} _{-13.1}
3-4	3.5 ± 0.1	27.9 ± 2.3 ^{+4.6} _{-5.2}
4-5	4.5 ± 0.1	10.97 ± 0.87 ^{+1.81} _{-1.88}
5-6	5.5 ± 0.1	5.68 ± 0.45 ^{+0.97} _{-0.99}
6-7	6.5 ± 0.1	3.25 ± 0.27 ^{+0.55} _{-0.56}
7-8	7.4 ± 0.1	1.73 ± 0.21 ^{+0.29} _{-0.30}
8-12	9.4 ± 0.3	0.674 ± 0.050 ^{+0.113} _{-0.116}
12-16	13.8 ± 0.9	0.160 ± 0.016 ^{+0.030} _{-0.031}
16-24	17.0 ^{+2.0} _{-1.0}	0.027 ± 0.004 ^{+0.007} _{-0.007}

Table 7.1: p_T -differential cross sections and mean p_T of D^{*+} meson in each p_T bins. The data are measured by the ALICE experiment in p-p collisions at 7 TeV. The values correspond to the data points in Fig. 7.1. The systematic uncertainties from the normalization and the decay branching ratio are not included.

comparison. Both calculations use CTEQ6.6 parton distribution functions to define the initial conditions. The numeric values of the calculations represent the integrated and normalized values over the ranges of each p_T bin. The result of the calculation is shown as a bracket between an upper and a lower limit. This uncertainty is not the standard deviation, and the uncertainty profile is not Gaussian either. The center value is calculated with an arbitrary parameter, while the upper and lower limits are calculated with extreme values of the parameters. Thus, the center value is not preferred over other values at the edge, and every value inside this bracket is one possibility. The details of the two calculation models were introduced in Chap. 2.

In the FONLL calculation, three sources of uncertainties are considered. They are the uncertainty from the scale variation, uncertainty from the charm quark mass, and the uncertainty of the PDF. The perturbative uncertainty is acquired by varying the factorization and renormalization scales μ_f, μ_r in the range $0.5 < \frac{\mu_f}{m_T}, \frac{\mu_r}{m_T} < 2$ and $0.5 < \frac{\mu_f}{\mu_r} < 2$, where $m_T = \sqrt{p_T^2 + m_c^2}$. The uncertainty from the charm quark mass in the FONLL calculation is obtained by varying the charm quark mass within the range $1.3 < m_c < 1.7$ GeV/ c^2 . The uncertainty of the PDF is also included in FONLL. These uncertainties are calculated separately, with the other parameters fixed at their central values. The total uncertainty is taken as the square root of the quadratic sum $\Delta\sigma_{\text{FONLL}} = \sqrt{\Delta\sigma_{\mu_f, \mu_r}^2 + \Delta\sigma_{m_c}^2 + \Delta\sigma_{\text{PDF}}^2}$.

In contrast, in the GM-VFNS calculation, only the uncertainty from the scale variation is considered. This is for the reason that, in both calculation schemes, the uncertainty from the scale variation is dominant. There are two factorization scales μ_i, μ_f in the GM-VFNS calculation. Both μ_i, μ_f and the renormalization scale μ_r are limited to the range $0.5 < \frac{\mu_i}{m_T}, \frac{\mu_f}{m_T}, \frac{\mu_r}{m_T} < 2$. Moreover, their ratios are limited to the range $0.5 < \frac{\mu_i}{\mu_f}, \frac{\mu_f}{\mu_r}, \frac{\mu_r}{\mu_i} < 2$. The charm quark mass is fixed at $m_c = 1.5 \text{ GeV}/c^2$. The PDF uncertainty is also not included in GM-VFNS.

The ratios between the measurement and the two theories are also shown in Fig. 7.1. The central value of FONLL is calculated with the scale parameters $\mu_f = \mu_r = m_T$ and the charm quark mass $m_c = 1.5 \text{ GeV}/c^2$. Similarly, in GM-VFNS, the central value is calculated with the scale parameters $\mu_i = \mu_f = \mu_r = m_T$.

The comparison between the measurement and the FONLL and GM-VFNS calculations reveals:

- Both FONLL and GM-VFNS calculations are compatible with the measurement within uncertainty. The measured data points are inside the predicted ranges of both calculations, except for a slight difference between data and FONLL in bin $12 < p_T < 16 \text{ GeV}/c$.
- The measured data points are at the lower edge of the GM-VFNS calculation, and are systematically smaller than the central values of GM-VFNS prediction. The two bins in $8 < p_T < 16 \text{ GeV}/c$ are exceptions, which should be due to the relatively large uncertainties compared to the calculations.
- The measured data points are at the higher edge of the FONLL calculation, and are systematically larger than the central values of FONLL prediction.
- In the low- p_T region, the differences between the center values of the calculations and the measurement are relatively larger than the differences in the high- p_T region.
- In the low- p_T region, the uncertainties of the calculations are larger than the uncertainties of the measurement. Whereas, in the high- p_T region, the uncertainties of the measurement are relatively larger, if one considers both the systematic and statistical uncertainties.

The comparisons between the calculations and the measurement result enable us to understand the successes and limits of the current pQCD calculations.

In the low- p_T region of the charm differential cross section, the pQCD calculations agree with the measurements. However, among all the sources of the uncertainties, the perturbative uncertainty is too large. The other calculation uncertainties from the quark mass and the PDF are overshadowed by the perturbative uncertainty. Thus, the comparison is limited by the precision level of current pQCD calculation. A higher order pQCD calculation of charm cross section may reduce the perturbative calculation, and will reveal more information by comparing to the measurements.

In the high- p_T region of the charm differential cross section, the resummation method has much reduced the perturbative uncertainties. The calculations from FONLL and GM-VFNS models give more precise predictions than the measurements from ALICE. However, there is difference between those two calculations. This indicates that, the uncertainty of the resummed pQCD calculations may be underestimated at high- p_T region. Even though, the calculated charmed meson p_T cross sections agree well with the measurement up to 24 GeV/ c .

7.1.2 Differential Cross Sections of Other D Mesons

Differential Cross Sections of D Mesons in p-p Collisions at 7 TeV

Along with the D^{*+} analysis, other charmed baryons are reconstructed and measured with the ALICE experiment. The results found for the D^0 , D^+ and D_S^+ cross sections are shown here for comparison.

Figure 7.2 shows the D^0 and D^+ differential cross section in proton-proton collisions at 7 TeV. The D^0 mesons are reconstructed from the $D^0 \rightarrow K^-\pi^+$ channel ($B.R. = 3.88 \pm 0.05$). The D^+ mesons are reconstructed from the $D^+ \rightarrow K^-\pi^+\pi^+$ channel ($B.R. = 9.4 \pm 0.4$). The mean proper decay length $c\tau$ of the D^0 and D^+ mesons are 123 and 312 μm , respectively. The topological selections and particle identification method are applied on both reconstructions. The reconstructed raw yields are about ~ 8300 and ~ 2800 for D^0 and D^+ mesons. Both analyses are done with the same data sample as shown in Fig. 7.1. Both FONLL and GM-VFNS calculations are presented in comparison to the measurements.

The differential cross section of the D^0 reconstruction is shown in the region $1 < p_T < 16$ GeV/ c . The last bin $16 < p_T < 24$ GeV/ c is not available due to the limited signal to background ratio. On the other hand, the differential cross section of the D^+ reconstruction is shown in the region $1 < p_T < 24$ GeV/ c , which is the same as that of the D^{*+} analysis.

For both analyses, The comparisons between the measurements and the calculations give a same conclusion as given by the D^{*+} analysis. We

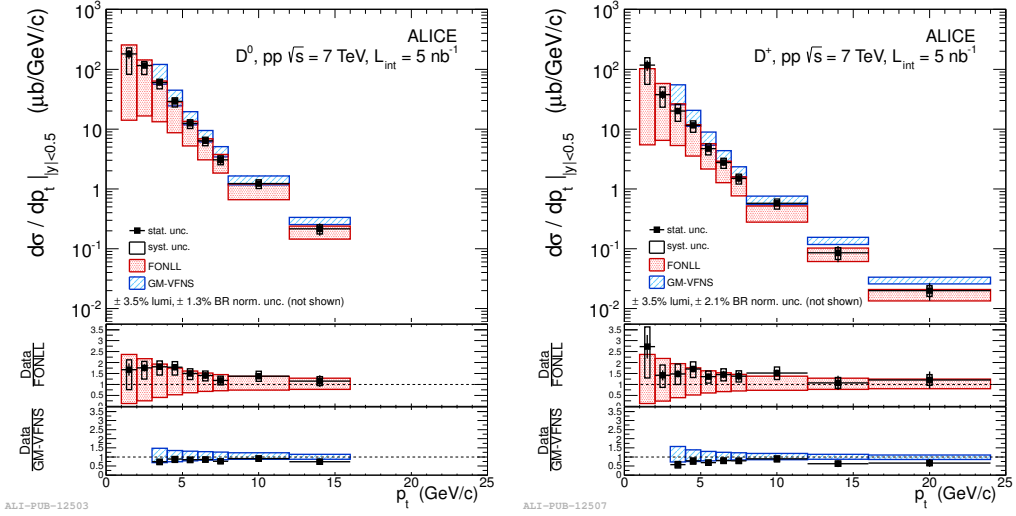


Figure 7.2: D^0 and D^+ p_T differential cross section in proton proton collisions at $\sqrt{s} = 7$ TeV [19]. The result is compared with FONLL (in red) and GM-VFNS (in blue) calculations.

found that the first bin of the measured D^+ cross section is above the theoretic value, and also has large systematic uncertainty. Except for that, the calculations have good agreement with the measurement, also the FONLL (GM-VFNS) is systematically below (above) the measurement. The remaining issue of the comparison is that the theoretical uncertainties are too large. The results from the D^{*+} , D^0 and D^+ analyses are also consistent with the p_T -differential cross sections of the D mesons measured in 7 TeV proton-proton collisions with the ATLAS experiment [68].

Figure 7.3 shows the D_S^+ differential cross section in proton-proton collisions at 7 TeV. The D^0 mesons are reconstructed from the $D_S^+ \rightarrow \phi\pi^+$ and $\phi \rightarrow K^-K^+$ cascade channels ($B.R. = 2.28 \pm 0.12$). The mean proper decay length of the D_S^+ is $c\tau = 150 \pm 2\mu\text{m}$. The data were collected in 2010. They are from the same period as been used in D^{*+} , D^0 and D^+ analyses. There are about ~ 480 D_S^+ mesons are reconstructed. The measured differential cross section is given in the range $2 < p_T < 12$ GeV/c, and divided into 4 p_T bins. The rapidity range is $|y| < 0.5$.

The k_T factorization at LO and GM-VFNS calculations are shown as the comparisons of the measurement. The D_S^+ cross section from FONLL calculation is not available. This is because that the D_S^+ fragmentation function is currently unavailable in the FONLL framework. The GM-VFNS calculation has good agreement with the measurement. However, the k_T factorization are systematically below the measurement. Nevertheless, its

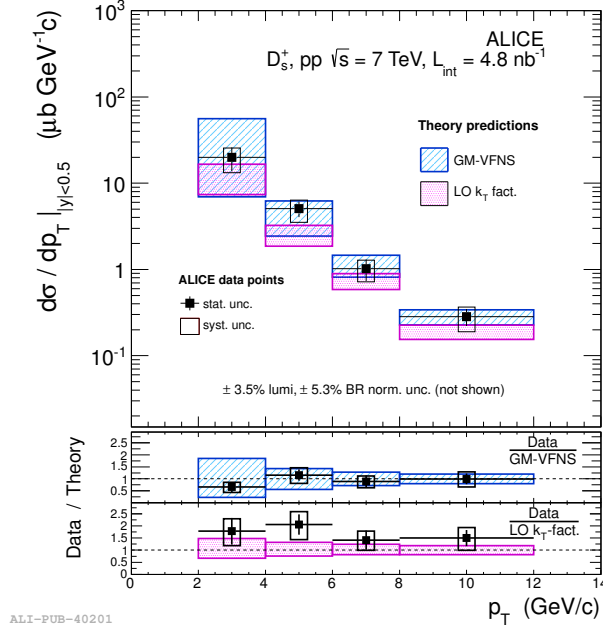


Figure 7.3: D_S^+ p_T differential cross section in proton proton collisions at $\sqrt{s} = 7$ TeV. The result is compared with k_T factorization at LO [69] (in magenta) and GM-VFNS (in blue) calculations [70].

upper limit are covered in the lower part of uncertainties range of the measurement. Further conclusions are hard to be addressed based on the limited data points given by the measurement.

Differential Cross Sections of D Mesons in p-p Collisions at 2.76 TeV

In order to calculate the charm nuclear modification factor in the Pb-Pb collisions, the cross sections of D mesons in proton-proton collisions at 2.76 TeV is needed as the baseline. A short run of proton-proton collisions at $\sqrt{s} = 2.76$ TeV was carried out. But the statistics is limited and does not allow a comparison with the Pb-Pb measurements for every p_T bins. Thus, the p-p baseline is achieved by scale down the cross section measured at 7 TeV collisions. The scaling factor is from the FONLL calculation, taking the ratio of the cross section at 2.76 TeV to the cross section at 7 TeV. The 2.76 TeV measurement and the scaled cross section provide us more understandings on the pQCD calculations.

The p_T differential cross sections of D^0 , D^+ and D^{*+} at 2.76 TeV are shown in Fig. 7.4. The detector setting, trigger setting and analysis method

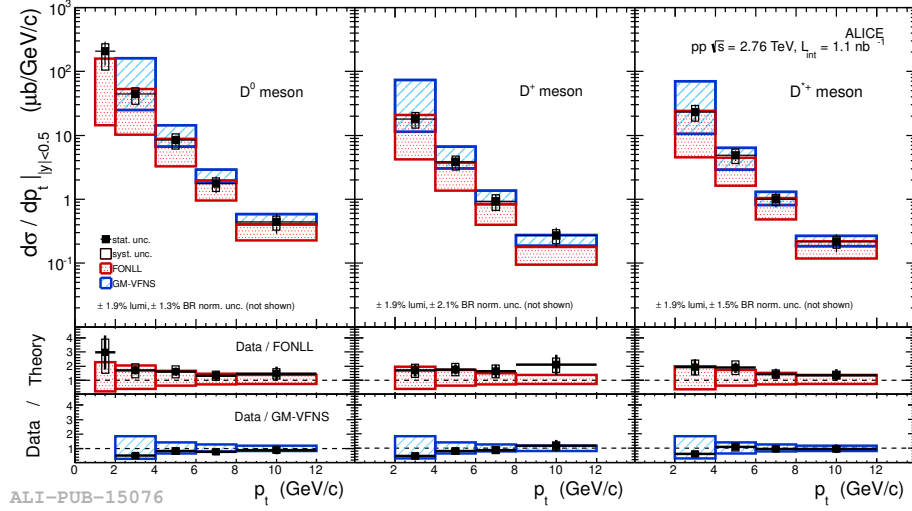


Figure 7.4: D^0 , D^+ and D^{*+} p_T differential cross section in proton proton collisions at $\sqrt{s} = 2.76$ TeV. The result is compared with FONLL (in red) and GM-VFNS (in blue) calculations [20].

are the same as been used in the 7 TeV measurement. The number of collision events is 58M, which corresponds to an integrated luminosity $L_{int} = 1.1 \text{ nb}^{-1}$. The D_s^+ meson can not be reconstructed with this small amount of data, due to its relatively low production rate and reconstruction efficiency. The measured differential cross sections are available in a smaller p_T range $2 < p_T < 12 \text{ GeV}/c$, where an additional data point $1 < p_T < 2 \text{ GeV}/c$ is provided in the D^0 measurement. The result is in a smaller p_T phase space than that from the 7 TeV measurements due to the limited statistics.

The measured differential cross sections are also compared with FONLL and GM-VFNS calculations. The conclusion given by the comparison is the same as that from 7 TeV measurement. Except for the D^+ cross section at bin $8 < p_T < 12 \text{ GeV}/c$, the theory calculations and the measurements are in good agreement. The data points are systematically higher than the central value of the FONLL calculation, and lie on the upper edge of the uncertainty bracket. On the other hand, the data points are lower than the GM-VFNS central values.

The comparisons of the 2.76 TeV cross section to the 2.76 TeV cross section scaling are shown in Fig. 7.5. The scaling factor is evaluated with the center value of the FONLL calculation at both 2.76 TeV and 7 TeV. The uncertainty is estimated with the variation of the parameters. We found agreement in every p_T bin. These agreements suggest that the shape of the D mesons cross section distributions are well reproduced by FONLL

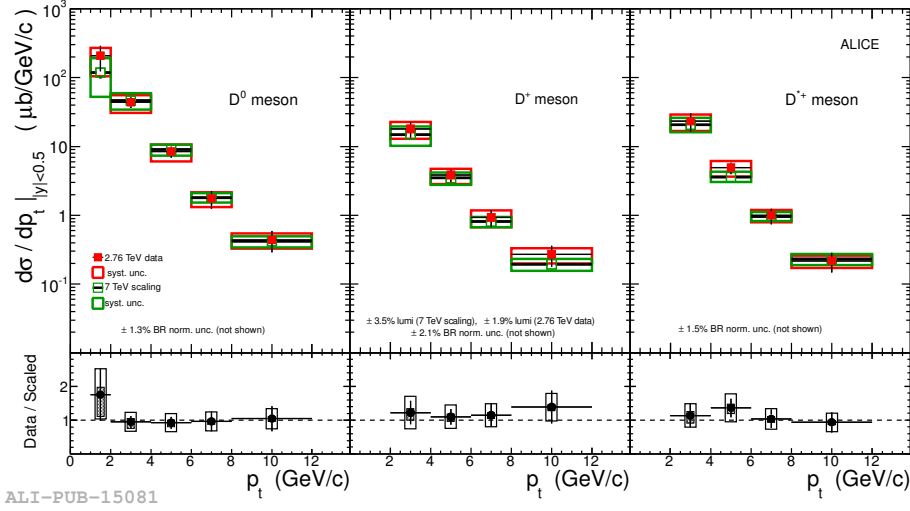


Figure 7.5: D^0 , D^+ and D^{*+} p_T differential cross section in proton proton collisions at $\sqrt{s} = 2.76$ TeV, compared with the scaling of the cross sections at $\sqrt{s} = 7$ TeV. The ratio of the 2.76 TeV cross section to the 7 TeV scaling is shown in the bottom [20].

calculations.

7.1.3 D Mesons Ratios

The ratios of D^+/D^0 , D^{*+}/D^0 , D_s^+/D^0 and D_s^+/D^+ in 7 TeV p-p collisions are shown in Fig. 7.6. There are systematic uncertainties, which are considered in both measurements of the two mesons taking the ratio. These correlated uncertainties between two D meson measurements are treated separately. The systematic uncertainty from the B feed-down is estimated from the spread of the cross section ratios. The systematic uncertainty from the tracking efficiency is cancelled between three-body decay channels. The error is estimated to be 4% when the ratio of the cross section of a three-body-decaying meson and a two-body-decaying meson is calculated.

The predictions from FONLL, GM-VFNS and PYTHIA are shown as comparisons with the measurement. The prediction of the D_s^+ cross section from FONLL is not available, due to the absence of a proper fragmentation function. Those predictions are made in the rapidity range $|y| < 0.5$. In PYTHIA, the tune of Perugia-0 for charm hadronization is applied.

The ratios from the FONLL and GM-VFNS models are calculated by assuming a correlation of perturbative uncertainty between the D mesons. When the ratio is calculated, the same scale parameters are applied to

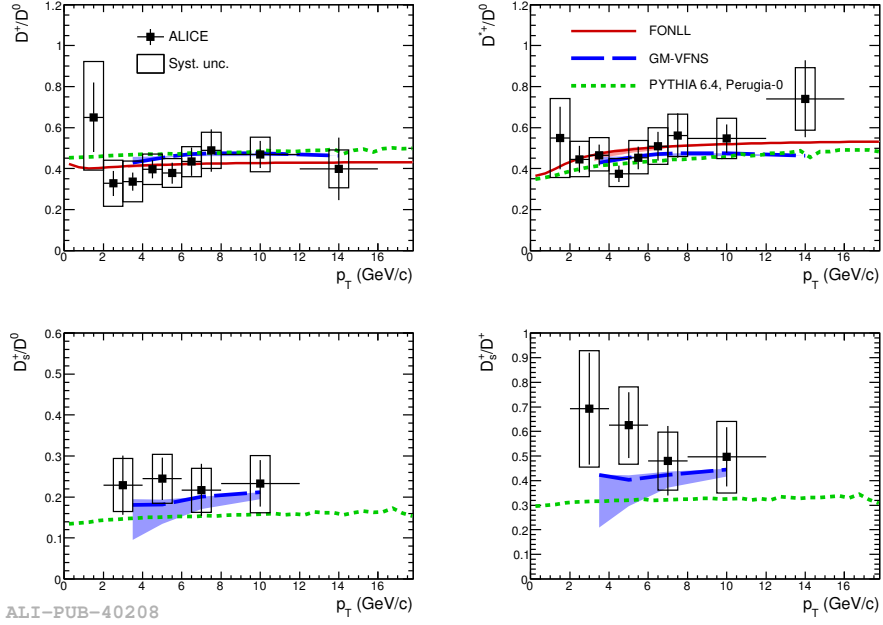


Figure 7.6: The ratios between the D mesons as a function of p_T in pp collisions at $\sqrt{s} = 7$ TeV. The result is compared with FONLL (in red), GM-VFNS (in blue) and PYTHIA 6.4.21 with Perugia-0 tune [20].

the calculations of both D mesons. Thus the uncertainties from the scale variation cancel to large extent. The prediction of the D^+/D^0 and D^{*+}/D^0 ratios from FONLL and GM-VFNS models agree with the data within uncertainties. The meson ratios predicted by FONLL and GM-VFNS come from their fragmentation functions. Those fragmentation functions are fitted to existing measurements, and are not from perturbative calculations. This agreement exhibits the consistency of the D meson fragmentation among experiments in different collision systems. Fig. 7.6 also shows that the ratios of D_s^+/D^0 and D_s^+/D^+ are slightly above the prediction from GM-VFNS and PYTHIA. We note that the uncertainties of these two ratios are relatively large, which mainly originate from the D_s^+ measurement. Within the large uncertainty, we observe that the ratios between strange D mesons and non-strange D mesons have little dependence on p_T . An analysis with higher statistics will enable us to give a stronger conclusion.

7.2 Total Cross Sections of D Mesons

Comparing to the differential cross section of charm mesons, the total charm cross section is a more intrinsic quantity. It is less related to experimental circumstances, and is relatively easy to calculated with pQCD. But the measurement of the total charm cross section needs to involve the either calculations or simulations, which may raise the systematic uncertainty.

In order to measure the total charm cross section, we have to integrate the measured differential cross section in the visible range of (p_T, y) phase space. Then the result is extrapolated to the whole phase space.

The visible cross section is defined as the integral of the differential cross section in the measured region of phase space. The total cross section is the integral of the extrapolated differential cross section over the full phase space. The extrapolation method in the phase space is based on the FONLL calculation.

7.2.1 Visible Cross Sections of D Mesons

In the case of this analysis, the measured D^{*+} differential cross section is provided in the range $|y| < 0.5$ and $1 < p_T < 24$ GeV/ c . This range is limited by the acceptance of the detector, the statistics of the data and the reconstruction efficiency. The visible D^{*+} cross section measured by the ALICE experiment is calculated as the following:

$$\begin{aligned}\sigma_{vis.}^{D^{*+}} &= \int_{y=-0.5}^{y=0.5} \int_{p_T=1\text{GeV}/c}^{p_T=24\text{GeV}/c} \frac{d^2\sigma_{\text{ALICE}}^{D^{*+}}(p_T, y)}{dydp_T} dy dp_T \\ &= \int_{p_T=1\text{GeV}/c}^{p_T=24\text{GeV}/c} \frac{d\sigma_{\text{ALICE}}^{D^{*+}}(p_T)|_{|y|<0.5}}{dp_T} dp_T.\end{aligned}\quad (7.2)$$

In Eq. 7.2, $\frac{d\sigma_{\text{ALICE}}^{D^{*+}}(p_T)|_{|y|<0.5}}{dp_T}$ is the p_T -differential cross section we have shown in Sec. 7.1. The integral is simply the sum of the differential cross sections over all p_T bins. The visible cross sections of the other D mesons are calculated in the same way. They are measured in the same rapidity range $|y| < 0.5$, and in the p_T ranges where the measurements are performed. The visible cross sections of D^{*+} and the other D mesons measured with the ALICE central rapidity detectors are summarized in Table 7.2.

7.2.2 Method of Extrapolation

The extrapolation is performed by multiplying the visible cross section by an extrapolation factor f_{FONLL} . The extrapolation factor is determined by the

Meson	\sqrt{s} (TeV)	p_T (GeV/c)	$\sigma_{vis.}^D \pm \text{stat.} \pm \text{syst.}$ (μb)
D^0	7	1-16	412 ± 33 $^{+55}_{-140}$
D^+	7	1-24	198 ± 24 $^{+42}_{-73}$
D^{*+}	7	1-24	203 ± 23 $^{+30}_{-67}$
D_s^+	7	2-12	53 ± 12 $^{+13}_{-15}$
D^0	2.76	1-12	317 ± 85 $^{+72}_{-120}$
D^+	2.76	2-12	47 ± 9 $^{+10}_{-12}$
D^{*+}	2.76	2-12	59 ± 14 $^{+13}_{-14}$

Table 7.2: Summary of the visible cross sections of the D mesons measured by the ALICE experiment in p-p collisions at 7 TeV and 2.76 TeV. The visible cross sections are in the rapidity range $|y| < 0.5$. The systematic uncertainties from the normalization and the decay branching ratio are not included.

ratio of the theoretical total cross section in the full range of (p_T, y) phase space to the theoretical cross section in the visible phase space. The subscript tells that the extrapolation factor is extracted from the FONLL calculations. In the case of the D^{*+} analysis, its total cross section is calculated as the following:

$$\sigma_{tot}^{D^{*+}} = \sigma_{vis.}^{D^{*+}} \cdot f_{\text{FONLL}}, \quad (7.3)$$

$$f_{\text{FONLL}} = \frac{\int_{y=-\infty}^{y=\infty} \int_{p_T=0}^{p_T=\infty} \frac{d^2 \sigma_{\text{FONLL}}^{D^{*+}}(p_T, y)}{dy dp_T} dy dp_T}{\int_{y=-0.5}^{y=0.5} \int_{p_T=1 \text{ GeV}/c}^{p_T=24 \text{ GeV}/c} \frac{d^2 \sigma_{\text{FONLL}}^{D^{*+}}(p_T, y)}{dy dp_T} dy dp_T}. \quad (7.4)$$

Our knowledge of the D meson hadro-production cross section is limited in the small phase space. For that reason, the extrapolation must rely on the theory calculations. FONLL is a good candidate for this extrapolation, for the reasons listed below:

- Compared with standard NLO calculations, FONLL has a good accuracy in the high- p_T region. The resummation of the logarithmic terms enables FONLL to give a precise prediction of the differential cross section in the high- p_T region. Due to the limited statistics, the measurement is absent at $p_T > 24$ GeV/c, where FONLL gives a very good estimate of the cross section.
- FONLL calculations have a reasonably small uncertainty in the low- p_T region. The cross section decreases logarithmically as a function of p_T . Thus, the integrated total cross section is dominated by the

contribution from the low- p_T region. The extrapolation uncertainty of the total cross section is also dominated by the uncertainty in this region. The FONLL calculation applies a suppression function $G(m, p_T)$ in order to suppress the zero mass resummation in the low- p_T region. This merit significantly reduces the uncertainty of the FONLL calculation in the low- p_T region, whereas other theoretical models with zero mass resummation calculation, e.g. GM-VFNS, do not have precise predictions at $p_T \sim 1$ GeV/ c or lower.

- FONLL has good agreement with data in the visible range of phase space. Although the measured data points are systematically above the central value from the FONLL calculations, the shape of the measured distribution is well reproduced by FONLL. Considering that the extrapolation factor f_{FONLL} is only the ratio of the FONLL cross section in two different regions, the absolute value of the FONLL calculation does not affect the extrapolated result.

The extrapolation factor f_{FONLL} is calculated using the central value of the FONLL calculation. It also has a non-negligible uncertainty, since the FONLL prediction of the differential cross section has large uncertainties. Three sources of the uncertainties are considered. They are the uncertainty from the scales μ_f, μ_r , the uncertainty from the charm mass m_c , and the uncertainty from the parton distribution function PDF. We vary each parameter independently, while keeping the other parameters fixed at their central values. The upper and lower uncertainties are calculated separately, hence the uncertainty is asymmetric. Take the scale uncertainty as an instance, the maximum and minimum values of the extrapolation factor are $f_{\mu_f, \mu_r}^{\text{MAX}} = \text{FONLL}_{\mu_f, \mu_r}^{\text{MAX}} / \text{FONLL}_{\mu_f, \mu_r}^{\text{MIN}}$ and $f_{\mu_f, \mu_r}^{\text{MIN}} = \text{FONLL}_{\mu_f, \mu_r}^{\text{MIN}} / \text{FONLL}_{\mu_f, \mu_r}^{\text{MAX}}$. The upper (lower) uncertainty is the difference between the maximum (minimum) value and the center value f_{FONLL} . The total uncertainties of the extrapolation factor is then taken as the square root of the quadratic sum $\Delta f_{\text{FONLL}} = \sqrt{\Delta f_{\mu_f, \mu_r}^2 + \Delta f_{m_c}^2 + \Delta f_{\text{PDF}}^2}$. The uncertainties of the total cross section from the extrapolation are then calculated as

$$\Delta \sigma_{\text{tot}}^{D^{*+}}(\text{extr.}) = \sigma_{\text{vis.}}^{D^{*+}} \cdot \Delta f_{\text{FONLL}}. \quad (7.5)$$

7.2.3 Total Cross Sections of D Mesons

The extrapolation factors are summarized in Tab. 7.3. The numbers correspond to the ratios of the total cross sections in the (p_T, y) phase space to the cross sections measured in the visible (p_T, y) phase space.

Meson	\sqrt{s} (TeV)	$f_{\text{FONLL}}(\sigma_{\text{tot}}^D)$	$f_{\text{FONLL}}(\frac{d\sigma}{dy} _{y=0})$
D^0	7	10.7 ^{+6.3} _{-0.5}	1.25 ^{+0.29} _{-0.08}
D^+	7	10.7 ^{+6.2} _{-0.5}	1.25 ^{+0.29} _{-0.08}
D^{*+}	7	10.4 ^{+6.1} _{-0.4}	1.21 ^{+0.28} _{-0.07}
D_s^+	7	N.A.	2.23 ^{+0.71} _{-0.65}
D^0	2.76	9.9 ^{+6.3} _{-0.4}	1.35 ^{+0.48} _{-0.06}
D^+	2.76	19.9 ^{+8.8} _{-1.9}	2.72 ^{+0.80} _{-0.49}
D^{*+}	2.76	18.2 ^{+8.6} _{-1.7}	2.50 ^{+0.72} _{-0.39}

Table 7.3: Summary of the extrapolation factors of D mesons calculated with FONLL in p-p collisions at 7 TeV and 2.76 TeV. Both the extrapolation factors for total cross section σ_{tot}^D and rapidity differential cross section $\frac{d\sigma}{dy}|_{y=0}$ are listed.

In addition to the total cross section, we also give the result of $\frac{d\sigma}{dy}|_{|y|<0.5}$. This is simply done by extrapolating the differential cross section only in the p_T dimension of the phase space, then integrating over the range of $p_T > 0$, in the rapidity region $|y| < 0.5$. The result is $\frac{\Delta\sigma}{\Delta y}|_{|y|<0.5}$, but we may consider it to be the differential cross section $\frac{d\sigma}{dy}|_{y=0}$, since the distribution in this small central rapidity region is rather flat.

We are not able to extrapolate the D_s^+ cross section to the full phase space, because FONLL prediction of D_s^+ differential cross section in the full phase space is unavailable. The absence of D_s^+ prediction from FONLL calculation is due to the lack of D_s^+ fragmentation function in the FONLL model. However, we managed to calculate the D_s^+ differential cross section in the central rapidity. We started from the p_T -differential cross section of charm quark from FONLL calculation. It is then combined with the charm to hadron fraction $f_{c \rightarrow D}$ from ALEPH [71], and the fragmentation functions from [72].

In the 7 TeV p-p collisions, to get the total cross section, the measured cross section is multiplied by the extrapolation factor of ~ 10 . This means we measure only $\sim 10\%$ of the total cross section. The extrapolation factor from visible cross section to full p_T range is ~ 1 at mid-rapidity, which means the measurement covers a large portion in the p_T distribution. In the 2.76 TeV p-p collisions, the scale factor is even higher except for the D^0 measurement. This is because that the measurements have smaller p_T coverage due to the limited statistics. Only the D^0 measurement has a measurement in the $1 < p_T < 2$ GeV/c, where a large portion of the cross section distribute.

The extrapolated total cross sections of the D mesons are listed in

7.2. Total Cross Sections of D Mesons

Meson	\sqrt{s} (TeV)	σ_{tot}^D (mb)	stat.	syst.	lum.	B.R.	extr.
D^0	7	4.42	± 0.35	$^{+0.59}$ $_{-1.50}$	± 0.15	± 0.06	$^{+2.59}$ $_{-0.19}$
D^+	7	2.12	± 0.26	$^{+0.45}$ $_{-0.78}$	± 0.07	± 0.04	$^{+1.23}$ $_{-0.99}$
D^{*+}	7	2.11	± 0.24	$^{+0.31}$ $_{-0.70}$	± 0.07	± 0.03	$^{+1.24}$ $_{-0.08}$
D^0	2.76	3.13	± 0.84	$^{+0.71}$ $_{-1.19}$	± 0.06	± 0.04	$^{+2.02}$ $_{-0.14}$
D^+	2.76	0.93	± 0.19	$^{+0.20}$ $_{-0.22}$	± 0.02	± 0.02	$^{+0.41}$ $_{-0.09}$
D^{*+}	2.76	1.08	± 0.25	$^{+0.24}$ $_{-0.26}$	± 0.02	± 0.02	$^{+0.51}$ $_{-0.10}$

Table 7.4: Summary of the total cross sections of D mesons measured by the ALICE experiment in p-p collisions at 7 TeV and 2.76 TeV.

Meson	\sqrt{s} (TeV)	$\frac{d\sigma}{dy} _{y=0}$ (μ b)	stat.	syst.	lum.	B.R.	extr.
D^0	7	516	± 41	$^{+69}$ $_{-175}$	± 18	± 7	$^{+120}$ $_{-37}$
D^+	7	248	± 30	$^{+52}$ $_{-92}$	± 9	± 5	$^{+57}$ $_{-18}$
D^{*+}	7	247	± 27	$^{+36}$ $_{-81}$	± 9	± 4	$^{+57}$ $_{-16}$
D_s^+	7	118	± 28	$^{+28}$ $_{-34}$	± 4	± 6	$^{+38}$ $_{-35}$
D^0	2.76	428	± 115	$^{+98}$ $_{-163}$	± 8	± 6	$^{+151}$ $_{-23}$
D^+	2.76	127	± 26	$^{+28}$ $_{-31}$	± 2	± 3	$^{+38}$ $_{-23}$
D^{*+}	2.76	148	± 35	$^{+33}$ $_{-36}$	± 3	± 2	$^{+42}$ $_{-23}$

Table 7.5: Summary of the $\frac{d\sigma}{dy}|_{y=0}$ of D mesons measured by the ALICE experiment in p-p collisions at 7 TeV and 2.76 TeV.

Table 7.4. The p_T integrated cross section of the D mesons in the central rapidity $\frac{d\sigma}{dy}|_{y=0}$ is also shown in Table 7.5. The cross sections of D^0 , D^+ and D^{*+} mesons were measured in p-p collisions at both 7 TeV and 2.76 TeV.

The uncertainties of the statistics, the systematics, the luminosity, the branching ratio, and the extrapolation are also scaled by the extrapolation factor. Among these sources of uncertainties, the extrapolation uncertainty and the systematic uncertainty are dominant. The systematic uncertainty originate from the reconstruction and the correction of the raw data, which were discussed in the previous chapter. The extrapolation uncertainty is asymmetric, which is from the uncertainty of FONLL calculation.

The relative extrapolation uncertainty of the total cross section is much smaller than that of the $\frac{d\sigma}{dy}|_{y=0}$ cross section. This is for the reason that, the extrapolation from the range of $|y| < 0.5$ to the full phase space has a large uncertainty. There, the distribution of the differential cross section in the wide range of $|y| > 0.5$ relies only on the calculation. The combination of the measurement in central rapidity and the measurements in forward

rapidity will provide a more precise total cross section. The extrapolation from the combined ALICE and LHCb data gives an improved result [43].

7.3 P_v

The parameter P_v represents the ratio of vector $c\bar{d}$ D mesons to $c\bar{d}$ D mesons in pseudoscalar or vector states. It is calculated by using the ratio between D^{*+} cross section and the sum of D^{*+} cross section and prompt D^+ cross section (those not from D^{*+} decay), as shown in Eq. 7.6. We take only the resonances with the smallest masses, since the other resonances only contribute a very small part of the production cross sections.

$$\begin{aligned}
 P_v &= \frac{\sigma_{tot}^{D^{*+}}}{\sigma_{tot}^{D^{*+}} + \sigma_{tot}^{D^+} - \sigma_{tot}^{D^{*+}} \times (1 - BR_{D^{*+} \rightarrow D^0 + \pi_s^+})} \\
 &= \frac{\sigma_{tot}^{D^{*+}}}{\sigma_{tot}^{D^+} + \sigma_{tot}^{D^{*+}} \times BR_{D^{*+} \rightarrow D^0 + \pi_s^+}}.
 \end{aligned} \tag{7.6}$$

The prompt D^+ cross section is calculated by subtracting the cascade D^+ cross section from the cross section of all the D^+ . The cross section of $c\bar{d}$ D mesons in both pseudoscalar or vector states is equal to the cross section of D^+ and $D^{*+} \rightarrow D^0 \pi_s^+$. By applying the total cross section of D^{*+} and D^+ in 7 TeV and 2.76 TeV, we get

$$\begin{aligned}
 P_v(7\text{TeV}) &= 0.59 \pm 0.06(\text{stat.}) \pm 0.18(\text{syst.}) \pm 0.01(\text{B.R.})_{-0.003}^{+0.005}(\text{extr.}), \\
 P_v(2.76\text{TeV}) &= 0.65 \pm 0.10(\text{stat.}) \pm 0.13(\text{syst.}) \pm 0.01(\text{B.R.})_{-0.004}^{+0.011}(\text{extr.}).
 \end{aligned}$$

The extrapolation uncertainty is calculated in the same way as the extrapolation factor f_{FONLL} . The three uncertainty sources (scale, charm quark mass and parton distribution function) from FONLL calculations are varied separately, while the other two are fixed at the central values. Each maximum deviations from their central value of P_v are summed quadratically.

The extrapolation uncertainty is negligible. This is because the FONLL uncertainty is correlated between the D^{*+} and D^+ total cross section calculations. The luminosity uncertainty also cancels. The statistical and systematic uncertainties are dominant.

These values, in comparison with other experiments at different collision energies and different collision systems, are shown in Fig. 7.7. The average of the experimental measurements reported in Ref. [74] is 0.594 ± 0.010 . The weighted average including LHC measurements is $P_v = 0.60 \pm 0.01$, which is shown by the yellow band.

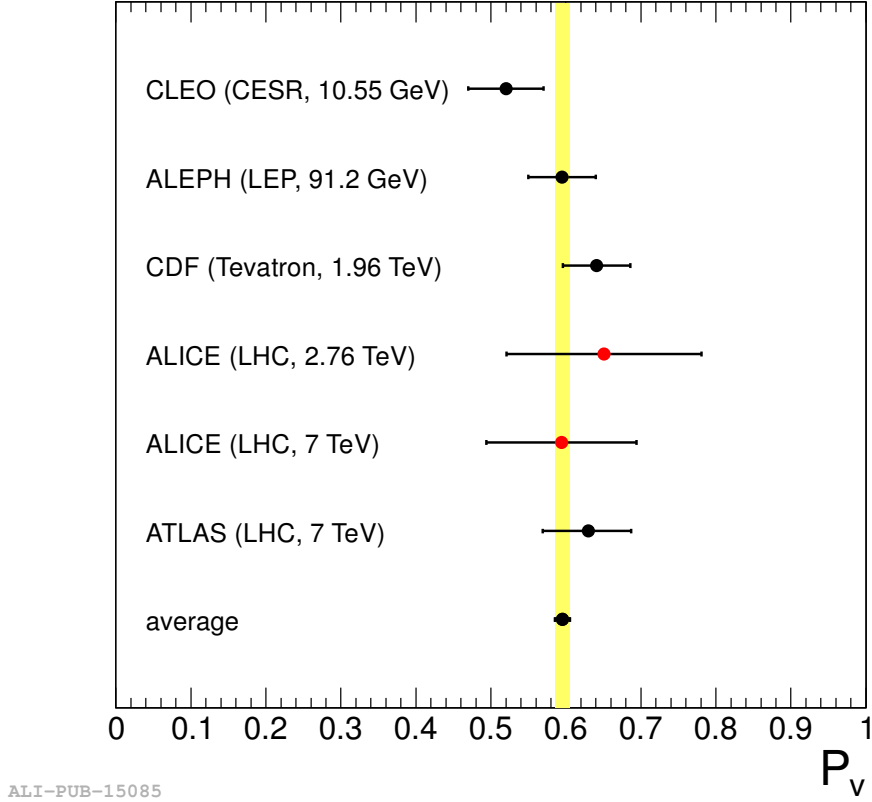


Figure 7.7: The P_v values of $c\bar{d}$ D mesons in various experiment systems [6, 19, 20, 68, 73, 71]. The average of the measurement in Ref. [74] is also shown. The weighted average value is represented by the yellow band.

In the PYTHIA generator, the ratio P_v is defined by the parameter PARJ(13), the default value of which is $P_v = 0.75$. This is calculated from naive spin counting. A vector state D meson has 3 possible spins, while a pseudoscalar state D meson has zero spin. This gives a naive calculation of $P_v^{spincounting} = 3/(3 + 1) = 0.75$. The argument of spin counting originates from heavy quark effective theory (HQET) assuming infinite heavy quark masses. However, the mass difference between D^{*+} and D^+ is $\Delta m/m \approx 7.5\%$, which makes the HQET assumption less applicable. In contrast, the mass difference of the B meson system is $\Delta m/m \approx 0.87\%$, where the HQET assumption is more reliable.

Calculations using the Lund symmetric fragmentation function [75] with exact Clebsch-Gordan coefficient coupling from the virtual quark-antiquark pair to the final hadron state functions predict $P_v = 0.63$. In this model,

the difference between the hadron masses are taken into account in the fragmentation function.

The Statistical Hadronization Model [76] predicts that the ratio of total yields of prompt D^{*+} to D^+ is $3 \cdot (m_{D^{*+}}/m_{D^+})^2 \cdot \exp(-(m_{D^{*+}} - m_{D^+})/T) \approx 1.4$, at a temperature of $T = 164$ MeV. From this we obtain $P_v \approx 0.58 \pm 0.13$ for $T = 164 \pm 10$ MeV. We find that both predictions of Lund fragmentation function and Statistical Hadronization Model agree with our measurement within uncertainties.

7.4 Total Cross Section of Charm Quark Production

Finally, we calculated the total charm cross section $\sigma_{tot}^{c\bar{c}}$ by dividing the total D meson cross section by the fragmentation fraction of each D meson. The fragmentation fraction is the probability that a charm quark forms into a certain D meson species $f_{c \rightarrow D}$. The measured D mesons are sorted into two groups, with one having the D^0 and D^+ mesons and the other having the D^{*+} meson. They can not be summed together, because the second group is a subset of the first one, and exists in an earlier time sequence. The total charm cross section is calculated from the total cross section from the two groups, as shown in the following:

$$\sigma_{tot;D^0D^+}^{c\bar{c}} = \frac{\sigma_{tot}^{D^0} + \sigma_{tot}^{D^+}}{f_{c \rightarrow D^0} + f_{c \rightarrow D^+}}. \quad (7.7)$$

$$\sigma_{tot;D^{*+}}^{c\bar{c}} = \frac{\sigma_{tot}^{D^{*+}}}{f_{c \rightarrow D^{*+}}}. \quad (7.8)$$

The fragmentation fractions are $f_{c \rightarrow D^0} = 0.557 \pm 0.023$, $f_{c \rightarrow D^+} = 0.226 \pm 0.010$, and $f_{c \rightarrow D^{*+}} = 0.238 \pm 0.007$. The weighted average of the two results $\sigma_{tot;D^0D^+}^{c\bar{c}}$ and $\sigma_{tot;D^{*+}}^{c\bar{c}}$ is then calculated, where the weights are defined by the errors. This average is considered the total charm cross section in proton-proton collisions measured with ALICE. The result is listed in Table 7.6, where F.F. stands for the uncertainty from the fragmentation fractions. We find that the extrapolation uncertainty provides one of the largest errors. The statistical and systematic uncertainties are also significant.

Figure 7.8 summarizes the measured charm cross section as a function of center-of-mass energy. A number of charm quark production cross section in various experiments [77, 78, 79] are shown, including recent results from ALICE, ATLAS and LHCb experiments in proton-proton collisions at 7 TeV and 2.76 TeV. Those experiments are carried out in different nucleon-nucleon

7.4. Total Cross Section of Charm Quark Production

\sqrt{s} (TeV)	$\sigma_{tot}^{c\bar{c}}$ (mb)	stat.	syst.	lum.	B.R.	F.F.	extr.
7	8.5	± 0.5	$+1.0$ -2.4	± 0.3	± 0.09	± 0.2	$+5.0$ -0.4
2.76	4.8	± 0.8	$+1.0$ -1.3	± 0.1	± 0.06	± 0.1	$+2.6$ -0.4

Table 7.6: Total charm cross sections in proton-proton collisions at 7 TeV and 2.76 TeV measured by ALICE experiment. The total cross section is extrapolated from the D^0 , D^+ and D^{*+} cross section at mid-rapidity.

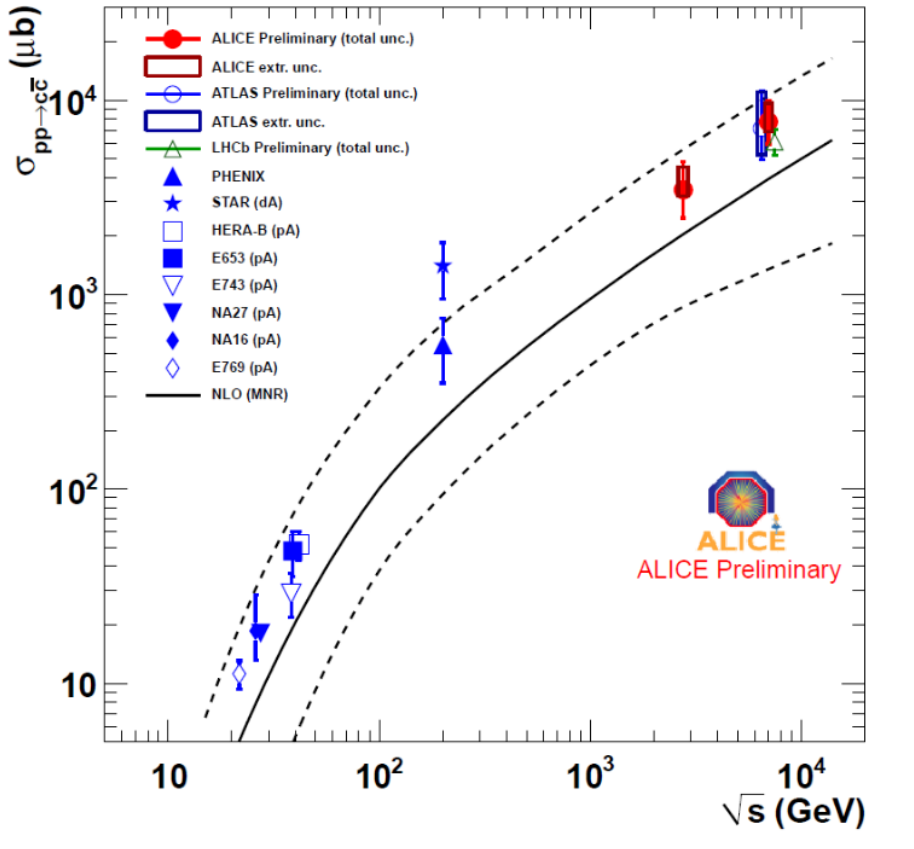


Figure 7.8: Total charm cross section as a function of colliding energy measured by various experiments in nucleon-nucleon collisions. The three data points from ALICE, ATLAS and LHCb are measured at the same energy. The horizontal displacement of the data points is drawn for reading convenience.

collision systems. The cross sections from proton-nucleus (pA) and deuteron-nucleus (d-A) collisions are scaled down by the number of binary nucleon-nucleon collisions, which is calculated with Glauber model. The extrapolated

total cross sections measured by the three experiments at LHC have good agreement with each other.

These measurements are compared to the MNR model, which is an NLO pQCD calculation. The solid curve represents the calculation with the parameters set to their central values. The dashed curves represent the uncertainties of the calculation, which is mainly from the scale variation. In terms of the total cross section calculation, the resummed calculation (e.g. FONLL, GM-VFNS) does not make any improvement over the standard NLO calculation. The resummed terms only make corrections in the high- p_T region, while the low- p_T region contributes mainly to the total cross section.

With the measurements from ALICE, ATLAS and LHCb experiments added, the calculations are tested at a new energy realm. The charm cross sections measured by LHC experiments are still following the trend of increasing cross section with collision energy, as indicated by the calculation. This is because with the higher collision energy, a larger domain of partons distributed in the proton (nucleon) participate in the production of the charm quark. It is also obvious that the experimental results are systematically above the center value of the calculation but still within the uncertainty range.

The cross section shown in Fig. 7.8 is scaled from the measured p_T, y phase space to full phase space by a factor ~ 10 . Therefore, the measurement of the total charm cross section suffers from a large extrapolation uncertainty. However, the NLO pQCD calculation gives an even larger uncertainty, which is mainly from the scale variation. Moreover, the uncertainty band is broadening as the collision energy increases. This is because, in high energy collisions, the uncertainty from the low- x parton distribution becomes significant. The fact that the measurements have more precise results than the calculation leaves a challenge for the calculation to provide more precise predictions. The comparison of the differential cross sections gives more deconvoluted information on the pQCD calculations.

Chapter 8

Summary and Outlook

Within this thesis, for the first time D^{*+} mesons have been identified by their topological decay in the $D^{*+} \rightarrow D^0(K^-\pi^+)\pi^+$ decay channel (and charge conjugates) at mid-rapidity from p-p collisions at $\sqrt{s} = 7$ TeV with the ALICE detector. The topological selection criteria were chosen to optimize the D^{*+} significance. Particle identification with the Time Projection Chamber and the Time of Flight detector was applied. The reconstructed D^{*+} mass is in excellent agreement with values from the literature; the mass resolution is well reproduced by Monte Carlo simulations. The yield is presented in ten transverse momentum bins from 1 to 24 GeV/ c .

The measured differential cross section of prompt D^{*+} meson production is described by state-of-the-art calculations in perturbative QCD, e.g. within the framework of FONLL and GM-FVNS. The central values of the predictions are systematically below (FONLL) or above (GM-FVNS) the data. However, within the rather larger uncertainty in both data and calculations, agreement is found. Taking into account the ALICE measurements of the prompt production of D^0 and D^+ , the total charm production cross section was extracted. Fair agreement with results from the other LHC experiments ATLAS and LHCb was found. The hadronization of charm, once created, to charmed mesons containing a light quark d is independent of the collision system and energy and allows for a description within the statistical model.

In order to address charm production at ultra-low p_T , one might have to use loose topological selection and rely on careful subtraction of the incredible large combinatorial background [80]. Presently, in pp and p-Pb the dependence of the charm production cross section on charged particle multiplicity [81] is poorly understood, and poses a formidable challenge to all models.

Further, the measurement presented in this thesis serves as an essential reference for studies into bulk properties of the Quark-Gluon-Plasma created in Pb-Pb collisions. The nuclear modification factor of D^0 , D^+ and D^{*+} shows a large suppression, indicating strong energy loss of a charm quark propagating in the QGP. This measurement has already been published [21, 82].

Presently, the LHC is in its first long shut down until the end of 2014. In the second round of data taking from 2015-2017, a ten-fold increase in collected data is expected. This will allow a precise measurement of charm production at higher transverse momentum, which will make studies of e.g. charm-jet correlations feasible. During the second long shut down in 2018, ALICE will upgrade the Inner Tracking System [83] with improved pointing resolution and higher read-out rate capabilities. Full reconstruction of B mesons at low momentum will then become possible [84].

Bibliography

- [1] D.J. Gross and F. Wilczek, Phys. Rev. Lett. **30** (1973) 1343.
- [2] H.J. Politzer, Phys. Rev. Lett. **30** (1973) 1346.
- [3] M. Cacciari, M. Greco, P. Nason, J. High Energy Phys. **05** (1998) 007.
- [4] B. A.kniehl, G. Kramer, I. Schienbein, H. Spiesberger, Phys. Rev. D **71** (2005) 014018; Eur. Phys. J. C **41** (2005) 199.
- [5] M. Cacciari, P. Nason, J. High Energy Phys. **0309** (2003) 006.
- [6] The CDF Collaboration, Phys. Rev. Lett. **91** (2003) 241804.
- [7] J. Beringer *et al.*, Phys. Rev. D **86** 010001 (2012).
- [8] A. Dainese, Ph. D. thesis, arXiv: nucl-ex/0311004v2 (2003).
- [9] X. Zhu *et al.*, Phys. Lett. **B647** (2007) 366.
- [10] N. Cabibbo and G. Parisi, Phys. Lett **B59** (1975) 67.
- [11] J.C. Collins and M.J. Perry, Phys. Rev. Lett. **33** (1975) 1353.
- [12] A. Andronic *et al.*, Nucl. Phys. **A789** (2007) 334.
- [13] L Yan, P. Zhuang and N. Xu, Phys. Rev. Lett. **97** (2006) 232301.
- [14] M. Djordjevic and M. Gyulassy, Acta. Phys. Hung. **A24** (2005) 313.
- [15] B. Zhang, L.W. Chen and C-M. Ko, Phys. Rev. **C72** (2005) 024906.
- [16] P. Braun-Munzinger and J. Stachel, Nucl. Phys. **A690** (2001) 119c.
- [17] I. Vitev and M. Gyulassi, Phys. Rev. Lett. **89** (2002) 252301.
- [18] P. Jacobs and X. Wang, Prog. Part. Nucl. Phys **54** (2005) 443.

- [19] B. Abelev *et al.* ALICE Collaboration, J. High Energy Phys. **01** (2012) 128.
- [20] B. Abelev *et al.* ALICE Collaboration, J. High Energy Phys. **07** (2012) 191.
- [21] B. Abelev *et al.* ALICE Collaboration, J. High Energy Phys. **09** (2012) 112.
- [22] M. Gell-Mann, Phys. Lett. **8** (1964) 214.
- [23] G. Zweig, CERN Report No.8182/TH.401; No.8419/TH.412.
- [24] B. J. Bjorken, S. L. Glashow, Phys. Lett. **11** (1964) 255.
- [25] J. E. Augustin *et al.*, Phys. Rev. Lett. **33** (1974) 1406.
- [26] J. J. Aubert *et al.*, Phys. Rev. Lett. **33** (1974) 1404.
- [27] A. D. Martin *et al.*, arXiv: hep-ph/0901.0002 (2009).
- [28] J. Stirling, <http://http://www.hep.phy.cam.ac.uk/~jjs/>, High Energy Physics Group, Cavendish Laboratory.
- [29] H-U. Bengtsson and T. Sjöstrand, Comput. Phys. Commun. **46** (1987) 43;
T. Sjöstrand, Comput. Phys. Commun. **82** (1994) 74;
T. Sjöstrand, S. Mrenna, P. Skands, JHEP **05** (2006) 026.
- [30] ALICE Collaboration, ALICE: Physics Performance Report, Volume II, J. Phys. G: Nucl. Part. Phys. **32** (2006) 1295-2040.
- [31] D. J. Gross, F. Wilczek, Phys. Rev. Lett. **30** (1973) 1343.
- [32] J. C. Collins, D. E. Soper, G. Sterman, Nucl. Phys. B **263** (1986) 37.
- [33] S. Bethke, Nucl. Phys. Proc. Suppl. **234** (2013) 229; arXiv:hep-ex/1210.0325v1.
- [34] G. Altarelli, Phys. Rep. **81** (1982) 1.
- [35] C. Peterson *et al.*, Phys. Rev. D **27** (1983) 105.
- [36] V. G. Kartvelishvili, A. K. Likhoded, V. A. Petrov, Phys. Lett. **B78** (1978) 615.
- [37] M. G. Bowler, Zeit. Phys. **C11** (1981) 169.

- [38] P. B. B. Collins, T. P. Spiller, J. Phys. G **11** (1985) 1289.
- [39] S. Kretzer, H. L. Lai, F. I. Olness, W. K. Tung, Phys. Rev. **D69** (2004) 114005.
- [40] M. Buza, Y. Matiounine, J. Smith, R. Migneron, W. L. van Neerven, Nucl. Phys. **B472** (1996) 611.
- [41] M. L. Mangano, P. Nason, G. Ridolfi, Nucl. Phys. B **373** (1992) 295.
- [42] J. Baines *et al.*, arXiv: hep-ph/0601142.
- [43] H. Cakir, Bachelor thesis (2013), Univ. of Heidelberg.
- [44] L. Evans, New J. Phys. **9** (2007) 335.
- [45] LHC webpage, <http://lhc.web.cern.ch/lhc/>.
- [46] P. Braun-Munzinger and J. Stachel, Nature **448** (2007) 302.
- [47] ALICE Collaboration, ALICE: Physics Performance Report, Volume I, J. Phys. G: Nucl. Part. Phys. **30** (2004) 1517-1763.
- [48] P.G. Kuijer Nucl. Phys. A830(2009)81C-88C arXiv:0907.5060[hep-ex].
- [49] K. Aamodt *et al.*(ALICE Collaboration) Phys. Rev. Lett. 105, 252301(2010).
- [50] J. Alme *et al.* (ALICE Collaboration), arXiv: 1001.1950.
- [51] W. Blum, W. Riegler and L. Rolandi, Particle Detection with Drift Chambers, 2nd ed. (Springer-Verlag, 2008).
- [52] M. Gagliardi *et al.* (ALICE Collaboration), arXiv: 1109.5369 [hep-ex].
- [53] S. Van der Meer, ISR-PO/68-31, KEK68-64.
- [54] ROOT User's Guide, <http://root.cern.ch/root/doc/RootDoc.html>.
- [55] P. Hristov, AliRoot Primer, <http://aliweb.cern.ch/Offline/AliRoot/Manual.html>.
- [56] X-N. Wang and M. Gyulassy Phys. Rev. **D44** (1991) 3501;
M. Gyulassy and X-N. Wang Comput. Phys. Commun. **83** (1991) 307-31.
- [57] R. Brun, F. Bruyant, M. Maire, A. C. McPherson and P. Zancarini, GEANT3 User Guide CERN Data Handling Division DD/EE/84-1 (1985).

- [58] S. Agostinelli *et al.*, Geant4 Simulation Toolkit CERN-IT-20020003, KEK Preprint 2002-85, SLACPUB-9350; Nucl. Instr. Meth. **A506** (2003) 250.
- [59] A. Fassò *et al.*, Proc. Computing in High Energy and Nuclear Physics (La Jolla, CA) (2003).
- [60] P. Billoir, Nucl. Instr. Meth. **A225** (1984) 352;
P. Billoir *et al.*, Nucl. Instr. Meth. **A241** (1984) 115;
R. Fruhwirth, Nucl. Instr. Meth. **A262** (1987) 444;
P. Billoir, Comput. Phys. Commun. **57** (1989) 390.
- [61] P. Kindziuk *et al.*, ALICE-INT-1999-34.
- [62] C. Ivan, Doctoral thesis (2010), Univ. of Utrecht.
- [63] R. Grajcarek, Doctoral thesis (2013), Univ. of Heidelberg.
- [64] T. Aaltonen *et al.* CDF Collaboration, Phys. Rev. D **77** 072003 (2008).
- [65] M. Cacciari *et al.*, JHEP **0407** (2004) 033.
- [66] R. Aaij *et al.* (LHCb Collaboration), Phys. Lett. **B694** (2010) 209.
- [67] V. Khachatryan *et al.* (CMS Collaboration), Eur. Phys. J. **C71** (2011) 1575.
- [68] The ATLAS Collaboration, ATL-PHYS-PUB-2011-012.
- [69] R. Maciula, M. Luszczak, A. Szczurek, arXiv:1208.6126 [hep-ph].
- [70] B. Abelev *et al.* ALICE Collaboration, Phys. Lett. B **718** (2012) 279.
- [71] R. Barate, *et al.* ALEPH Collaboration, Eur. Phys. J. C **16** (2000) 597.
- [72] E. Braaten, K. Cheung, S. Fleming, T. C. Yuan, Phys. Rev. D **51** (1995) 4819.
- [73] D. Bortoletto *et al.* [CLEO Coll.], Phys. Rev. D **37** (1988) 1719, Phys. Rev. D **39** (1989) 1471.
- [74] A. David, Phys. Lett. **B644** (2007) 224.
- [75] C. D. Buchanan, S. B. Chun, Phys. Rev. Lett. **59** (1987) 1997.
- [76] A. Andronic *et al.*, Phys. Lett. **B652** (2007) 259.

- [77] C. Lourenço, H. K. Wöhri, Phys. Rept. **433** (2006) 127.
- [78] J. Adams *et al.* STAR Collaboration, Phys. Rev. Lett. **94** (2005) 62301.
- [79] A. Adare *et al.* PHENIX Collaboration, Phys. Rev. **C 84** (2011) 044905.
- [80] C. Möhler, Master thesis (2013), Univ. of Heidelberg.
- [81] J. Wilkinson, Doctoral thesis (in preparation), Univ. of Heidelberg.
- [82] B. Abelev *et al.* ALICE Collaboration, Phys. Rev. Lett. **111** (2013) 102301.
- [83] B. Abelev *et al.* ALICE Collaboration, CERN-LHCC-2012-013.
- [84] J. Stiller, Doctoral thesis (in preparation), Univ. of Heidelberg.

Bibliography

Acknowledgement

I owe my greatest gratitude to my supervisor Dr. Kai Schweda, who not only provides me this great opportunity to work on this challenging but interesting topic, but also gives me amounts of support on both my study and living. The many discussions with him keep me inspired and motivated. Without his help, I will not finish my study.

I would also like to give my gratitude to Prof. Dr. Johanna Stachel, who provides the opportunity to work in the ALICE TRD group. Her advices on the rehearsals of my many presentations helped me acquired much knowledge from her experience and improve the quality of the presentations.

I would like to thank Prof. Dr. Norbert Herrmann, who agreed to be the referee of my thesis.

I am also grateful to the effort of Dr. Yvonne Pachmayer, Dr. Minjung Kweon, Micheal Winn, Jochen Klein, Jeremy Wilkinson, Robert Grajcarek and Martin Völkl, who helped be by proof reading the thesis.

Last but not least, I would like to thank Weiwei and my parents, who have been always supporting my study.

This work has been supported by the Helmholtz Association under contract number VHNG-147 and HA216/EMMI. and and the Federal Ministry of Education and Research under promotional reference 06HD197D.

